Volume 53 Number 14 21 July 2024 Pages 7301-7634

Chem Soc Rev

Chemical Society Reviews

rsc.li/chem-soc-rev



ISSN 0306-0012



REVIEW ARTICLE

Chem Soc Rev



REVIEW ARTICLE

View Article Online



Cite this: Chem. Soc. Rev., 2024, **53**. 7392

Advancing electrocatalytic reactions through mapping key intermediates to active sites via descriptors

Xiaowen Sun, Rafael B. Araujo, Egon Campos dos Santos, Yuanhua Sang, O

Descriptors play a crucial role in electrocatalysis as they can provide valuable insights into the electrochemical performance of energy conversion and storage processes. They allow for the understanding of different catalytic activities and enable the prediction of better catalysts without relying on the time-consuming trial-and-error approaches. Hence, this comprehensive review focuses on highlighting the significant advancements in commonly used descriptors for critical electrocatalytic reactions. First, the fundamental reaction processes and key intermediates involved in several electrocatalytic reactions are summarized. Subsequently, three types of descriptors are classified and introduced based on different reactions and catalysts. These include d-band center descriptors, readily accessible intrinsic property descriptors, and spin-related descriptors, all of which contribute to a profound understanding of catalytic behavior. Furthermore, multi-type descriptors that collectively determine the catalytic performance are also summarized. Finally, we discuss the future of descriptors, envisioning their potential to integrate multiple factors, broaden application scopes, and synergize with artificial intelligence for more efficient catalyst design and discovery.

Received 3rd March 2024 DOI: 10.1039/d3cs01130e

rsc.li/chem-soc-rev

- ^a State Key Laboratory of Crystal Materials, Shandong University, Jinan 250100, China. E-mail: hongliu@sdu.edu.cn, xiaowen.yu@sdu.edu.cn
- ^b Department of Materials Science and Engineering, The Ångstrom Laboratory, Uppsala University, SE-751 03 Uppsala, Sweden
- ^c Departamento de Física dos Materials e Mecânica, Instituto de Física, Universidade de SãoPaulo, 05508-090, São Paulo, Brazil
- ^d Jinan Institute of Quantum Technology, Jinan Branch, Hefei National Laboratory, Jinan, 250101, China

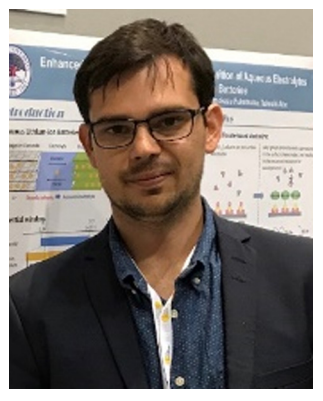
1. Introduction

Development of green and sustainable energy systems to produce clean fuels and valuable chemicals has been a crucial strategy for addressing environment and energy challenges. 1-3 Hydrogen (H₂) is one of the cleanest fuels because it only produces water (H₂O) as a byproduct when burned. In recent years,



Xiaowen Sun

Xiaowen Sun obtained her BS degree from the School of Physics and Technology, the University of Jinan, China, in 2021. Currently, she studies as a PhD student in Prof. Hong Liu's group at the State Key Laboratory of Crystal Materials, Shandong University, China. Her current research mainly focuses on theoretical calculations for electrocatalysis.



Rafael B. Araujo

Dr Rafael B. Araujo received his PhD in computational physics from Uppsala University, Sweden, in 2017. He worked as a postdoctoral researcher at Chalmers University of Technology, Stockholm University, and Uppsala University, Sweden. He has continued as a researcher at the Department of Materials Science and Engineering, Uppsala University, since September 2022. His research interests include applying a broad range of computational tools to explore

scientific challenges in catalysis, batteries, and materials for energy storage.

significant efforts have been made to efficiently and sustainably produce H₂ through electrochemical hydrogen evolution reaction (HER).4-7 Oxygen evolution reaction (OER) and oxygen reduction reaction (ORR) are crucial processes in energy conversion and storage technologies.^{8–13} They serve as core reactions in renewable energy devices such as fuel cells and water splitting systems. However, these reactions often suffer from sluggish kinetics and high overpotentials (η) , which significantly impacts their overall energy efficiencies. To address these challenges, it is essential to develop electrocatalysts with high catalytic activity and chemical stability to enhance the performance of OER and ORR. 14-16 As is known, the strong triple bond (N≡N) between nitrogen atoms makes the nitrogen (N_2) gas unreactive under normal conditions. Breaking of this N=N triple bond requires overcoming a high potential barrier. Industrially, N2 is a critical raw material in the production of ammonia (NH₃). The most well-known method for this process is the Habor-Bosch process, which utilizes Fe-based catalysts at high temperatures and pressures. However, this traditional process is energy-intensive and contributes to carbon dioxide (CO₂) emissions. ¹⁷⁻¹⁹ In contrast, electrochemical reduction of N2 to NH3 (NRR) offers a promising alternative that can significantly reduce the energy consumption and carbon footprint associated with NH3 production. 20-23 In addition, to address the concerning issue of melting glaciers and collapsing permafrost caused by global warming, extensive research has been conducted on the electrochemical CO2 reduction reaction (CO₂RR). This process converts CO₂ into high-value fuels or various multi-carbon products.²⁴⁻²⁷ All in all, electrocatalytic reactions are essential for addressing the energy crisis and environmental issues. To enable efficient electrochemical reactions, it is of great importance to develop highly active catalysts that can effectively lower energy barriers and increase reaction rates while maintaining high selectivity towards desired products.

Understanding the interactions between catalysts and reaction intermediates is pivotal for improving the catalytic activity of certain catalysts. These interactions occur at specific sites on



Egon Campos dos Santos

Dr Egon Campos Dos Santos received his PhDdegree in chemistry from Universidade Federal de Minas Gerais, Brazil, in 2019. He subsequently worked in various esteemed international theoretical computational groups, including a two-year postdoc period in surface chemical physics and corrosion at Stockholm University, Sweden (2019-2021); one-year postdoc in computational chemistry at Stanford University, USA (2021-2022); and

one-year Assistant Professor in Tohoku University, Japan (2022-2023). Since 2024 he has been working as a postdoc at the Physics Department at University of São Paulo, Brazil. His research interest focuses on the theoretical electrocatalysis method.



Yuanhua Sang

Prof. Yuanhua Sang obtained his BS degree from Shandong University, China, in 2007 and received his PhDdegree from Shandong University in July 2012. Now, he works as a professor at the State Key Laboratory of Crystal Materials, Shandong University. His research interests include nanomaterials for solar light conversion, especially for photocatalysis and photothermal application; functional crystal materials for nonlinear optics; and biomaterials for tissue engineering.



Hong Liu

Prof. Hong Liu received his PhD degree from Shandong University, China, in 2001. Since 2002 he has been working as a professor at the State Key Laboratory of Crystal Materials, Shandong University. His research interests include nanomaterials photocatalysis, electrolysis, and biosensors; tissue engineering and stem cells; and functional crystal materials.



Xiaowen Yu

Prof. Xiaowen Yu received her PhD degree in chemistry from Tsinghua University, China, in 2018. Then she worked as a postdoc at the Department of Materials and Environmental Chemistry, Stockholm University, Sweden, from 2018 to 2021. Since 2022 she has been working as a professor at the State Key Laboratory of Crystal Materials, Shandong University, China. Her research interests include rational design of electrocatalysts and (photo)electrochemical synthesis of value-added molecules.

the catalysts' surface, known as active sites, whose concept was first introduced by Taylor in 1925,28 laying the foundation for subsequent research on the electronic structure of catalysts and the binding between catalysts and reaction intermediates. The Sabatier principle, as proposed by Nørskov,²⁹ states that for optimal catalytic performance, the adsorption of reaction intermediates on the catalyst surface should neither be too strong nor too weak. Instead, a moderate level of adsorption is preferred. Accordingly, a volcano plot visualizes the relationship between catalytic activity and adsorption energy of reaction intermediates for different catalysts. 30-32 Catalysts located near the peak of the volcano diagram have an optimal balance of adsorption energy and thereby the highest catalytic activity. On the other hand, catalysts with weak adsorption energy have lower catalytic activity due to insufficient interaction with the reaction intermediates. Similarly, catalysts with excessively strong adsorption energy may hinder the release of the final products, leading to reduced catalytic efficiency. This suggests that modifying the adsorption strength of key intermediates can optimize the catalytic activity of materials. Various approaches, such as doping heteroatoms, introducing defects, forming alloys, employing strain/stress, and designing heterojunctions on catalysts, have been employed to alter the electronic structure of active sites. By doing so, the adsorption strength of catalyst surfaces and intermediates can be modulated, leading to significant changes in catalytic performance. 33-37 Especially, if the readily accessible intrinsic properties or electronic structure features of a catalyst material can be used as descriptors to correlate with the adsorption energy of key intermediates in reactions or its catalytic activity in a linear or volcano plot, it allows for a physical or chemical mechanistic explanation of the origin of the catalysts' activity. This understanding can then be utilized to efficiently screen and design other catalysts with desired properties.38-40

The design of catalysts based on descriptors offers a more efficient and targeted approach to catalyst development. By utilizing descriptors, researchers can significantly reduce the need for extensive theoretical calculations and experimental tests, and thereby save valuable time, resources, and efforts in the search for highly active catalysts.^{27,41-46} One of the simplest descriptors used in catalysts is based on the adsorption energy of key intermediates. For instance, the adsorption Gibbs free energy of H atoms (ΔG_{*H}) is commonly employed to directly describe the catalytic activity of the considered catalysts for HER.47-49 Additionally, the adsorption energy of O atoms (ΔE_{*O}) usually exhibits a linear relationship with the adsorption energies of OH (ΔE_{*OH}) and OOH (ΔE_{*OOH}), which also provides valuable information for evaluating catalytic activities in OER and ORR. 50-52 However, for multi-electron complex processes such as NRR and CO₂RR, multiple reaction intermediates are involved, making it challenging to evaluate catalytic activity using a single descriptor based on a particular intermediate. In 1987, Nørskov proposed a fitting of the adsorption energy of nitrogen atoms (ΔE_{*N}) to the limiting potential $(U_{\rm L})$ of NRR on metal surfaces, successfully replacing the adsorption energies of various Nrelated intermediates (e.g., N_xH_v) in NRR by ΔE_{*N} , resulting in a

volcano diagram relationship between ΔE_{*N} and U_L , which can effectively illustrate how ΔE_{*N} can serve as a descriptor for evaluating the catalytic activity of transition metals (TMs) for NRR.53 In addition, some descriptors have been utilized to predict the trend of electrocatalytic activity, including the widely used metal d-band center, O-2p band center for oxides, e_o filling, electron transfer, number of active sites, electronegativity, bond lengths, etc.54-60 In the past decade, there has been increasing interest in investigating the catalytic activity of spin-regulated systems. It has been observed that changing the spin state of the active site can influence the binding interactions of the active centers with intermediates, thereby modulating the catalytic activity.61,62

Although there have been several reviews on descriptors in recent years, many of them focused on specific types of descriptors or descriptors for particular reactions, 63-65 and there are relatively fewer comprehensive summaries available that encompass descriptors related to readily accessible intrinsic properties, spin-related characteristics, the application of comprehensive d-band centers, and the multi-type descriptors. In this review, we aim to provide a systematic and comprehensive summary of the relevance of physical and chemical features mapping key reaction intermediates and their applications as descriptors to quantify the catalytic activity of reactions (see overview in Fig. 1). First, we describe the critical electrochemical reaction processes such as HER, OER, ORR, NRR, and CO2RR under different conditions and identify the available key reaction intermediates that can be correlated to quantify the catalytic activity. Then, by combining the results of density functional theory (DFT) calculations and experimental data, we summarize the descriptors for the above-mentioned electrochemical reactions. The descriptors are categorized into d-band center descriptors, readily accessible intrinsic properties of the catalysts that can be obtained directly from databases, spinrelated property descriptors, and multi-type descriptors. Finally, by summarizing the current state of descriptor-related research, we provide a comprehensive perspective on this field and highlight potential directions for future descriptor studies.

2. Fundamental reaction processes and the involved key intermediates

The advancement of descriptors based on certain properties of catalysts has facilitated the prediction of catalytic performance in various electrocatalytic reactions without the need to carry out the entire reaction process. Different reaction pathways for a given reactant can lead to the formation of different intermediates, generate products in different orders, or even produce different products. This variability in the reaction pathway can have a significant impact on the overall reaction activity. 66-68 For instance, during the protonation of different atoms in nitric oxide (NO), the first product could be either H₂O or NH₃, depending on the specific reaction pathway.⁶⁹ Additionally, critical intermediates in reactions can serve as important indicators for forecasting the electrocatalytic activity of certain

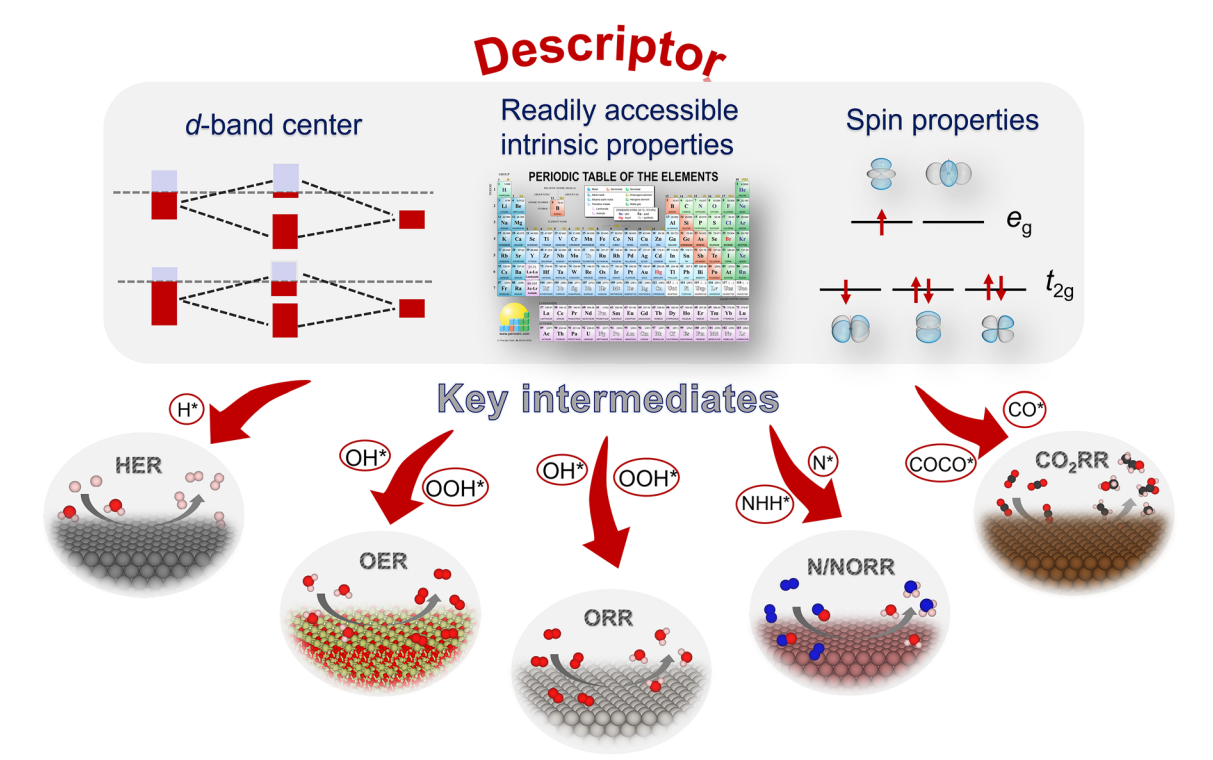


Fig. 1 Overview of the descriptors utilized in diverse electrocatalytic reactions.

catalysts with high efficiency. Recent works have highlighted the importance of understanding the interaction between key intermediates and active sites. 70,71 Correctly understanding the elementary reaction steps involving multiple electron transfer and further exploiting key intermediates in the reaction processes are essential for achieving transformative advances in the development of descriptors for efficiently screening electrocatalysts.

2.1. HER process and key intermediates

As one of the promising energy storage carriers, H₂ has always attracted considerable attention. Production of H2 through the conventional method, such as methane (CH₄) steam reforming, can result in significant CO2 emission, contributing to greenhouse gas effects and climate change. As an alternative, electrochemical HER, which is the cathodic half reaction of water electrolysis ($H_2O \rightarrow H_2 + 1/2O_2$), offers a more environmentally friendly route to produce H₂ without CO₂ emission.⁷² The HER pathway can vary under different pH conditions. In an acidic electrolyte, two reaction mechanisms are widely accepted: Volmer-Heyrovsky mechanism and Volmer-Tafel mechanism (Fig. 2a).⁷³⁻⁷⁶ In both mechanisms, the initial Volmer step involves adsorption of protons from the solution to form adsorbed hydrogen species (*H) (H + * \rightarrow *H).⁷⁷ In the above reaction, the asterisk * represents the adsorption site on the catalyst surface. The distinction between these two mechanisms lies in the subsequent steps. For the Heyrovsky step, the adsorbed intermediate *H reacts with one solvated proton in solution to form H_2 ($H^+ + e^- + *H \rightarrow H_2$). For the Tafel step, the adsorbed *H intermediates interact with each other to form H2

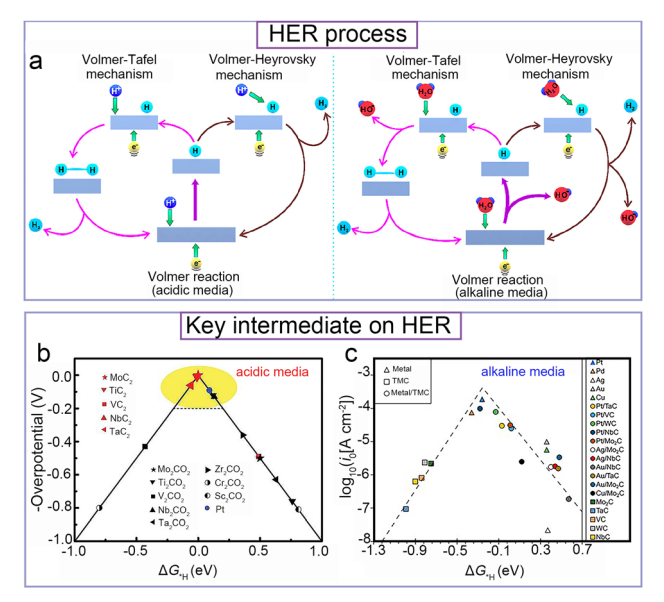


Fig. 2 (a) Mechanism diagram of HER on the surface of an electrode. Reproduced with permission. Copyright 2020, American Chemical Society.73 (b) HER volcano curve of metal carbides (red) compared to the previously reported O-terminated MXenes (black) and Pt (blue) in acidic media. Reproduced with permission. Copyright 2020, Wiley-VCH.76 (c) HER volcano curve of transition metal carbides in alkaline media. Reproduced with permission. Copyright 2019, American Chemical Society. 78

(*H + *H \rightarrow H₂). In an alkaline electrolyte, due to the low H⁺ (proton) concentration, the production of H2 can be considered to occur through a two-step process known as the Volmer-Heyrovsky mechanism. In the first step, the adsorbed water

molecule accepts an electron to form an adsorbed *H and a hydroxyl ion $(H_2O + e^- + * \rightarrow *H + OH^-)$. In the second step, another water molecule reacts with the adsorbed *H and an electron to produce molecular H2 and release a hydroxyl ion $(H_2O + *H + e^- \rightarrow H_2 + OH^-).^{74,78}$

The strength of the interaction between the H atom and the catalyst surface, as determined by ΔG_{*H} , plays a crucial role in determining the catalytic activity of catalysts for HER. According to the Sabatier principle,29 an optimal catalyst for HER should exhibit a moderate ΔG_{*H} . If the interaction between *H and the catalyst surface is too strong, the active sites will be poisoned, thus hindering the desorption of molecular H2 from the catalyst surface. On the other hand, if the *H adsorption is too weak, the reaction will require higher η , meaning that an additional energy input is needed to drive the reaction forward, which will result in an increase in energy consumption and a decrease in overall efficiency. Therefore, an ideal HER catalyst should strike a balance between *H uptake and release, and thereby a moderate adsorption strength for *H. Experimental studies have identified Pt and Pt-based metals as the most active catalysts for the HER. Theoretical calculations have revealed that these catalysts exhibit moderate H adsorption, indicated by a moderate ΔG_{*H} value. This suggests that the ΔG_{*H} parameter can effectively characterize the catalytic activity of catalysts. For example, in an acidic electrolyte, ΔG_{*H} is considered as the simplest and most intuitive descriptor for HER; its absolute value $|\Delta G_{*H}|$ can serve as an indicator of the catalytic activity of the catalyst. Generally, a smaller value of $|\Delta G_{*H}|$ indicates better catalytic performance of the catalyst, as shown in Fig. 2b.76 In an alkaline electrolyte, although the binding energy of OH and the kinetics barrier for water dissociation have significant impacts on the catalytic activity of the catalysts for HER, ΔG_{*H} still plays important roles, which can also exhibit a volcano-type diagram as a function of the logarithm of theoretical exchange current density i_0 (lg(i_0)) (Fig. 2c).⁷⁸ Therefore, in both acidic and alkaline electrolytes, wherein the adsorbed *H is a critical intermediate for HER, ΔG_{*H} associated with *H is a key factor in determining the catalytic activity of catalysts for HER. Furthermore, it is important to note that the kinetics barriers also play a significant role in HER. For instance, many metal catalysts exhibit H binding strength comparable to that of Pt, but display significantly lower activity in catalyzing HER. This discrepancy may arise from the distinction between the kinetically active H species and the inactive surface H species with binding energies as descriptors. For Pt and Au, the H atoms with $G \sim 0$ (hollow site) are inert in the kinetic correlation region, whereas the top H atoms are active and show weaker H adsorption. For the HER on Au, the H atoms should transit through a less strongly bound top site before diffusing into the stable hollow site. This diffusion encounters a high potential barrier, which contributes to the observed low HER activity on Au. In contrast, for the HER on Pt, H atoms located at the top site with particularly low barriers facilitate higher reaction rates. Therefore, it is essential to recognize that the HER activity cannot be accurately assessed solely based on $G \sim 0.79$ Thorough analysis of kinetically relevant H and inactive H species is crucial for a comprehensive understanding of HER catalysts.

2.2. OER and ORR pathway and key intermediates

The OER is a key half reaction in water electrolysis. In acidic media, the OER can be represented by the equation $2H_2O \rightarrow O_2 +$ $4H^+ + 4e^-$. In alkaline media, the equation changes to $4OH^- \rightarrow$ $O_2 + 2H_2O + 4e^-$. Compared with the HER, which involves a twoelectron transfer process occurring at the cathode, the anodic OER is more sluggish in kinetics due to its four-electron transfer process. 76,80 The elementary steps of OER are distinctly different under different pH conditions (Fig. 3a). In an acidic electrolyte, the elementary steps of the OER can be described as follows:76,81-83 (i) A water molecule interacts with the catalyst surface and dissociates into *OH and *H (* + H2O → *OH + $H^+ + e^-$). (ii) The *OH undergoes a dehydrogenation process to produce *O (*OH \rightarrow *O + H⁺ + e⁻). (iii) The *O combines with another water molecule to generate *OOH (*O + H₂O → *OOH $+ H^{+} + e^{-}$). (iv) The *OOH undergoes a deprotonation reaction to form the target O_2 (*OOH \rightarrow * + O_2 + H⁺ + e⁻). In an alkaline electrolyte, O2 is produced according to the following steps:84,85 (i) * + OH $^- \rightarrow$ *OH + e $^-$; (ii) *OH + OH $^- \rightarrow$ *O + H₂O + e $^-$; (iii) *O + OH $^- \rightarrow$ *OOH + e $^-$; and (iv) *OOH + OH $^- \rightarrow$ O₂ + * + $H_2O + e^-$.

In the assessment of the OER catalytic activity, the ΔG of each reaction step serves as a critical parameter. There are two commonly utilized indexes to evaluate the OER activity of the catalyst: (i) $U_{\rm L}$ is defined as $U_{\rm L} = -\Delta G_{\rm max}/e$, where $\Delta G_{\rm max}$ represents the maximum increase in the Gibbs free energy of the reaction. (ii) η^{OER} is defined as the difference between U_{L}

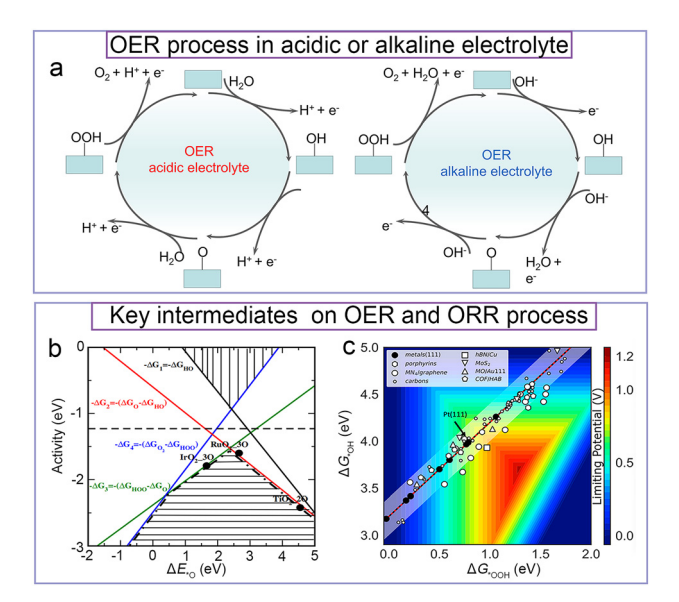


Fig. 3 (a) The mechanism representation of OER on the surface of a catalyst in acidic and alkaline electrolytes. (b) The volcano curve between ΔE_{*O} and OER activity. Reproduced with permission. Copyright 2007, Elsevier. 86 (c) The 3D volcano plot showing the "standard" scaling relationship ($\Delta G_{\star OOH} = \Delta G_{\star OH} + 3.20$) for $\Delta G_{\star OOH}$ and $\Delta G_{\star OH}$ in ORR for a wide variety of two-dimensional materials. Reproduced with permission. Copyright 2018, American Chemical Society.87

Review Article

required for adsorption of *OOH is approximately 3.20 eV and equilibrium potential (U_0) ; this difference represents the higher than that of *OH (Fig. 3c).87 From the analysis mentioned above, it is apparent that the ORR activity of the catalyst is limited by this scaling relationship. In theory, an ideal ORR catalyst would operate at the equilibrium potential of 1.23 V, where all the reaction free energies would be zero. 2.3. NRR and NO reduction reaction (NORR) pathways and

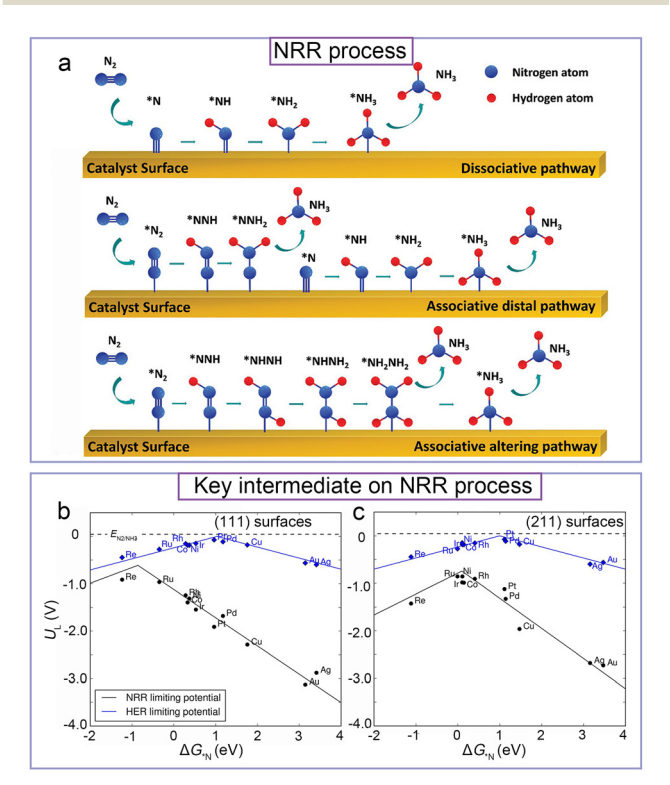
additional potential required to drive the OER beyond the thermodynamically balanced potential, i.e., $\eta^{OER} = U_L - U_0$. For the reaction $2H_2O \rightarrow H_2 + O_2$, U_0 is known as 1.23 V.⁸² Therefore, $\eta^{\rm OER}$ can also be expressed as $\eta^{\rm OER} = U_{\rm L} - 1.23 \text{ V.}^{85,88} \text{ A lower}$ n^{OER} generally indicates better catalytic activity of the catalysts being considered. Currently, Ru and Ir oxides are considered as the best metal-based OER catalysts. For instance, through DFT calculations, Rossmeisl et al. identified that RuO2 and IrO2 are located at the apex of the ΔG_{*O} volcano diagram for the OER, suggesting that these catalysts are the most effective catalysts for this reaction, and highlighting the significance of *O as a crucial reaction intermediate in this process (Fig. 3b).86 Additionally, the adsorbed *OH and *OOH species are also considered as key intermediates in OER. For example, in 2011, Nørskov et al. studied a large number of oxide surfaces for OER and found interesting results regarding the relationships among ΔG_{*OH} , ΔG_{*O} , and ΔG_{*OOH} . They found a linear relationship between ΔG_{*OOH} and ΔG_{*OH} with a slope of approximately 1; this suggests that both *OOH and *OH species are bound to the catalyst site through a single bond. On the other hand, the slope for the linear relationship between ΔG_{*O} and ΔG_{*OH} is approximately 2, indicating that *O is bound to the catalyst site through a double bond. 89-91 Additionally, they established a volcano curve to describe the OER catalytic activity of various oxide surfaces by correlating $-\eta^{\text{OER}}$ as a function of $\Delta G_{*O} - \Delta G_{*OH}$.⁸⁹

The electrochemical ORR occurring at the cathode is a determining reaction that limits the development of Zn-air batteries and proton exchange membrane fuel cells. 92 It should be noted that ORR can be considered as the reverse reaction of OER, and they share the same intermediates (e.g., *O, *OH, *OOH). The ORR can proceed through two main pathways, depending on the number of electrons transferred during the overall reaction. One pathway involves the reduction of O2 to H₂O by transferring four electrons. Another pathway involves the reduction of O2 to hydrogen peroxide (H2O2) by transferring two electrons. 93-97 The overall reaction for the four-electron transfer during the ORR is $O_2 + 4H^+ + 4e^- \rightarrow H_2O$ in acidic media or O_2 + $2H_2O$ + $4e^- \rightarrow 4OH^-$ in alkaline media. In the ORR process, the initial step involves the activation of O_2 . Generally, it is believed that the adsorption of molecular O₂ onto a surface is a chemical process and that electron transfer is unlikely to limit the rate of this process. However, through the use of ab initio molecular dynamics (AIMD) coupled with a solvation model, Dudzinski et al. revealed that O2 adsorption on Au(111) during the ORR is significantly influenced by the applied (absolute) potential due to local electric field effects. This observed dependency implies that O2 adsorption should be viewed as an electrochemical step rather than purely a chemical one, underscoring the importance of O2 adsorption in the overall process.⁹⁸ Additionally, the strength of *OH adsorption on the catalyst surface, represented by ΔG_{*OH} , is recognized to play a crucial role in determining the ORR kinetics. There is a commonly accepted standard scaling relationship between ΔG_{*OOH} and ΔG_{*OH} : $\Delta G_{*OOH} = \Delta G_{*OH} +$ 3.20 eV. This scaling relationship implies that the energy

their key reaction intermediates

NH₃ is a crucial raw material in the synthesis of amino acids and the production of fertilizers. The current industrial method for the production of NH₃ mainly relies on the Haber-Bosch process, which requires high temperature (400-500 °C) and high pressure (10-30 MPa) conditions. However, these harsh reaction conditions and massive CO2 emission associated with the process greatly limit the development of NH₃ production. As an alternative to the Haber-Bosch process, electrochemical NRR (N₂ (g) + 6H⁺ + 6e⁻ \rightarrow 2NH₃ (g)) and NORR (NO (g) + 5H⁺ + $6e^- \rightarrow NH_3 (g) + H_2O)$ offer environmentally friendly pathways for NH₃ production under ambient conditions.

Electrochemical NRR has two possible mechanisms: the associative mechanism and the dissociative mechanism (Fig. 4a). 99,100 The N₂ activation process includes the end-on and side-on configuration, and to simplify, the subsequent hydrogenation of the side-on configuration is not displayed. The associative mechanism involves the reduction of the



(a) Schematic depiction of three mechanisms for NRR. Reproduced with permission. Copyright 2020, Wiley-VCH. 99 (b) $U_{\rm L}$ volcano curves of HER and NRR on metal (111) surfaces. (c) U_1 volcano curves of HER and NRR on metal (211) surfaces. Reproduced with permission. Copyright 2015, Chemistry Europe.53

adsorbed N₂ molecule through generating N₂H₃ intermediates, followed by the breakage of the N=N bond and further reduction to form NH3 eventually. The dissociative mechanism involves the direct breaking of the $N \equiv N$ triple bond in N_2 , resulting in two separated N atoms which then go through individual reductions to form NH₃. In general, breaking the N≡N triple bond is challenging. As a result, the associative mechanism is typically observed in NRR. 101 For most of the catalysts, the conversion of *N2 to *NNH, *NH to *NH2 or *NH2 to *NH₃ is identified to be the potential-determining step (PDS) of NRR in the associative mechanism. 102,103 Considering all the possible elementary steps in the NRR, the Gibbs free energy change of key intermediates (such as ΔG_{*N_2} , ΔG_{*NNH} , ΔG_{*NH_2} and ΔG_{*NH_2} , or $\Delta G_{*N_2 \text{ to } *NNH}$ and $\Delta G_{*N_2 \text{ to } *NH_2}$ is an important factor in determining the NRR performance. In NRR, the atom that interacts with the catalyst surface is always N. Therefore, the interaction strength between the catalyst and the N atom can provide valuable information regarding the efficiency of NRR or NORR; thus the adsorption Gibbs free energy of N (ΔG_{*N}) can be utilized as a descriptor to assess the catalytic activity of the catalysts (Fig. 4b and c).⁵³

The research on NORR has received significant attention recently, because the NO molecule has relatively low activation energy (204 kJ mol⁻¹) compared to N₂ (941 kJ mol⁻¹) and thus would be more easily activated than N2. By performing NORR, NO removal and NH₃ synthesis can be achieved simultaneously, making the process attractive for environmental applications. 69,104,105 Among pure metal surfaces, Cu is considered as one of the best catalysts for NORR since it exhibits both high activity and selectivity. 106 The reaction intermediates and mechanisms observed in NORR are similar to those in NRR. In NORR, there are several possible steps that can serve as the PDS, including *NO + H⁺ + e⁻ \rightarrow *NOH or *NH₂ + H⁺ + e⁻ \rightarrow *NH₃. Additionally, the production of H_2O step (*OH + e⁻ + H⁺ \rightarrow H_2 *O) can also act as the PDS in NORR. 107 The key intermediates involved in these steps can have a great influence on the catalytic efficiency. Recent research conducted by Wu et al. has demonstrated that graphene-based single atom catalysts (SACs) are promising electrocatalysts for NORR. The adsorption of NO on such catalysts provided valuable insight into the catalytic activity of NORR. In particular, catalysts with a moderate ΔG_{*NO} between 0 and -1 eV have been found to be effective in promoting protonation and preventing poisoning. 108 Catalysts with metaldoped α -borophene monolayers (M@BM- α) have been found to exhibit a volcano-shape relationship when correlating $U_{\rm L}$ with ΔG_{*N} for NORR. This suggests that there is an optimal range of ΔG_{N} that leads to the best performance of the catalysts for such reaction.¹⁰⁷ According to the Sabatier principle, the optimal catalytic activity is achieved when there is neither too strong nor too weak binding between the key intermediates and the catalysts; the balanced interaction ensures that the intermediates undergo the necessary chemical transformations without too strong adsorption or desorption. Furthermore, the physical or chemical mechanisms involved in the interaction between the key intermediates and the catalysts play decisive roles in determining the overall reaction efficiency.

2.4. CO₂RR pathway and its key reaction intermediates

CO₂ is an important substance for the regulation of human body fluids. Additionally, plants rely on CO₂ for photosynthesis, through which they convert sunlight, water, and CO₂ into O₂ and glucose, supporting the production of organic matter and enabling the cycling of the organic and inorganic substances in nature. However, excessive CO2 emissions have resulted in significant environmental problems, such as global climate change, ozone layer depletion, acid rain, deforestation, and land desertification. To mitigate the impact of excessive CO2 emission and achieve carbon neutrality, there is growing interest in electrochemical CO₂RR, which aims to convert CO₂ into valuable chemicals under ambient conditions and in aqueous solutions. Electrochemical CO₂RR involves multi-electron transfer pathways, resulting in the generation of various products, including C₁ products (carbon monoxide (CO), CH₄, formaldehyde (HCHO), formic acid (HCOOH) and methanol (CH3OH)) and C2 products (ethene (C₂H₄), acetaldehyde (CH₃CHO), ethanol (C₂H₅OH) and acetic acid (CH₃COOH)) (Fig. 5a). 109-116 In recent years, Cu has emerged as one of the most promising electrocatalysts among pure metals for CO₂RR due to its feasible binding strengths with the key intermediates involved in CO2RR, such as *COOH and *CO. Theoretical and experimental studies have proved that Cu catalysts can yield various products, including hydrocarbons and alcohols. 117-120

Effective CO₂ adsorption is typically considered as a crucial step in the CO₂RR, although its exact nature is subject to debate. One perspective suggests that CO₂ adsorption leads to the formation of CO2 species carrying a unit charge on the adsorbed surface. Alternatively, it has been proposed that *CO₂ adsorption is driven by the interaction between the dipole of *CO₂ and the interfacial electric field, without the existence of *CO2 species. Through an analysis of adsorbate-induced density of states widths, Vijay et al. found that electron transfer to CO2 was facilitated on metal and metal nitrogen-doped carbon catalysts (MNCs), indicating the important role played by the dipole of *CO₂. In addition, their research further revealed that the *CO₂ formation tends to be the rate-limiting step for TMs, while MNCs may encounter limitations related to *CO₂ adsorption or *COOH formation. 123 Therefore, it is important to optimize *CO2 dipoles in the design of CO2RR catalysts. Different products observed in CO2RR can be attributed to the variations in the key intermediates for different catalysts. For instance, late TMs (such as Au, Ag, Zn) tend to bind *COOH more strongly than *CO, thus leading to the production of CO as the main product. Sn, Pb, and Hg tend to interact with O*CHO rather than with the *COOH intermediate, resulting in the HCOOH as the primary product. 124,125 In most instances, the adsorption strength of *CO plays a decisive role in determining the activity and selectivity of CO₂RR, because too strong adsorption of *CO will lead to poisoning of the active sites, while too weak adsorption will cause the desorption of *CO and thus result in lower yield of C₂ products. To achieve optimal selectivity, it is desirable to have a moderate *CO adsorption, which can promote C-C coupling and favor the formation of valuable C2 products (Fig. 5b). 121 This can be

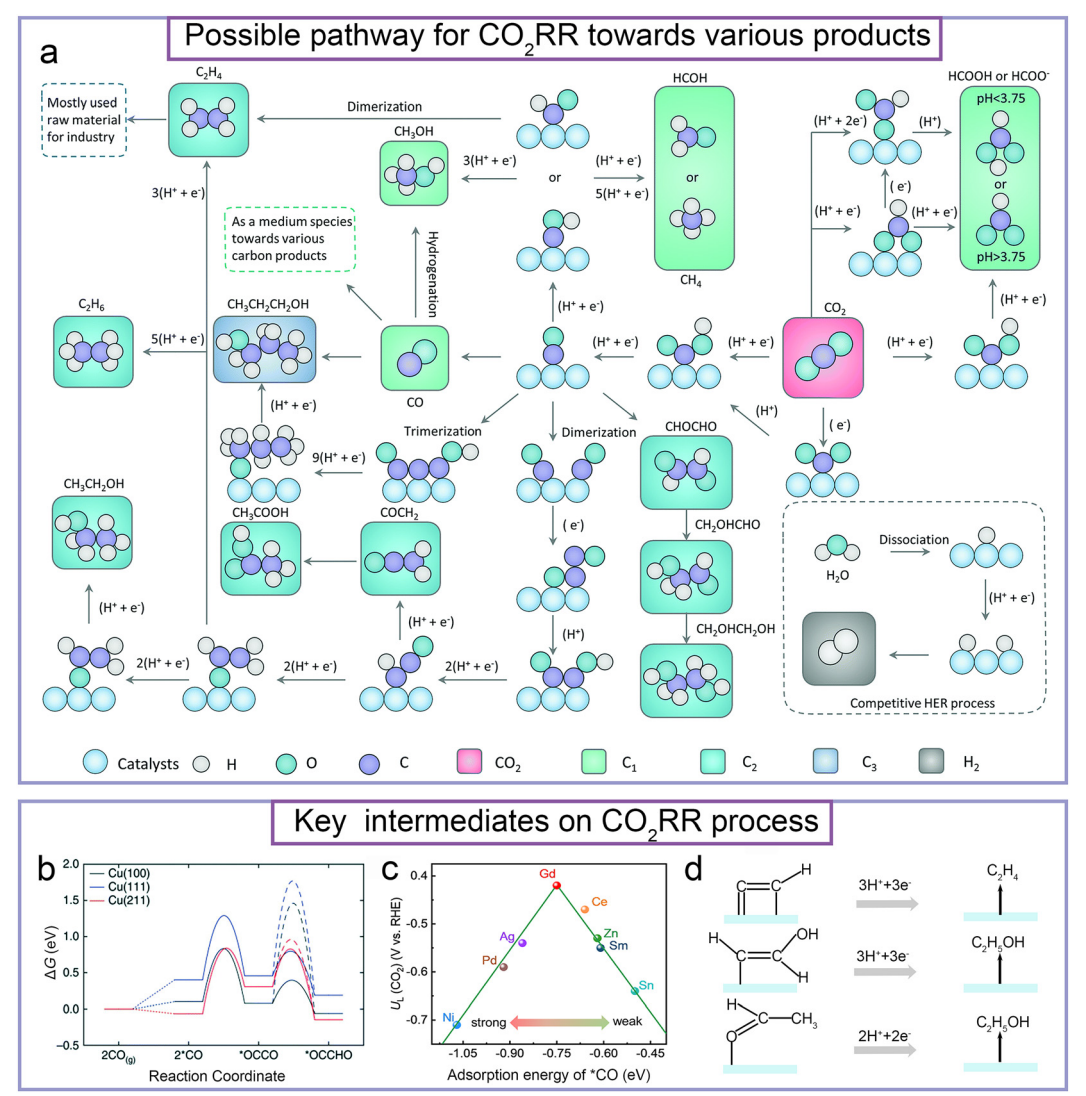


Fig. 5 (a) Mechanism illustration for the CO_2RR process. Reproduced with permission. Copyright 2022, The Royal Society of Chemistry. (b) Free energy diagram at 0 V vs. RHE for the energetics of the dimerization of *CO to form O*C*CO. Reproduced with permission. Copyright 2018, Nature. 121 (c) The volcano curve between U_L and $\Delta G_{\star CO}$. Reproduced with permission. Copyright 2023, American Chemical Society. 122 (d) *C*CH as a key intermediate in the production of ethylene and *CHCHOH and CH3CH*O as key intermediates in the production of ethanol.

achieved by tuning the geometric or electronic properties of the catalysts. For example, doping lanthanide (Ln) elements into Cu₂O can change the lattice constant of the catalyst, which subsequently affected the adsorption strength of *CO. This modification reduced $\Delta G_{*CO-*COCO}$ and finally promoted the catalytic activity of the catalyst (Fig. 5c). 122 In addition to the study of the adsorption strength of CO, the effect of CO coverage on C-C coupling is a topic of ongoing debate. Many works argue that high CO coverage promotes C-C coupling, leading to the production of more multicarbon products. Experimental strategies often involve increasing the concentration of CO or enhancing the adsorption strength of CO through improved catalysts. However, DFT calculations on the Cu(111) and Cu(100) surfaces indicate that high CO coverage leads to significantly weaker CO adsorption, making it unfavorable for the generation of C2 products. 126 C-C coupling is a prerequisite step for the generation of C₂₊ products in the CO₂RR process. It is typically categorized into three main pathways: *CO direct dimerization, *CO and *CHO coupling, and *CHO direct dimerization. In all these pathways, the specific type of *CO hydride formed after C-C coupling plays a crucial role in determining the resulting products. 127 For example, *C*CH serves as a key intermediate in ethylene production, while *CHCHOH and CH3CH*O are crucial for ethanol production (Fig. 5d). In addition, the protonation of the intermediate O*C*CH is an important step that influences the formation of acetic acid and ethylene. By precisely controlling site-selective protonation through adjusting the H affinity, it is possible to stabilize O*C*CH, protect the C=Obonded intermediates from H attack, and selectively generate the acetate product. 128

In summary, intermediates play critical roles in chemical reactions and their Gibbs free energies can serve as fundamental descriptors to correlate catalytic activity. Nevertheless, when considering the same reaction on different catalysts, the key intermediates may be different. Moreover, the key intermediates

corresponding to different products may also differ significantly for the same reactants. Therefore, thorough consideration of all factors and meticulous investigation of different reaction processes are essential in the study of key intermediates in electrocatalytic reactions.

2.5. The influence of solvent effects on electrocatalytic reactions

The significance of electrolyte species in modulating adsorption energies and catalytic activities has garnered increasing attention in recent years. 83,129 Consideration of solvent effects in DFT calculations may lead to different computational results. For example, after incorporating the explicit solvation correction for Pt(111), the *OH binding energy can be stabilized within 0.1-0.3 eV.130 Additionally, the utilization of a semidissociated water layer network on Pt(111) enabled the stabilization of *OOH at approximately 0.5 eV. 131 Recent studies have shown that the inclusion of AIMD and the explicit solvation effect can elucidate the varying performance of M-N-C catalysts in the ORR under different pH conditions. 132 This variation is dependent on different rate-determining steps. For the HER/ HOR, ΔG_{*H} is known to be the main activity descriptor that can accurately predict reaction kinetics on various metal surfaces in acidic electrolytes. However, ΔG_{*H} does not fully encompass the impact of pH on HER/HOR kinetics. Therefore, it is essential to take into account more factors such as solvent type, concentration, and pH to comprehensively investigate and understand the catalytic activity of catalysts in these reactions. As for the

CO₂RR, manipulating the cation ratio of the electrolyte can yield high selectivity for acetic acid at high currents. This is due to the fact that the reduction of interfacial water content within the Helmholtz layer can effectively mitigate the HER activity and decrease the C=O protonation. These processes are influenced by different hydrated alkali metal cations (Na⁺, K⁺, Cs⁺).¹²⁸ Hence, a thorough assessment of various solventrelated parameters, including solvent type and concentration, solvent recombination energies, interfacial electric field strengths, and electrode/electrolyte interfaces, is essential for achieving a comprehensive understanding of the electrochemical reaction mechanism.

3. d-Band center as a descriptor

3.1. d-Band center theory

As is well documented, the d-band center, i.e., the average energy of electronic d states projected onto a transition metal

atom, can be expressed as
$$\varepsilon_d = \frac{\int_{-\infty}^{\infty} n_d(\varepsilon) \varepsilon d\varepsilon}{\int_{-\infty}^{\infty} n_d(\varepsilon) d\varepsilon}$$
, and is widely used

in the field of metal surface catalysis. In the adsorption of simple atoms or molecules onto metal surfaces, the s/p states of the adsorbate interact with the d-band of the surface TM atom, leading to energy level splitting and resulting in the formation of bond states and anti-bond states, as shown in Fig. 6a. 133 As is known, the energy levels of an adsorbate and the catalyst surface lie higher in energy than the bond states but lower than the anti-bond states, meaning that when the anti-bonding

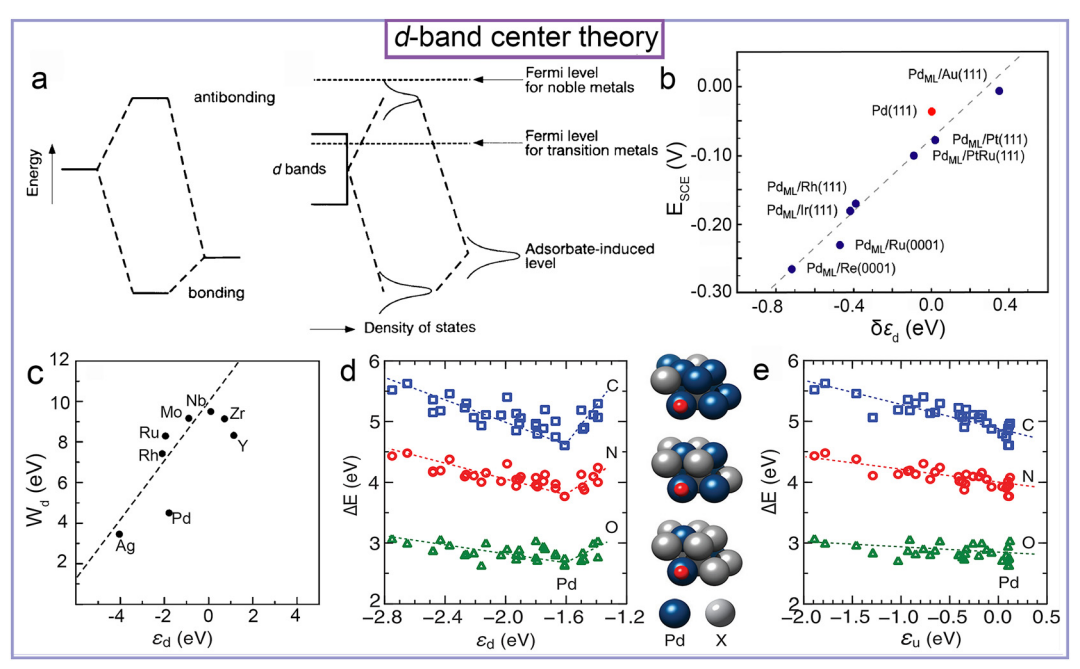


Fig. 6 (a) Schematic illustration of the interaction between two electronic states. Reproduced with permission. Copyright 1995, Springer Nature.¹³³ (b) Electrochemically measured potential (\mathcal{E}_{SCE}) for Pd overlayers on a number of metals as a function of the calculated shift of the d-band center ($\delta \epsilon_0$). Reproduced with permission. Copyright 2011, PNAS.¹³⁴ (c) Variations in the semielliptical width of the density of states distribution as a function of the dband center for the 4d transition metals. Reproduced with permission. Copyright 2013, Springer Link.¹³⁵ (d) Adsorption energies of C, N, and O on the (111) surface (atop site) of Pd and PdX alloys as a function of the ε_d of surface Pd atoms. (e) Adsorption energies of C, N, and O on Pd and Pd alloys with late TMs at 3:1, 2:2, and 1:3 atomic ratios as a function of ε_u . Reproduced with permission. Copyright 2014, American Physical Society. ¹³⁶

state is occupied, the system is energetically unfavorable and thereby destabilizes the adsorption, leading to weak adsorption or even desorption of the adsorbate from the surface, and vice versa. Generally, the s states of the metal are usually delocalized and identical across various metals, whereas the d states are localized and can vary significantly. Therefore, the localized d orbitals play the most important role in determining the interaction between metal aotms and the adsorbates. The higher the d states are in energy relative to the Fermi level (E_f) , the more unfilled are the anti-bonding states and the stronger is the adsorption of the adsorbate on the metal surface. Therefore, it is extremely feasible to modify the interaction between the active sites and the adsorbate by adjusting the d-band center for modulating the catalytic activity. In general, the d-band distribution of the active site can be modified by strain engineering, alloying, phase engineering, etc. This can change the d-band center and, subsequently, affect the adsorption strength. Additionally, the coordination number can also influence the d-orbital interaction, and consequently affect the adsorption energy. Generally, increasing the coordination number strengthens the d-orbital interaction, broadens the d-orbital, and lowers the d-band center, and thereby leads to a smaller adsorption energy.

The d-band model was first proposed by Nørskov et al. and is particularly beneficial for understanding the trends in bond formation and reactivity of TMs. 133 In 2010, Nørskov et al. proved that the experimental results can be well described by a theoretical volcano plot based on the d-band model (Fig. 6b).¹³⁴ However, when describing the interaction between absorbates and metal atoms, only considering the location of the d-band center is not sufficient; it is important to take into account the width and shape of the d-band (Fig. 6c). 135 Hence, based on DFT and the Newns-Anderson model, Nørskov et al. extended the d-band model and showed that bond strength can be accurately defined by the location of the upper edge of the d state. The TMs Ni, Pd, and Pt were identified to be particularly affected by the d-band shape, and the generalized electronic structure descriptor $\varepsilon_{\rm d}$ + $W_{\rm d}/2$ was introduced to account for these effects (Fig. 6d). ¹³⁶ For some TM alloys, the d-band center, even after taking into account the corrections for the d-band width and s/p electrons, may not fully capture the reactivity change from one surface to another. Thus, by studying the high moments of the d-band, the upper dband edge ε_{u} , defined as Hilbert's highest peak position of the Hilbert transform of the density of states projected onto the d orbitals of the active metal sites, was determined for the electron surface activity descriptor (Fig. 6e). 136 The d-band center theory has highly favored and extensively applied in the field of electrocatalysis to explain the interaction between active sites and adsorbates. It has proven to be a valuable framework for understanding and designing electrocatalysts.

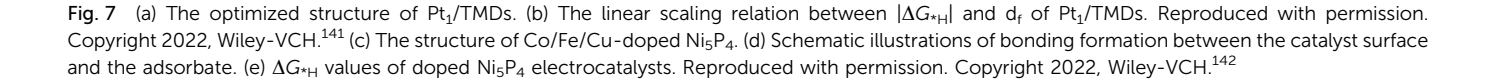
Typically, the determination of d-band centers is carried out through DFT calculations; however, in practical applications, specific absolute values are not necessarily required to assess the adsorption strength of intermediates. The shift of the valence band of an element relative to the $E_{\rm f}$ level following a catalyst change can be ascertained through techniques such as X-ray absorption near-edge spectroscopy (XANES) and ultraviolet photoemission spectroscopy (UPS), where the shift of the valence band corresponds to the shift of the d-band center, providing insights into the adsorption strength of the intermediates. 137,138 Nevertheless, practical challenges may arise from the discrepancies between theoretical calculations and experimental findings. Generally, DFT calculations often simplify catalysts and ignore the external influences, which may lead to deviations in experimental results. In this case, one can consider corrections to the DFT model to account for solvation effects, etc. Alternatively, one can speculate about changes in the d-band center based on the difference in electronegativity between the target atom and the surrounding atoms.

3.2. d-Band center on HER

For HER, the most efficient catalyst is typically the noble metal Pt, which has a very low *H adsorption energy ($\Delta G_{*H} = 0.09 \text{ eV}$). ¹³⁹ *H is known as the key intermediate under both basic and acidic conditions for HER. Thus, modulating the adsorption strength of *H on metal atoms by adjusting the d-band center is an effective way to improve the activity of electrocatalysts for HER. Generally speaking, doping or alloying Pt can both reduce its cost and enhance its catalytic activity for HER. In 2016, Du et al. synthesized trimetallic PtFeCo nanoparticles via an organic-phase process. They found that the d-band center of the Pt atom changed with varying the ratios of Fe and Co atoms within the alloy. Experimental results showed that the current density of the PtFeCo TriStar 3 sample is as high as 1325 mA cm⁻² at a potential of -400 mV, indicating that alloying is an effective method to enhance the HER performance and reduce the utilization of Pt. 140 Additionally, constructing single atom Pt on transition metal disulfides (Pt₁/TMDs) (Fig. 7a) is also a promising approach to reduce costs while maintaining the catalytic activity of the catalyst in the HER. 141 DFT calculations have shown that when Pt is deposited on TMDs, a charge transfer occurs between the Pt and S atoms, resulting in the formation of strong Pt-S bonds. Moreover, the p state of the S atom makes an additional contribution to the catalytic activity of the HER. As such, the generally accepted ε_d failed to explain the HER activity in this system. Thus, they created a new HER descriptor, namely, d-band frontier (d_f), by considering the d-band weights within the energy range of [-1.0 eV, 1.0 eV] on the Pt atom (Fig. 7b). Further, the descriptor can also be extended to Pt single atoms anchored on other supports such as C₃N₄, carbon, molybdenum trioxide, cobalt oxide, etc., suggesting the versatility of this d_f descriptor. 141

Non-noble metal Ni is generally considered inert for HER due to its too strong adsorption for *H. However, by synthesizing the Ni-Cu alloy and changing the surface composition ratio of Ni to Cu to control the ligand effect, the position of the d-band center of the Ni-Cu alloy can be adjusted to be comparable to that of Pt (-1.929 eV with respect to $E_{\rm F}$), making the Ni-Cu alloy a potential alternative to Pt for HER. 143 Another work on Ni-Cu alloys was conducted by Wang et al., which focused on the improved d-band center, especially considering the hollow adsorption sites for *H on Ni-M alloys. In their work, the conventional d-band center is not suitable for describing *H adsorbed on hollow sites, because *H interacts Chem Soc Rev

d-band center for Pt/TMD on HER a Pt₁/HfS₂ 0.4 © 0.4 © 0.3 _∓ ე 0 0.1 $|\Delta G_{H^*}| = -5.3 \times d_{\rm f}$ 0.0 0.12 0.14 0.18 0.20 Pt₄/HfS₂ d-band center for Ni₅P₄ on HER С d Antibonding Antibonding 0.2 0.0 -0.2 H+ + e 1/2 H 0.0 Ads.



Bonding

Bonding

with three metal atoms, forming three M–H bonds. Therefore, they quantified the effect of these three M–H bonds, and established a linear relationship between the improved d-band center and $\Delta G_{^*H}$. The improved d-band center is defined as $\varepsilon_{\rm d} = A \ \varepsilon_{\rm Ni} + (1-A) \ \varepsilon_{\rm M}$, where A is the ratio between the numbers of Ni–H and M–H bond. In addition, the proposed d-band center descriptor is also applicable for trimetallic alloys (Ni–Cu–M). ¹⁴⁴

Ni ● P ● M = (Co/Fe/Cu)

Recently, high entropy alloys (HEAs), comprised of five or more metal elements in roughly equal proportions, have received a lot of attention due to their high thermal stability, good resistance to high temperature oxidation, and adjustable electronic structure. 145-151 Kwon et al. successfully synthesized nanoporous Ir-based HEAs (ZnNiCoIrX, X = Fe, Mn) through dealloying in the vacuum system. They found that when Mn is doped into HEAs, the electronic structure of the Ir site is modified, leading to the d-band center being far away from $E_{\rm F}$, and thus weakening the adsorption strength of the adsorbed intermediates and consequently improving the catalytic activity. Experimental results confirmed that the ZnNiCoIrMn HEA has lower η for HER and OER than its counterparts, suggesting that tuning the d-band center of HEAs through doping with different metals can effectively enhance the catalytic activity. 152 Perovskites have been considered as a promising candidate for electrocatalysis, solar cells, etc. A recent report demonstrated that the LnBaCo₂O_{5+δ} perovskites exhibited excellent catalytic HER properties. Notably, among these perovskites, the one with the O p/Co d-band center that is located far from $E_{\rm F}$ showed the best activity for HER. More importantly, the report highlighted the importance of designing perovskite-based catalysts with appropriate O p/Co d-band centers for enhancing the HER performance. 153

In HER, transition metal carbides, nitrides, sulfides, phosphides, borides, etc. are considered as promising candidates to replace the precious metal Pt. 154,155 It was reported that Co₄N has high activity for OER, while its catalytic HER activity is poor. By introducing heteroatom doping, the d-band center of the Co atom can be tuned and therefore result in different HER catalytic activities. The V-atom-doped Co₄N nanosheets displayed an overpotential of 37 mV at 10 mA cm⁻² for HER, and the increased catalytic activity was attributed to the decreased d-band center. 137 Similarly, Zhang et al. improved the HER performance of Fe₃C in alkaline media by adjusting the d-band center of Fe atoms. They grew Cr-doped Fe₃N structures on nitrogen-doped graphene and observed a lower η compared to the pristine Fe₃C. DFT calculations illustrated that Cr doping reduced the d-band center of the Fe atom, thus optimizing the HER performance. 156 Furthermore, introduction of holes in the CoP nanosheets can also optimize their catalytic performance for HER. DFT calculations revealed that the valence electron numbers of the d-band center and Co sites around the holes are shifted upward, resulting in a change of the ΔG_{*H} of the Co atoms surrounding the holes. ¹⁵⁷ In 2019, Li et al. demonstrated that ruthenium diboride (RuB2) is the most competitive HER catalyst among diborides through theoretical calculations; it exhibited a catalytic activity comparable to that of Pt. The high HER activity of RuB₂ was further experimentally verified in both acidic and alkaline environments. Furthermore, the study revealed a linear relationship between the catalytic activities of various metal diborides and their d-band centers. 158 Another study investigated the catalytic performance of Ni₅P₄ nanosheets manipulated by heteroatom doping, especially with Fe and Co atoms (Fig. 7c). The doped Ni₅P₄

Reaction Coordinate

catalysts were found to exhibit different HER performance according to theoretical calculation results (Fig. 7d). Compared with Fe-doped, Cu-doped, and pristine Ni₅P₄, the Ni₅P₄ nanosheets with appropriate Co doping demonstrated the best electrocatalytic performance, with the lowest overpotential of 100.5 mV at 10 mA cm⁻² for HER. The enhanced activity was attributed to its moderate position of the d-band center, which contributes to moderate anti-bonding filling (Fig. 7e) and thus promotes the adsorption and desorption processes of H atoms on the catalyst surface. 142 Wang et al. designed and synthesized a series of lattice-strained homogeneous NiS_xSe_{1-x} nanosheets@ nanorods hybrids for HER/ORR. 159 Among various compositions, the NiS_{0.5}Se_{0.5} sample with approximately 2.7% lattice strain exhibited the best catalytic performance for both HER and OER, with an extremely low overpotential of 70 mV for HER and 257 mV for OER at 10 mA cm⁻². In addition, it also displayed a good long-term durability for 300 h at a high current density of 100 mA cm⁻². Experiments and theoretical calculations revealed that the lattice strain reduced the d-orbital overlap of the metals, resulting in narrowing of the bandwidth of the dband and bringing the d-band center closer to $E_{\rm F}$. Therefore, NiS_{0.5}Se_{0.5} has the optimal *H adsorption kinetics for HER and the lowest energy barrier for OER. All the above results demonstrate that the adsorption strength of *H on metal active sites can be optimized by adjusting the d-band center. The crystallineamorphous CoSe₂/CoP heterojunction has also been demonstrated to be active for HER. This heterojunction showed a reduced HER kinetics barrier, which was attributed to the strong electronic coupling at the interface that lowered the d-band center of the Co atom, leading to the feasible adsorption of *H.160 The MoS₂ basal plane is generally inert for HER catalysis; however, its electronic structure can be tuned by introducing dopants, defects, or strain, which can significantly enhance the HER catalytic activity. Yang et al. studied the defective MoS₂/ graphene catalysts and demonstrated that the d-band center of the metal is a good descriptor for evaluating the adsorption strength of *H under different strain conditions. 161 Kwon et al. synthesized ternary alloy nanosheets MoSe₂-VSe₂-NbSe₂ through a hot-injection colloidal reaction. They found that these ternary alloys exhibited higher electrocatalytic activity for HER compared to binary alloys when tested in an acidic electrolyte. They also revealed a volcano-type relationship between the HER performance and the d-band center of the alloys, where the d-band center was determined based on synchrotron radiation X-ray photoelectron spectroscopy valence band spectra. 162

3.3. d-Band center on OER and ORR

The intermediates involved in OER and ORR are similar and include species such as *O, *OH, and *OOH. The d-band center is an effective descriptor for evaluating the adsorption energy of O-containing species and assessing the catalytic performance. As a representative, Lu et al. determined the relationship between *O adsorption energy and d-band center in single crystal metal films.163 The design of catalysts for ORR based on the d-band center theory has been widely discussed, particularly in the case of Pt and Pt-based alloys. For instance, in order to search for

more efficient catalysts for ORR, Nørskov et al. constructed Pt₃M alloys to modify the electronic structure of Pt. DFT calculations revealed that the position of the metal d-band relative to $E_{\rm F}$ determines the strength of the bond between O and the metal, which in turn affects the catalytic activity. 164 Toyoda et al. studied the size effect of Pt nanoclusters on the catalytic activity for ORR. They observed that the d-band centers of Pt with different sizes are linearly related to the ORR catalytic activity, which is consistent with the d-band center theory. The smaller size of the Pt nanocluster makes the d-band center closer to $E_{\rm F}$, and thereby leads to lower catalytic activity. 165 In 2018, Ando et al. designed a series of PtPb-ordered intermetallic nanoparticles (NPs) deposited on TiO₂/cup-stacked carbon nanotube (PtPb NPs/TiO₂/CS) catalysts for ORR. Interestingly, they demonstrated that the current density of the electrochemically de-alloyed PtPb NPs/ TiO2/CS catalysts and the d-band center of the Pt atom exhibited a volcano relationship. 166 To minimize the cost and the metal utilization, and to further enhance the catalytic ORR activity, they deposited Pt NPs on a series of transition metal oxides (MOx, M = Ti, Nb, Ta, W, Y, and Zr) and composites $(M_1M_2O_x; M_1M_2 = TiNb,$ NbTa, and TaW). 167 They also observed a "volcano-type" correlation between ORR activity and the d-band center in this system. 167 More importantly, they found that the electron transfer from metal oxides to Pt NPs can result in an increase in the electron occupation of Pt atoms, leading to a decrease in the d-band center of Pt atoms, and thus making the facile adsorption of different oxygen-containing intermediates in ORR. Therefore, the catalytic activity of Pt can be modulated by adjusting its metal oxide substrates or tuning its local coordination. Likewise, introducing the Bi atom to form a PtBi(100) alloy can also influence the electron transfer between Pt and Bi atoms, resulting in a higher catalytic activity compared to Pt(111). The enhanced catalytic activity arises from the downward shift of the d-band center of Pt atoms, which is caused by the stretching strain induced by the introduction of Bi. 168 In the past few years, doping p-block heteroatoms or constructing p-block elements as ligand atoms to the active sites have been popular approaches to improve the catalytic activity of catalysts for ORR, because the p-block elements possess abundant lone electrons and can tune the electronic structure of the considered metal atoms. Zhu et al. designed and compared the intrinsic ORR activities of the PtN_r and PtNx-PO catalysts through a combination of theoretical calculations and experiments. By coordinating P atoms to Pt-N moieties, the d-band center of Pt in Pt-N-C becomes lower, which consequently optimizes the binding strength between Pt atoms and the ORR intermediates, finally resulting in the designed Pt-NO catalyst exhibiting superior ORR activity. 169

The electron transfer process during the OER can occur through two mechanisms: adsorbate evolution mechanism (AEM) and lattice oxygen oxidation mechanism (LOM) (Fig. 8a). 65,170,171 In the AEM, the reaction occurs at the surface of the catalyst, where oxygen species are adsorbed on the metal surface and undergo a series of oxidation reactions. In the LOM, the lattice oxygen within the bulk of the catalyst participates in the electron transfer process. 172,173 Balancing the adsorption and desorption of oxygen-containing intermediates is essential for optimizing

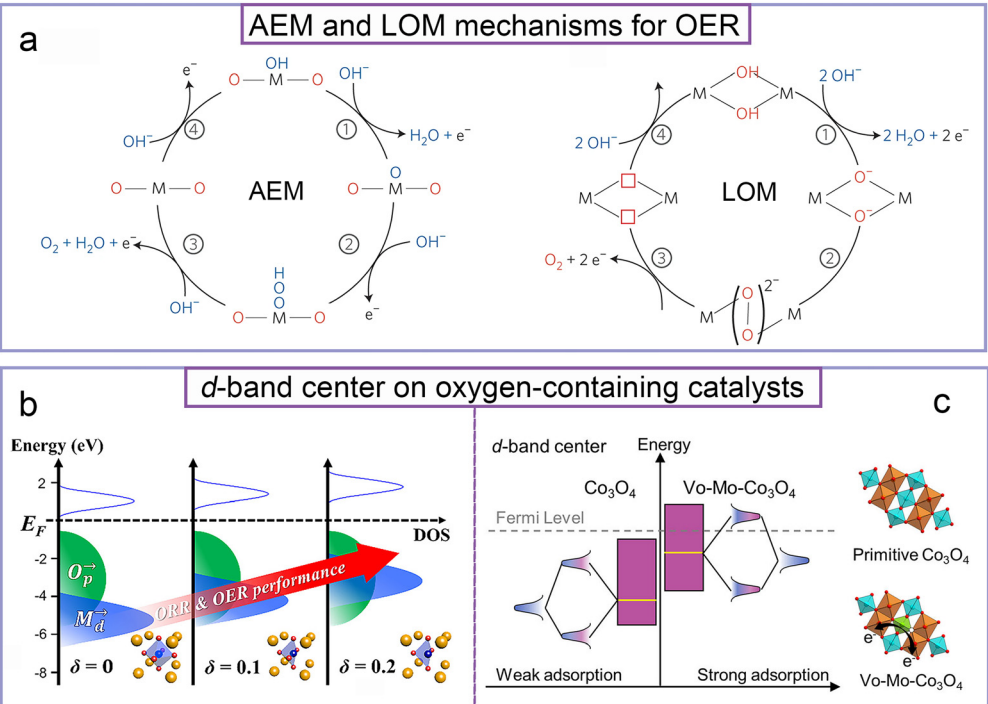


Fig. 8 (a) The AEM and LOM mechanisms for OER. Reproduced with permission. Copyright 2016, Nature. (b) The reduced gap between d- and pband centers (ΔE_{d-p}) and correspondingly increased OER/ORR performance on perovskite oxides of $Sm_{0.5}Sr_{0.5}CoO_{3-\delta}$. Reproduced with permission. Copyright 2020, American Chemical Society. 176 (c) Schematic illustration of the effect of Mo doping and O vacancies on the d-band center of Co₃O₄. Reproduced with permission. Copyright 2022, Wiley-VCH. 177

the OER process following the AEM mechanism. This balance is crucial for maximizing the effectiveness of OER catalysts, necessitating the presence of the optimal d-band center in the electrocatalysts. 174 In contrast, for reactions following the LOM mechanism, metal atoms with minimal electronegativity difference from oxygen are usually preferred. This characteristic enables the feasible intramolecular electron transfer from the oxygen ligand to the TM cation, leading to a negative metal dband center relative to the O-2p band center ($\varepsilon_{\text{TM-d}}$ – $\varepsilon_{\text{O-2p}}$). This provides a prerequisite for lattice oxygen redox chemistry to occur. 175 Thus, the influence of the d-band center on the OER activity of catalysts under the LOM mechanism primarily manifests through alterations in the band distribution of TMs to influence the lattice oxygen activation.

Therefore, oxygen-containing catalysts thus play an important role in facilitating the OER. 178-183 There have been extensive studies on the oxide catalysts for OER. In the research on V-doped LaCoO₃ (V-LCO), it was observed that the closer the d-band center to the $E_{\rm F}$ of the Co atom after doping, the stronger the bond strength between the adsorbate and the catalyst and thereby the better OER activity.¹⁷⁸ Luo et al. theoretically calculated and experimentally verified that Fe-doped Ni₃Ge₂O₅(OH)₄ is a superior OER catalyst among serpentine germanane materials. Doping Fe³⁺ allowed for fine-tuning of the d-band center of the Ni₃Ge₂O₅(OH)₄ serpentine, which optimized the binding strength of the intermediate with the surface Ni and Fe atoms, leading to an effective alteration in the OER catalytic activity.¹⁸⁴ Some studies have suggested that the difference between the metal d-band center and the oxygen p-band center (ΔE_{d-p}) can serve as a descriptor in describing the OER catalytic activity of transition metal oxides. 185-187 For example, Lee et al. investigated the OER and ORR catalytic activities of the oxygen vacancy modified perovskite catalysts. They found that the metal d-band center (M_d) values of the perovskites with early TMs (Cr, V, and Mn) are higher than their O p-band center (O_p) values, while the perovskites with late TMs (Co, Ni, and Cu) have lower M_d values than the O_p values. This implies that changing the d-band center can modulate ΔE_{d-p} and thereby alter the OER/ORR performance (Fig. 8b). DFT calculations verified that introducing the surface oxygen vacancies can also modulate $\Delta E_{\rm d-p}$ and thereby effectively tune the adsorption strength of the intermediates and contribute significantly to the OER activity. 176 Xu et al. proposed that the relative positions of the O p-band center and the MO_h (Co and Ni in octahedra) d-band center in spinel oxides $ZnCo_{2-x}Ni_xO_4$ (x = 0-2) are correlated with their stability and different reaction mechanisms. Based on this, they predicted ZnCo_{1.2}Ni_{0.8}O₄ as a high-activity catalyst, which has been experimentally verified. In addition, they found that Ni substitution can adjust the relative position between the O p-band center and the MO_h d-band center in ZnCo₂O₄, leading to changes in the reaction mechanism and enhancement in the OER activity. 188

The rational introduction of oxygen vacancies can alter the electronic properties of the active sites, which in turn affects the binding strength of the OER and ORR intermediates to the active sites. Zhang et al. studied the amorphous/crystalline RuO2 with rich oxygen vacancies for OER. They attributed the

high activity of the catalyst to the downshifting d-band center relative to $E_{\rm F}$, which leads to a weakening of the chemical bond between the oxygen-containing intermediate and the RuO2 surface, thus lowering the activation barrier for the OER. 189 Yang et al. comprehensively studied the bifunctionality of LaCoO₃ with oxygen vacancies for both OER and ORR through DFT calculations. They confirmed three criteria: (i) oxygen vacancies can change the d-band center of Co atoms and the p-band center of O atoms, i.e., ΔE_{d-p} , (ii) the AEM reaction mechanism usually occurs at the Co active site when the oxygen vacancy locates at the sublayer, and (iii) the reduced desorption energy for *O leads to increased ORR activity and the cobalt and oxygen vacancies react synergistically in promoting the ORR process.¹⁹⁰ Huang et al. synthesized oxygen vacancy enriched Mo-substituted Co₃O₄ hierarchical porous nanoneedle arrays on carbon cloth (P-Mo-Co₃O₄@CC) by an Ar-plasma-assisted method. They mentioned that the Mo atom substitution can effectively regulate the atomic ratio of Co³⁺/Co²⁺ in the structure and increase the number of oxygen vacancies, leading to electron transfer and regulating the d-band center of Co₃O₄ (Fig. 8c), subsequently improving the adsorption energy of oxygen intermediates (e.g., *OOH) on P-Mo-Co₃O₄@CC. ¹⁷⁷

Apart from the oxygen vacancies, strain engineering also plays a key role in tuning the electronic structure of materials. Extensive works have shown that employing strains can indirectly change the binding strength between the active site and the intermediate, which in turn promotes the activation of molecules and thereby the catalytic activity of materials. Zhang et al. proved that the increased compressive strain induced by the folded nanostructures can weaken the binding strength of the adsorbed oxygen-containing substances and accelerate the kinetics process of the ORR, which in turn leads to a high catalytic activity for highly wrinkled Pd nanosheets. 191 P, N, and S can be used as non-metal dopant atoms in oxides, because they have similar properties to the O element. Cui et al. studied P-doped MoO2 and demonstrated that the P-doping raises the d-band center of MoO₂, which enhances the interaction between MoO2 and the associated oxygen-containing intermediates during ORR/OER, and thereby improves the catalytic activity of the material. Furthermore, they assembled zinc-air batteries with P-MoO2 as the cathode material, which exhibited excellent charge and discharge performance. 192

In recent years, SACs have received increasing attention in catalysis due to their wide range of active sites and large specific surface areas. In addition, non-planar axial ligand atoms are also creeping into the limelight, which can change the electronic properties of the reaction sites and improve the catalytic activity. Wang et al. studied the atomically dispersed penta-coordinated-Zr catalyst with the axial oxygen ligand for ORR and confirmed the effect of oxygen ligands on the active center. They uncovered that the reduced d-band center of Zr caused by the oxygen axial ligand can result in a stable local structure and proper intermediate adsorption capacity at the Zr site. As a result, the ORR performance of Zr-N-C-O significantly exceeds that of the commercial Pt/C catalyst, achieving a half-wave potential of 0.91 V and excellent durability (92% current retention after 130 h) for ORR. 193 Li et al. studied the Nd-doped RuO2 catalyst for OER under an acidic condition. Theoretical calculations showed that the d-band center of the Ru atom in the doped structure was shifted downward, resulting in a balance in the adsorption and desorption of OER intermediates. In addition, experiments showed that the dissolution of RuO2 was suppressed after the introduction of Nd, indicating that Nd can improve the acid resistance of RuO2. 194

3.4. d-Band center on NRR

The intermediates involved in the NRR primarily consist of N-containing species. Generally, a stronger adsorption of reactants occurs when the d-band center is closer to $E_{\rm F}$. Therefore, the d-band center of the catalyst can accurately assess the adsorption by simplifying N-containing species to N. For NRR, the activation of N2 is the main issue because N2 is an inert molecule. Nowadays, most of the electrocatalysts concentrating on the d-band center for NRR are mainly ultrathin twodimensional (2D) materials, because 2D catalysts have great atomic utilization because of their large specific surface area and can activate N2 efficiently in the NRR. The successful exfoliation of graphene in 2004 has sparked the interest in exploring 2D materials. 195 One common approach to create a 2D material model based on graphene is by substituting C atoms with N atoms and loading TMs onto the N sites, resulting in M-N-C structures. Such materials have been widely used in HER, ORR, OER, NRR, and CO₂RR. 196-198 The d-band centers of the active sites in these materials can be altered by adjusting the central metal atoms, the number or type of the surrounding atoms, as well as by doping or stress design, consequently leading to changes in the adsorption energy of N-containing intermediates. Lin et al. studied the mechanism of regulating the electronic state of the active center in SACs. Specifically, they examined the catalytic behavior of the N₃-graphene materials with the embedded Cr atom for NRR (Fig. 9a). By manipulating the coordination bond length between the Cr atom and the surrounding N atoms, the d-band center of the Cr atom within the SAC can be altered, which in turn affects the antibonding orbitals by changing the interaction between the N and Cr atoms (Fig. 9b and c). They also discovered that applying a stretching strain of 2.5% onto the N₃-graphene materials with the embedded Cr atom can induce a change in the spin polarization state of the Cr atom, making it transit from the high spin state to the ground spin state. The change in spin polarization modulates the adsorption strength of N₂ to a moderate level, resulting in reduced η and improved catalytic activity for NRR. ¹⁹⁹ Likewise, the catalysts with homogeneous double TMs supported by N-doped graphene (TM₂N₆@graphene) were analyzed by DFT calculations. Among the 20 different TM catalysts, Fe₂-N₆@G, Ru₂-N₆@G, and Ir₂-N₆@G were identified as highly active catalysts. Furthermore, they found that the first protonation step is generally the PDS. Specifically, they uncovered that the d-band center, within an energy range from 0 to 2 eV, can serve as a descriptor for evaluating the NRR performance $(U_{\rm L})$ of the aforementioned materials, following a volcano relationship. Finally, the accuracy of the descriptor is justified by the crystal orbital Hamiltonian population (COHP) and the orbital interaction analysis. 200 In addition to N coordination, Genç et al. investigated the influence of different

Chem Soc Rev d-band center for strained CrN₂-graphene on NRR

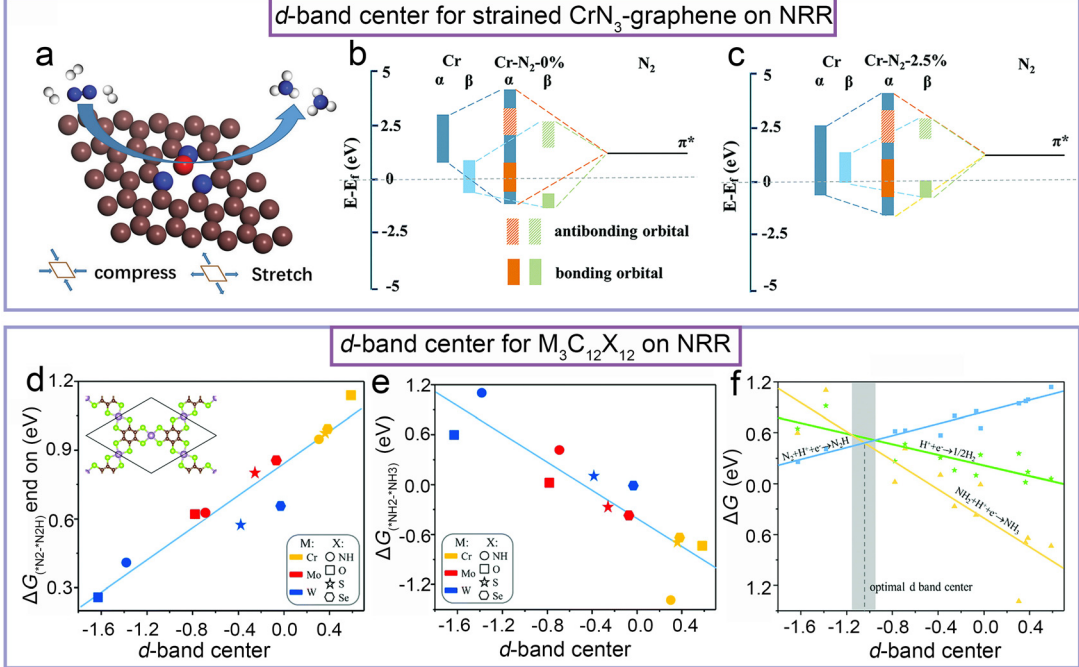


Fig. 9 (a) The schematic diagram of the NRR for CrN₃@graphene. (b) and (c) The interaction between Cr-3d and N₂-2p on (b) pristine and (c) lattice strained (2.5%) CrN₃@graphene. Reproduced with permission. Copyright 2021, The Royal Society of Chemistry. 199 (d) and (e) The linear relationship between the d-band center of M and the ΔG of key reaction steps in NRR on the proposed $M_3C_{12}X_{12}$. (f) The volcano curve between the d-band center and the ΔG of PDS. Reproduced with permission. Copyright 2021, The Royal Society of Chemistry. ²⁰²

amounts of O atoms replacing N atoms on the properties of MnN_xO_y in terms of stability, N_2 adsorption, and NRR activity. They found that with increasing oxygen content, the Mn-O interaction weakened compared to Mn-N, the bonding orbitals became reduced, and the anti-bonding orbitals between Mn-N-O atoms were partially occupied, which can be explained by COHP and the integrated crystal orbital bonding index (ICOBI). Furthermore, they proposed that the MnNO₃ layer has the best N2 adsorption energy, which is mainly due to it having more d-bands near $E_{\rm F}$ compared to other coordination environments.201

The doping of graphene with N atoms to form a graphene-like C_xN_y structure as a catalyst has received considerable attention in recent years. Two commonly used examples of such catalysts are g@CN and g-C₃N₄. Recently, Yu et al. developed a novel Ru-loaded g-C₃N₄ catalyst. Through experimental characterization, they demonstrated that the considered catalyst has high activity for NRR in strong alkaline electrolytes with an NH3 yield of 23.0 μg mg $_{cat}^{-1}$ h^{-1} at 0.05 V and a Faraday efficiency (FE) of 8.3%. Through DFT calculations, they compared the NRR process of the synthesized material with bulk Ru, and revealed that the activity of the Ru-loaded g-C₃N₄ catalyst originates from the altered d-orbital energy, which results in moving the d-band center toward E_E. ²⁰³ In 2021, Li et al. constructed three Mn-based SACs, namely Mn@g-CN, Mn@C₃N₄, and Mn@g-N₄. Among these, Mn@g-N₄ has the largest η for electrocatalytic NRR (0.75 V). After introducing heteroatoms (F, P, and S) and imposing strain engineering, the dband center energy of the central Mn atom significantly reduced, resulting in the improved performance for electrocatalytic NRR.204

Recently, researchers have designed several materials with structure similar to traditional graphene-like carbon and nitrogen compounds. For instance, Zhang et al. designed a series of TM SACs anchored on a π - π conjugated graphitic carbon nitride (g-C₁₀N₃) substrate with Dirac dispersion and good conductivity through DFT calculations. They applied a high throughput screening from 27 candidates to evaluate their NRR activity and predicted that W@g- $C_{10}N_3$ is a promising catalyst with a U_L of only -0.46 V. They explained the origin of its catalytic activity in terms of d electron number and electronegativity.205 In recent years, the development of machine learning (ML) techniques has revolutionized catalyst screening and descriptor selection. ML algorithms can efficiently analyze large amounts of data and establish correlations between catalytic activity and various parameters. This allows researchers to rapidly identify the most influential factors that govern the catalytic performance. Mukherjee et al. applied a combination of machine learning and DFT calculations to predict Ta-based C6N6 as the best candidate material for NRR. In their machine learning regression model, they identified the covalent radius and d-band center of TM as the most relevant descriptors to correlate the N₂ adsorption energy.²⁰⁶ Another new class of electrocatalysts, TM@g-C₄N₃, is also used to assess the NRR activity and unveil the underlying mechanism of nitrogen fixation. Through high throughput screening and DFT calculations, Wang et al. systematically investigated the NRR activity of 3d, 4d, and 5d TM embedded g-C₄N₃ catalysts and identified four good catalysts through a five-step screening. Interestingly, they found that the onset potential (U_{onset}) and the adsorption energy of N_2

 $(\Delta E_{ads}(*N_2))$ showed a volcano-shape relationship, and thus $\Delta E_{\rm ads}(*N_2)$ can be used as a descriptor to correlate the catalytic activity of NRR. Through an in-depth analysis of the readily accessible intrinsic properties of the best four selected catalysts, they revealed that the order of increase in activity is consistent with the order of increase in the d-band center of the catalyst.²⁰⁷ Quan et al. designed 12 TM SACs on g-C₃N₅ nanosheets (TM-g-C₃N₅) to explore their underlying mechanism for NRR. Through a three-step screening process based on stability, activity and selectivity, V-g-C₃N₅ was identified as the best electrocatalytic NRR catalyst among 12 TM-g-C₃N₅ catalysts with an onset potential of -0.30 V. For V-g-C₃N₅, the process of *N₂ \rightarrow *N₂H is considered as the PDS, meaning that $\Delta G_{*N,H}$ is the key factor in evaluating the overall NRR activity. Interestingly, the d-band center is linearly correlated with $\Delta G_{*N,H}$, indicating that the d orbit of the considered catalysts is also an important factor in evaluating the NRR activity.208

2D metal-organic frameworks (MOFs) have attracted significant attention in the field of electrochemical reactions due to their unique properties and advantages, including high conductivity, chemical tunability, easy synthesis, and facile accessibility to active sites. M₃C₁₂N₁₂, also known as MOF-235, is a commonly studied MOF with a well-defined structure. Researchers have explored different variations of M₃C₁₂N₁₂ by varying the central metal atoms and the coordinating atoms. In 2021, Wang et al. constructed various $M_3C_{12}X_{12}$ catalysts with X = O, S, and Se, and evaluated their NRR performance (Fig. 9d). In their research, * $N_2 \rightarrow N_2H$ or * $NHH \rightarrow NH_3$ is considered as the PDS, and interestingly, $\Delta G_{\text{N}_2 \rightarrow \text{N}_2 \text{H}}$ and $\Delta G_{\text{NHH}} \rightarrow \text{NH}_3$ exhibited an inversely proportional relationship. In addition, the d-band center of $M_3C_{12}X_{12}$ has a linear relationship with the ΔG of the PDS for NRR (Fig. 9d and e). Therefore, the d-band center can be taken as a good descriptor to evaluate the NRR activity of these catalysts (Fig. 9f).²⁰² In 2023, a study focused on investigating the influence of p-d orbital hybridization on electrocatalytic NRR was conducted using $M_3C_{12}X_{12}$ MOFs with X = O, S, Se, and NH and with different central metal atoms including Os, Ru, and Ir.²⁰⁹ The study reported that the strength of the hybridization interaction between the appropriate metal-d and intermediate atom-p orbitals is a key indicator of the NRR catalytic activity. Additionally, the strength of hybridization interactions can be quantitatively calculated by the p-d band central energy difference (Δ_{d-p}), which is a powerful descriptor to correlate the p-d hybridization strength with NRR performance. As a result, a volcano relationship between the maximum free energy change (ΔG_{max}) and $\Delta_{\text{d-p}}$ was obtained, and the $OsC_4(Se)_4$, IrC_4O_4 , and $RuC_4(Se)_4$ catalysts located at the top of the volcano curves were proved to have better NRR performance.209

TMDs, abbreviated as MX_2 (M = Mo, W, etc.; X = S, Se, Te), have attracted a lot of attention worldwide due to their 2D layered structure, which is similar to graphene. Doping TMs into ReS2 nanosheets is also a reliable method to simultaneously improve nitrogen fixation and suppress competitive HER. The catalyst with Fe-doped ReS2 nanosheets wrapped around nitrogen-doped carbon nanofibers (Fe-ReS2@N-CNF) has the best electrochemical activity with an NH₃ yield of 80.4 µg h⁻¹ mg_{cat}⁻¹, along with an

overpotential as low as 146 mV and a Tafel slope of 63 mV dec⁻¹. Through DFT calculations, it was interpreted that the dopant atoms provided more active sites and electron transfer for ReS₂, which caused the d-band centers move towards $E_{\rm F}$, thereby changing the adsorption strength of the intermediates, and consequently achieving different catalytic activities. 210 Similarly, VSe2 with abundant Se vacancies also exhibited high NRR performance, which is attributed to the increase of the d-band center of V atoms induced by the Se vacancy. This can promote the binding of key *N₂/*NNH intermediates to the active site, resulting in an energetically favorable NRR process.211

The construction of heterojunctions allows for different interfacial charge transfers for the purpose of changing the electronic properties of the surface. In 2021, Liu et al. reported the FeNi₂S₄/NiS heterogeneous structure, which effectively promoted N₂ adsorption in NRR and inhibited the competitive HER. Its NH₃ yield and FE reached up to 128.398 \pm 1.32 μ g⁻¹ h⁻¹ cm⁻² and 28.64 \pm 0.18%, respectively. Both experimental results and DFT calculations indicated that the enhanced electrocatalytic performance and selectivity of the FeNi2S4/NiS heterostructure for NRR were attributed to the changes in the d-band center and the electronic structure of the catalyst surface. 212 In 2022, Guo et al. designed a novel structure of WO3 in contact with TMDs, including MoS₂, MoSe₂, WS₂, and WSe₂, and validated their potential as the NRR electrocatalyst. The WO₃/MoS₂ heterostructure was identified as an optimal catalyst with a low onset potential of 0.25 V, which is attributed to its elevated d-band center that effectively modulated the adsorption strength of intermediate adsorbates.²¹³ In 2022, Biswas developed a Lewis acid-dominated aqueous electrolyte as a co-catalyst to overcome the N2 activation problem on the catalyst surface. N₂ adsorption is the first and the most critical step in NRR. DFT calculations have shown that the BF3-induced charge polarization can shift the metal d-band center of the MnN₄ moiety closer to $E_{\rm F}$, and thereby facilitate the N₂ activation. The free BF₃ molecule displays Lewis acidity, further suggesting that it can facilitate the N≡N bond polarization as well as the first protonation step. In addition, the change in the d-band center can effectively reduce the PDS energy of the NRR. As a result, a high NH₃ productivity can be achieved using the MnN₄/BF₃ catalyst, with a rate of 2.45×10^{-9} mol s⁻¹ cm⁻², which is comparable to the yields achieved in the industrial NH₃ production process.²¹⁴

3.5. d-Band center on CO₂RR

CO₂RR is one of the representative examples in electrochemical reactions with complex and diverse product outcomes. It can produce a wide range of products depending on the reaction conditions and the catalysts. The most common C1 products include CO, HCOOH, and CH₃OH. For CO₂RR, the interaction strength between key intermediates (e.g., *CO, *COOH, H*COO) and the catalyst surface, i.e., the adsorption energy, is considered to be a key determinant of the reduction products and reduction activity.215 *COOH is identified as the key intermediate of CO production on metal surfaces, while H*COO is the key intermediate of HCOOH production. The adsorption energy of *CO (ΔE_{*CO}) is a key factor that determines whether *CO participates in CO production or undergoes further hydrogenation. Generally,

when ΔE_{*CO} is greater than -0.5 eV, it indicates a relatively weak adsorption of *CO and thus favors CO release from the catalyst surface. When ΔE_{*CO} is less than -0.5 eV, it suggests a stronger adsorption of *CO and thus it would more likely undergo further dehydrogenation reactions to produce hydrocarbons. 122 The dband position of the active site on the metal surface affects the adsorption strength between the metal atom and the reaction intermediate, which in turn influences the catalytic activity. In 2007, Wang et al. explored the factors affecting the adsorption of CO2 on TM surfaces on the basis of DFT calculations. In their work, the CO₂ binding energies ($\Delta E_{\rm b}$) exhibited linear relationships with the d-band centers and the transferred charge (q), which were proposed as descriptors to correlate the chemisorption of CO₂. 216

For CO₂RR, selectivity is by far the most significant and urgent challenge in this field. Among pure metals, Cu has attracted much attention due to its unique selectivity for CO₂RR. In addition, various Cu-based alloys have been developed to further improve the catalytic activity and selectivity towards specific products. Rasul et al. prepared copper-indium (Cu₁₁In₉) alloys by electrochemical deposition of In on rough Cu surfaces and achieved efficient and selective reduction of CO2 to CO. The upward shifted d-band center of the Cu atoms induced by doping In atoms attributed to the improved catalytic activity. 217 In 2017, Clark et al. reported electrochemical CO2RR at a CuAg bimetallic electrode, which exhibited higher selectivity towards multi-carbon products compared to a pure Cu electrode. The introduction of Ag resulted in a compressive strain on the neighboring Cu atoms, which shifted the d-band distribution of Cu to a deeper energy level. This modified electronic structure of Cu was found to be beneficial for reducing the binding energies of *H and *O compared with *CO intermediates, thus effectively suppressing the competitive HER and increasing the selectivity towards CO-derived products. Furthermore, the strain effects induced by Ag introduction can also reduce the adsorption of *H species and decrease the bond strength of the Cu-O bond, consequently contributing to enhanced selectivity towards multicarbon products. This work provided an effective way to modify the CO₂RR selectivity in order to generate multi-carbon oxygenated products.²¹⁸ Ren et al. synthesized isolated Sn sites with a high surface density (up to 8%) anchored on Cu hosts (denoted as Cu-Sn NPs) (Fig. 10a) through a simple one-step reduction method. In an alkaline electrolytic cell, the Cu₉₇Sn₃ catalyst achieved a FE of 98% for CO production at a tiny overpotential of 30 mV. A high CO current density of 100 mA cm⁻² can be achieved on this catalyst at an overpotential of 340 mV. DFT calculations demonstrated that the PDOS of the d-orbitals of Cu in Cu-Sn alloys shifted to deeper energy levels and the d-band centers for Cu-Sn alloys are farther away from E_F, making the *COOH and *OCHO species interact with the metal surface weakly, which improves the $U_{\rm L}({\rm CO_2})$ – $U_{\rm L}({\rm H_2})$ of CO production, and therefore achieves a better CO₂RR activity (Fig. 10b and c).219

At present, Cu-based alloys are considered as the state-of-theart CO₂RR catalysts; some other non-noble metal alloys have also been explored as promising catalysts for CO2RR. For example, ultra-thin Rh₇₅W₂₅ alloy NPs have been successfully prepared by Zhang et al., which exhibited better performance than the Rh nanosheets (NSs) and Rh73W27 NPs for catalytic CO2 hydrogenation to CH₃OH. According to DFT calculations, the Rh₇₅W₂₅ NSs exhibit higher d-band centers (Fig. 10d), thus enhancing the adsorption and activation of CO2. Correspondingly, the experimental results showed that Rh₇₅W₂₅ NSs exhibited the highest methanol yield (Fig. 10e).220

For pure metallic materials, strain engineering is often employed to change the lattice spacing and adjust the position of the d-band center. Huang et al. investigated the electrochemical performance of CO₂RR with octahedral and icosahedral Pd catalysts. Experimental results demonstrated that the maximum FE of the Pd icosahedral/C catalyst was 91.1% at 0.8 V, which was 1.7 times higher than the maximum FE of the Pd octahedral/C catalyst at 0.7 V. Theoretical calculations showed that the Pd icosahedra have tensile strain relative to the Pd octahedra, leading to the dband center close to $E_{\rm F}$, which enhances the adsorption of the key intermediate *COOH on the metal surface, and consequently improves the catalytic activity.²²² Au NPs with compression-rich strain were synthesized via a liquid laser ablation strategy (denoted as Au-LAL) by Zhang et al. and were used for electrochemical CO₂RR. The experimental results indicated that the presence of compressive strain in Au-LAL resulted in higher current densities and FEs compared to plain Au NPs. *In situ* Raman characterization and theoretical calculations confirmed that the d-band center of the strained Au is changed, which increased the binding strength between the key intermediate *COOH and Au, and thus modulated the catalytic activity and selectivity of the Au-LAL catalyst. 223

SACs are one of the commonly used 2D catalysts. The strong interaction of CO on the FeN4 moiety limits CO desorption and therefore reduces the CO₂ to CO efficiency. The FE of CO₂RR can be significantly improved by constructing holes on the graphene substrate, because the introduction of hole edges decreases the d-band center of the active Fe atom site and weakens the Fe-C bond strength, which leads to a moderate *CO adsorption strength and promotes CO desorption. 224 Feng et al. designed and synthesized a nitrogen-doped carbon substrate with precisely controlled Fe-Cu di-atom sites at the atomic level and characterized its catalytic performance for CO2RR (Fig. 10f). Experiments demonstrated that Fe/Cu-N-C has higher current density (Fig. 10g), excellent FE, and high turnover frequency, which was attributed to the synergistic interaction between Fe and Cu that enables fast charge transfer, optimizes the position of the d-band center (Fig. 10h), and lowers the energy barriers for *COOH formation and *CO desorption.221

Briefly, the d-band center stands as the most widely used descriptor due to its quantitative interpretation of the interaction between the adsorbate and the catalyst surface. In recent years, significant advancements have been made to enhance the d-band center concept, aiming to gain a better understanding of the unique properties of the catalyst surface and the adsorbates involved in catalytic reactions. In future applications of the d-band center theory, a comprehensive approach incorporating the specific adsorbed atoms or molecules, along with the attributes of the active sites (top, bridge, or hollow), will be crucial in precisely predicting the activity of catalysts.

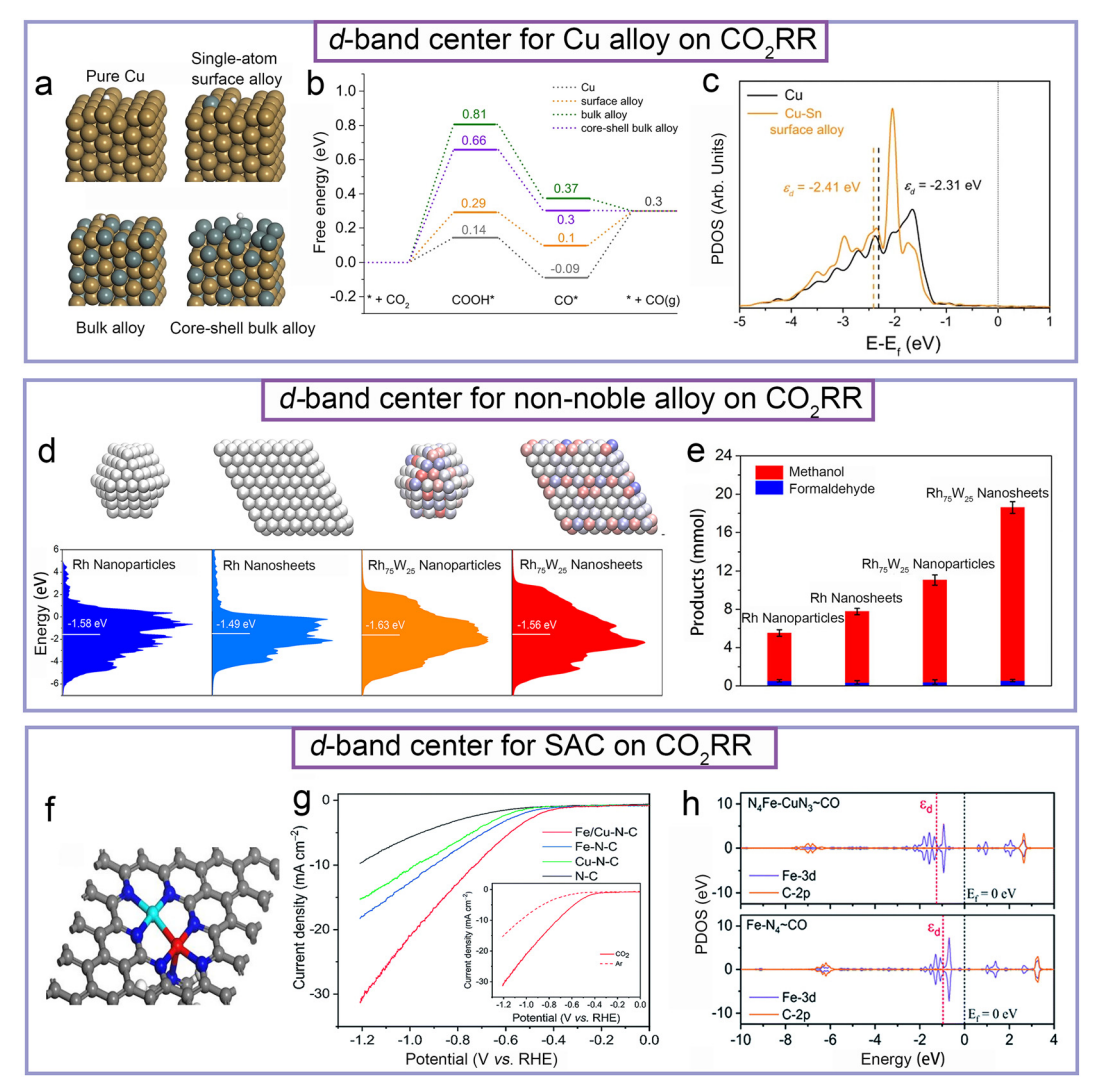


Fig. 10 (a) The structures of pure Cu and its alloys. (b) The free energy diagram of the CO₂RR pathway. (c) The d-band center of Cu and Cu-Sn alloys. Reproduced with permission. Copyright 2021, Nature. 219 (d) The d-band centers of Rh NP, Rh NS, Rh₇₃W₂₇ NP, and Rh₇₅W₂₅ NS catalysts. (e) Their corresponding products for CO₂RR. Reproduced with permission. Copyright 2017, American Chemical Society. ²²⁰ (f) The optimized structure of N₄Fe− CuN₃. (g) The linear sweep voltammetry profiles of Fe/Cu-N-C catalysts in a CO₂-saturated 0.1 M KHCO₃ electrolyte. (h) PDOS and d-band center of Fe on $N_4Fe-CuN_3$ and FeN_4 . Reproduced with permission. Copyright 2021, The Royal Society of Chemistry. ²²¹

3.6. How the d-band center guides the experiments

The d-band center is the most classical and powerful tool for describing the adsorption and desorption of reaction intermediates, enabling the optimization of catalytic activity by modulating the d-band center of the catalyst. For example, using DFT calculations, Sun et al. predicted that Fe doping into Ni₂P could enhance the non-uniform charge distribution within the material, leading to increased density of states at the $E_{\rm F}$ level, and consequently elevating the d-band center energy level of Ni₂P toward $E_{\rm F}$. According to the d-band center theory, this elevated dband center energy level can augment the adsorption capability of the material with OER intermediates, thus enhancing the OER activity of Ni₂P. Based on the theoretical guidance, the corresponding catalyst they synthesized requires only 166 mV to reach a current density of 10 mA cm⁻².²²⁵ In summary, the guidance of the d-band center for experiments can be approached through

the following steps: (i) calculate the d-band center of the active sites using theoretical or experimental techniques; (ii) determine whether the low catalytic activity results from excessive or insufficient adsorption; and (iii) modify the adsorption energy of the key intermediates to improve the catalytic activity by doping, alloying, strain engineering, or constructing heterojunctions, based on the desired adsorption strength.

4. Readily accessible intrinsic properties as descriptors

Although the d-band center theory has successfully described the interaction between catalysts and reaction intermediates, the substantial economic costs associated with obtaining the d-band center through theoretical calculations or experimental

measurements have prompted a growing interest in exploring readily accessible intrinsic properties as descriptors. These intrinsic properties are characteristics of catalysts that can be derived from existing databases without the need for extensive calculations or measurements, thus reducing costs significantly and are commonly referred to as inexpensive features. Examples of such readily accessible intrinsic properties include electronegativity, the number of outermost d electrons, ionization energy, coordination number of the active site, distance to the nearest neighboring atoms, etc. These properties can be directly determined for the specific catalyst under investigation. Leveraging these easily accessible properties as activity descriptors enables the accurate prediction of catalytic activity while minimizing costs, offering significant implications for the advancement of electrocatalysis.

4.1. Several readily accessible intrinsic properties

- 4.1.1. Electronegativity. Electronegativity is a measure of the ability of an atom to attract electrons within a chemical compound. It is a relative scale and does not have specific units. The greater the electronegativity value of an element, the stronger its ability to attract shared electrons in a covalent bond.²²⁶ The most commonly used standard for quantifying electronegativity is the Pauling scale, which assigns electronegativity values to each element based on their chemical behavior and properties. According to the Pauling scale, elements with electronegativity values greater than 1.8 are typically considered nonmetallic, those less than 1.8 are generally considered metallic, and those around 1.8 exhibit mixed characteristics.
- **4.1.2.** Electron affinity energy. The electron affinity energy, also known as electron affinity potential, is the energy associated with the interaction between an atom/molecule and an electron. It specifically refers to the energy released when a gaseous atom in its ground state gains an electron to form a gaseous anion, reflecting how easy it is for an atom to accept an additional electron and become negatively charged. The magnitude of the electron affinity energy depends on the strength between the atomic nucleus and the incoming electron.²²⁷
- 4.1.3. Outermost d electron. For metal atoms, the outermost electron shell typically consists of the d and f orbitals, which play significant roles in determining the catalytic activity of the metal. On the other hand, the inner filled s or p orbital has little effect on the catalytic activity of the metal. In catalysis, we generally consider the contribution of the outermost d orbital, because this orbital is responsible for forming bonds and participating in chemical reactions. Whether for 3d, 4d, and 5d TMs, the number of outermost d electrons increases from left to right.
- 4.1.4. Coordination environment. The coordination environment of metal atoms influences the catalytic activity of a material. The arrangement of atoms surrounding the active site, known as the coordination sphere or first coordination layer, directly affects the binding strength of the active site and key intermediates involved in the catalysis. The coordination atom type, the distance between the coordination atom and the reaction site, and the coordination geometry all affect the binding strength of the active

site and the key intermediates, which in turn affects the catalytic activity of the material. The coordination number can serve as a straightforward descriptor for discerning trends in adsorption energy on pure metal surfaces. The correlation between coordination number and adsorption energy stems from the understanding that the vicinity surrounding a bulk metal atom is fully occupied, rendering it chemically inactive due to the spatial constrains. As the metal-metal bond breaks and the metal atom becomes increasingly exposed, its susceptibility to species adsorption rises. Therefore, the reduction in the coordination number of the metal atom suggests a stronger affinity for binding adsorbates. The comprehensive impact of coordination on adsorption energy can be effectively captured by the generalized coordination number of atom *i*, denoted as $\overline{\text{CN}}(i) = \sum_{j=1}^{n_i} \frac{cn(j)}{cn_{\text{max}}}$, where cn(j) represents the

coordination number of the first nearest neighbors and cn_{max} indicates the maximal coordination at the given site.228 This descriptor has proven successful in elucidating the adsorption of

4.2. Readily accessible intrinsic properties as descriptors for electrocatalytic reactions

various atomic species, including *C, *O, and *N.

Among the readily accessible intrinsic properties of catalysts, electronegativity is the most widely considered factor to bridge the readily accessible intrinsic properties and catalytic performance of the catalysts. In addition, considering the role of adsorbates and active sites from multiple perspectives can provide a deeper understanding of the catalytic activity of the catalyst. HER is one of the simplest electrocatalytic reactions, and it has been interpreted earlier that *H is the key intermediate in HER. Zhu et al. used p-block atom doped g-C₃N₄ models to explore the intrinsic origin of their HER activity. 229 By considering multiple readily accessible intrinsic factors, they found a volcano-shaped relationship between η_{HER} (or ΔG_{*H}) and the descriptor $\varphi = (n_d/n_N) \times (E_d/E_N) \times (E_b/E_N) \times (I_d/I_N)$ for the most stable D-g-C₃N₄. ²²⁹ In this descriptor, n, E, and I are the number of electrons occupying the outermost p-orbital (valence electrons of the p-orbital), the electronegativity, and the electronic affinity, respectively. The subscripts d, N, and b represent the dopant, nitrogen, and replaced/adsorption-site atom, respectively. Doping p-block elements into the framework of g-C₃N₄ can alter the interaction between the active sites and the intermediates, thereby significantly optimizing the catalytic behavior for HER. Furthermore, Zhao et al. investigated the effect of p-block element doping in graphene structures on the OER/ORR catalytic performance, and proposed a descriptor based on electronegativity and electron affinity energy to correlate the doping and catalytic activity. The descriptor, denoted as $\Phi = (E_X/E_C) \times (A_X/A_C)$, is a dimensionless factor. E_X , E_C and A_X , A_C are the electronegativity and electron affinity of the dopant (X) and C atoms. By utilizing this descriptor, a volcano relationship between Φ and the minimum η required for ORR/OER was obtained. It has been proved that the catalytic activities of p-block element-doped carbon nanomaterials can be further predicted using this Φ descriptor.230

In catalytic reactions, the active center, which comprises both active adsorption sites and their coordination environment, plays a significant role in determining the overall catalytic activity and selectivity. Therefore, a careful consideration must be exercised on the synergy between active sites and their coordination environment to achieve the desired catalytic performance.⁸⁵ Recently, a general design principle was proposed by Xu et al. to evaluate the activity of graphene-based SACs for ORR, OER, and HER, This design principle takes into account multiple internal factors, including coordination number, electronegativity of active sites and the nearest neighboring atoms, and the elemental periodic correlation coefficient. By studying single vacancy with three carbon atoms (SV-C₃), double vacancy with four carbon atoms (DV-C₄), four pyridine nitrogen atoms (pyridine-N₄), and four pyrrole nitrogen atoms (pyrrole-N₄) (Fig. 11a), they established a descriptor:

atoms (pyrrole-N₄) (Fig. 11a), they established a descriptor:
$$\phi'_{\rm OH/H} = \alpha_{\rm g}\theta_{\rm d} \times \frac{E_{\rm M} + \frac{1}{L-1} \times (n_{\rm N} \times E_{\rm N} + n_{\rm C} \times E_{\rm C})}{E_{\rm O/H}}, \quad \text{where} \quad \alpha$$

represents the correction coefficient, $E_{\rm M}$, $E_{\rm N}$, and $E_{\rm C}$ are the electronegativity of different atoms, and $n_{\rm N}$ and $n_{\rm C}$ are the number of nearest-neighbor N and C atoms. Interestingly, this descriptor showed a volcano relationship between $\eta_{\rm HER}$ and $U_{\rm OER}^{\rm onset}$ (Fig. 11b and c). Furthermore, the applicability of this descriptor can also be extended to macrocyclic molecules.²³¹ Furthermore, molybdenum disulfide (MoS₂), featuring unique electronic and optoelectronic properties, has attracted intensive attention. In particular, Moterminated edge sites of MoS2 have demonstrated remarkable catalytic activities comparable to that of Pt-based catalysts. However, there is still a lack of uniform descriptors to avoid the dependence on traditional trial-and-error methods in catalyst design. Ran et al. proposed a universal descriptor based on the theoretical study of HER on various MoS2 structures such as TM-substitute, S-vacancy, Mo-edge, and S-edge. The descriptor exhibited a linear relationship with ΔG_{*H} , which can be defined

as
$$\Psi = \text{NBNB}_{\text{Mo-S}} \times \text{NV}_{\text{Mo-S}} \times \frac{X_{\text{Mo-S}}}{X_{\text{S-H}}} + \text{NB}_{\text{TM-S}} \times \text{NV}_{\text{TM-S}} \times \frac{X_{\text{TM-S}}}{X_{\text{S-H}}} \times R_{\text{TM-S}}$$
, in which NB_{TM-S} is the number of TM-S bonds.

Readily accessible intrinsic properties as descriptor on OER and HER

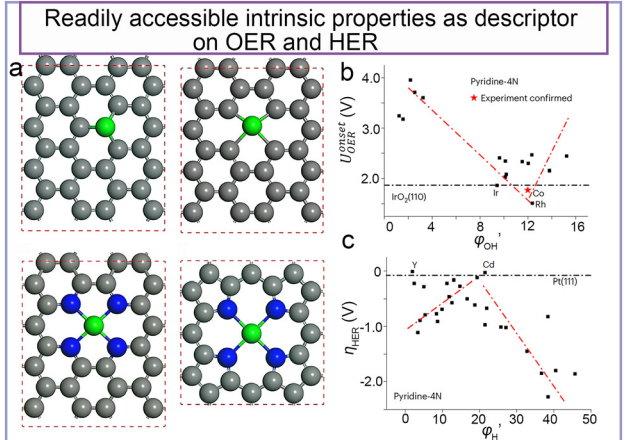


Fig. 11 (a) Four geometric configurations of graphene-based SACs. (b) $U_{\text{OER}}^{\text{onset}}$ and (c) η_{HER} of graphene-based SACs as a function of the descriptor φ' . Reproduced with permission. Copyright 2024, Springer Nature.²³¹

 X_{A-B} is defined as $\sqrt{\frac{X_A}{NC_A}\frac{X_B}{NC_B}}$, where X_A and NC_A are the electronegativity and the corresponding coordination number of atom A. NV_{TM-S} is the covalent electron number of the TM-S bond. R_{TM} is defined as $\frac{r_{\mathrm{TM}}+r_{\mathrm{s}}}{r_{\mathrm{Mo}}+r_{\mathrm{s}}}$. The results highlighted the significance of bond properties within the coordination microenvironment for catalytic reactions. More interestingly, a similar volcano curve between the descriptor and ΔG_{*H} can be found in the WS₂ system with different defects.232

The electronegativity and the number of valence electrons can also be utilized to describe the catalytic NRR activities. For example, Guo et al. studied the single TM decorated defective MoS_2 for NRR. ²³³ They discovered that the catalytic NRR activity was limited by the hydrogenation of the second N atom and the desorption of the second NH3 molecule. These processes appear to be affected by the strong interaction between N and the decorated metal atom. By introducing the descriptor, the correlation between ΔE_{*N} and the readily accessible intrinsic property of the active site is established. The descriptor is denoted as $\varphi = \theta_d \times E_M$, where E_M and θ_d are the electronegativity and the number of valence electrons respectively for the embedded TM atom. The greater value of φ corresponds to the weaker bonding of N to the active site.

Recently, 2D transition metal borides, known as MBenes (boron analogues of MXenes), have emerged as a new kind of promising catalyst due to their large specific surface area and high density of active sites. Yao et al. evaluated the NRR performance of TMs in Mo vacancies of the MBene nanosheet (Mo₂B₂O₂). They identified the first hydrogenation of N₂ as the PDS and highlighted *NNH as the key intermediate. Furthermore, they proposed a binary descriptor based on the number of d electrons and the period of the doped metal atom to establish a connection between the readily accessible intrinsic properties and catalytic activities of the catalyst. 234 Among the various metal catalysts for NRR, Au is often regarded as the best choice due to its high catalytic performance for NRR and low activity for competitive HER. 235,236 In order to further improve the activity of the Au catalyst and explore its nature in NRR, Zheng et al. screened a series of Au-based single-atom alloys and proposed three descriptors, including key intermediates and readily accessible intrinsic properties of the doped metal. They identified the reaction step $*N_2 \rightarrow *NNH$ as the PDS because the triple bond in N₂ is relatively inert. Interestingly, they observed a volcano relationship between $\Delta G(*N_2-*NNH)$ and the readily accessible intrinsic descriptor $\varphi = \frac{d}{\sqrt{E_{\mathrm{m}}}}$, where d and E_{m} represent the number of d electrons and electronegativity of the doped metal atom (Fig. 12a and b). Based on the volcano relationship, the Mo-

and W-doped Au(111), located at the peak of the volcano curve, was identified as the best catalyst for NRR.237 Likewise, the descriptor $\varphi = \frac{\mathrm{d}}{\sqrt{E_\mathrm{m}}}$ can also be used in single-atom-embedded

artificial holey SnN3 monolayers (Fig. 12c) for NRR, and a volcano relationship was found between $U_{\rm L}$ and φ (Fig. 12d).²³⁸ In addition, the first ion energy of the active center can also

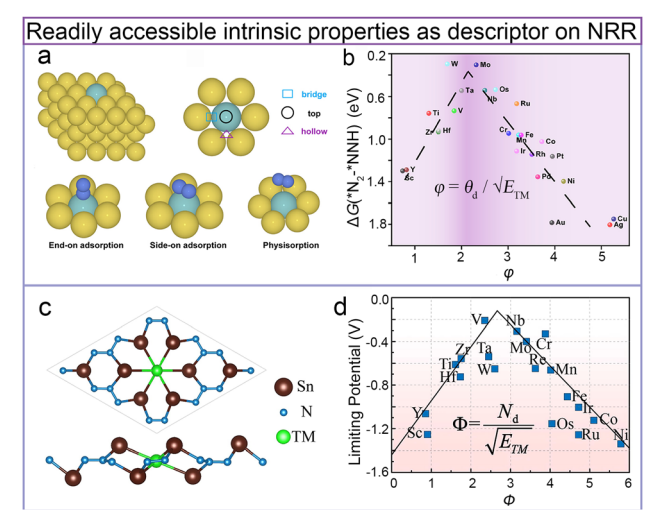


Fig. 12 (a) Models of M/Au(111) single-atom alloys. (b) A volcano relationship between $\Delta G(*N_2 \rightarrow *NNH)$ and the descriptor φ . Reproduced with permission. Copyright 2021, American Chemical Society. 237 (c) Top view and side view of TM/d-SnN3 with a single TM atom embedded in the central cavity. (d) Volcano plot for the U_1 of TM/d-SnN₃ as a function of the descriptor Φ . Reproduced with permission. Copyright 2022, Wiley-VCH.238

influence the bonding strength between active sites and the absorbates due to the electron transfer during the interaction process. Recently, Ouyang et al. demonstrated that boroncontaining co-doped graphene showed improved catalytic activity for NRR compared to carbon-based catalysts. Based on the calculations, ΔG_{*NNH} has a linear correlation with ΔG_{max} . In order to reveal the intrinsic characteristics of these doped structures, the researchers proposed a descriptor defined as $\Phi = (E_X/E_X)$ $(E_{\rm B}) \times I_{\rm X}^{-1}/I_{\rm B}^{-1}$, where E and I are the electronegativity and the first ion energy of the atom, respectively. X and B are the doped element and the boron atom, respectively. The study highlighted that the intrinsic difference between doped elements and the carbon atom has a significant impact on the electron transfer and bonding strength of the intermediates, which ultimately influences the catalytic activity of the catalyst in NRR.³⁹

Electrocatalytic reduction of nitrate (NO₃⁻) or NO to NH₃ (NO₃RR) has attracted intensive attention in recent years. This process offers the advantages of simultaneous elimination of harmful substances and production of valuable products. 239-241 In order to address the lack of information on the underlying catalytic mechanism and the impact of readily accessible intrinsic factors on NO₃RR, Wang et al. systematically investigated the performance of NO₃RR/NORR on TMN₃ and TMN₄ materials and used the activity

$$\text{descriptor} \qquad \varphi = \theta_{\rm d} \times \frac{E_{\rm M} + \alpha \times (n_{\rm N} \times E_{\rm N} + n_{\rm N} \times E_{\rm C})}{E_{\rm O}}. \qquad \text{This}$$

descriptor aims to elucidate the relationship of readily accessible intrinsic properties of TM centers and their local environments with regard to the catalytic activities of NO₃RR. The adsorption of NO₃⁻ is linearly correlated with the activity descriptor for both TMN3 and TMN4 materials. Additionally, a volcano-type diagram was discovered between the descriptor and the U_L of NORR on TMN₃ and TMN₄ materials. More importantly, this descriptor also allows for the identification of other graphene-based SACs with excellent NO3RR activity. 242

The electrochemical CO2RR presents several challenges, including multiple electron transfer processes, complex reaction intermediates, and formation of multiple reaction products. These factors have posed significant limitations on developing efficient catalysts for CO2RR. To overcome this bottleneck and identify high-performance catalysts, it is essential to search for descriptors that can accurately predict the catalytic activity of catalysts. The descriptor used for CO2RR may include multi-type readily accessible intrinsic properties such as electronegativity, atom radius, and coordination microenvironment feature due to its complex reaction intermediates. For instance, Gong et al. have conducted a theoretical study on M-N-C (porphyrin)-contained SAC structures with 3d TMs for the CO₂RR (Fig. 13a), and revealed a volcano-shaped relationship between η required for CO formation and the bonding energy of the *CO intermediate (Fig. 13b). Further studies that focused on the readily accessible intrinsic properties of catalysts have demonstrated that the η^{CO} for CO_2RR can be described as a segmented function of the descriptor $\Phi = V_{\rm M} \times E_{\rm M}/r_{\rm M}$ depending on different reaction pathways, where $V_{\rm M}$, $E_{\rm M}$, and $r_{\rm M}$ represent the valence electron number, the electronegativity of metal atoms, and the radius of metal ions, respectively (Fig. 13c). In addition to the 3d TMs, the descriptor can also be extended to predict the catalytic behavior of CO₂RR for 4d and 5d TMs.²⁴³ Wang et al. improved the efficiency of CO₂ to CH₄ conversion by introducing axial O atoms in TM-coordinated nitrogen-doped carbon SAC species (M-N₄O-C) (Fig. 13d).²⁴⁴ For both M-N₄-C and M-N₄O-C, η can be expressed as a function of $\Delta G(*OH)$ and ΔG (*CHO), which are strongly correlated with the proposed

descriptor
$$\varphi = \frac{V_{\rm M} \left[X_{\rm M} \left(\prod\limits_{L=1}^N \frac{1}{d} X_{\rm L} \right) \right]^{1/(N+1)}}{X_{\rm C} + X_{\rm O}}$$
; the relationship dia-

gram of $\Delta G(*OH)$ and η on M-N₄O-C is shown in Fig. 13e. Here, $V_{\rm M}$ is the d-shell electron number of a metal atom; N is the coordination number of the central atom; $X_{\rm M}$, $X_{\rm L}$, $X_{\rm C}$, and $X_{\rm O}$ represent the electronegativity of the M atom, its nearest atom L, adsorbate C and O atoms connected by metal atoms, respectively; and d is the bond length between the central atom and the nearest neighbor atom. Finally, the volcano curve for η and φ is obtained (Fig. 13f). Correspondingly, the relationship between the descriptor and catalytic CO2RR activities is linked by the key intermediates in the CO₂RR reaction pathway.²⁴⁴

In CO₂RR, effective suppression of competitive HER and side products is of great importance to improve the efficiency of target products. Existing works on porous covalent organic frameworks (COF) showed an extremely low η (0.34 V) for the selective reduction of CO2 to CO, while preventing the formation of the unwanted by-products such as H₂ and HCOOH. In the mechanistic explanation of different catalytic activities on these

COF catalysts, a concise and clear descriptor
$$\Phi = \frac{N}{r_{\rm TM} \times n}$$
 was put forward. In this descriptor, N , $r_{\rm TM}$, and n represent the number of d electrons, atomic radius, and periodic number of TM, respectively. By using this descriptor, a volcano relationship

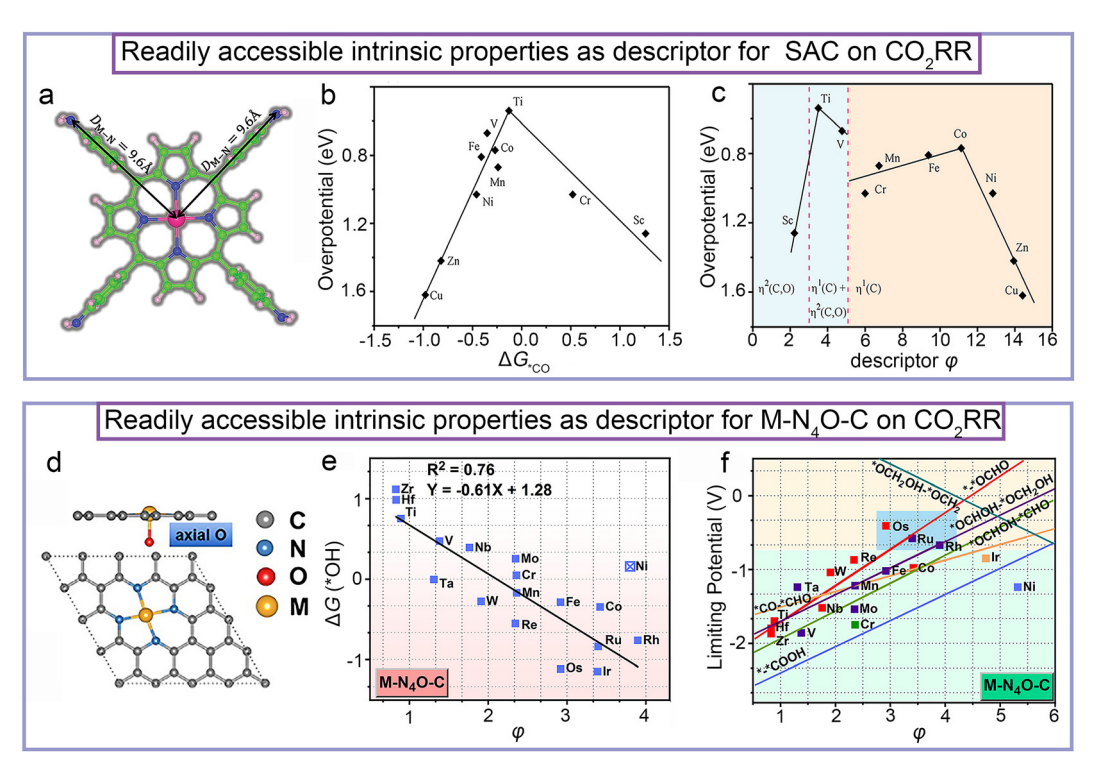


Fig. 13 (a) The top view of TM-based SACs. (b) The volcano curve between the overpotential and ΔG_{*CO} . (c) The volcano curve between the overpotential and the descriptor φ . Reproduced with permission. Copyright 2019, Wiley-VCH.²⁴³ (d) The side view and top view of the M-N₄O-C catalyst. (e) The linear relationship between $\Delta G(^*OH)$ and the descriptor φ . (f) The volcano relationship between U_L and the descriptor φ . Reproduced with permission. Copyright 2022, American Chemical Society.²⁴⁴

between $\eta^{\rm CO}$ and Φ was established. ²⁴⁵ Achieving a comprehensive understanding of the underlying mechanism and improving the selectivity of Cu catalysts for the CO2RR remain a challenging task. In this regard, Zhu et al. conducted a study employing grazing incidence X-ray diffraction and electron back-scattered diffraction techniques to track the top-surface reconstructions of Cu catalysts during CO2RR. Building upon their observations, they proposed three types of descriptors (crystal facet, atomic coordination number, and step-terrace angle) to establish an intrinsic structure-performance relationship. These descriptors provided valuable insight into the mechanism of CO₂RR and aid in the design of more efficient CO₂RR catalysts.²⁴⁶ In a recent DFT study, Gao et al. quantified the effect of the readily accessible intrinsic properties of adsorbates and substrates on their bonding behavior through step-bystep correction of descriptors. The studied adsorbates encompassed key intermediates involved in the reaction, while the chosen substrates included a diverse range of TMs, NPs, intermetallics, and oxides. Finally, the researcher innovatively developed a model for determining the adsorption energy (E_{ad}) using an electronic descriptor (Ψ). This relationship was expressed as

$$E_{\mathrm{ad}} = 0.1 \times \frac{X_{\mathrm{m}} - X}{X_{\mathrm{m}} + 1} \times \psi + 0.2 \times \left(\frac{X + 1}{X_{\mathrm{m}} + 1}\right) \times \overline{\mathrm{CN}} + \theta$$
. Here, E_{ad}

represents the adsorption energy of the intermediate, $X_{\rm m}$ denotes the maximum number of bonds that the central atom of a given adsorbate can form with the specific coordinating group, X represents the actual number of formed bonds, Ψ is related to the number of electrons and electronegativity, $\overline{\text{CN}}$

indicates the generalized coordination number of surfaces.²⁴⁷ and θ stands for a constant associated with each adsorbate. Importantly, this model covers a broad range of intermediates, as well as the physical and chemical properties of various materials, providing a long-sought guidance for future materials design.248

Using the readily accessible intrinsic nature of a catalyst as a descriptor for predicting its catalytic activity offers a cost-effective and practical approach that avoids the need for extensive DFT calculations and experimental tests. When considering readily accessible intrinsic properties, it is essential to meticulously examine certain physical and chemical properties, such as the atomic characteristics of the active site, the distance to the surrounding ligand atoms, and the variance in electronegativity. In addition, accurately assigning weights to each of these factors is a complex issue that requires in-depth study. This is due to the fact that different catalysts exhibit significantly varied influencing factors on catalytic activity, which are interrelated with both the catalyst itself and the adsorbate.

4.3. How the readily accessible intrinsic property descriptors guide the experiments

By consolidating the aforementioned inexpensive descriptors, we have ascertained that the electronegativity of the active atom and its surrounding ligand atoms, the number of ligands, and the number of d-electrons of the metal atoms collectively offer a comprehensive depiction of catalytic activity. For example, in a work on the synthesis of propylene over Pt-based catalysts,

Chang et al. introduced a descriptor $\Phi = \frac{r_{\rm M}}{r_{\rm Pt}} \Delta \chi \Delta d/n$, where rdenotes the atomic radius, $\Delta \chi$ represents the electronegativity difference, Δd signifies the distance between Pt and the nearest neighboring atom, and n indicates the number of electron shells of M. Through this descriptor, PtMn and PtZn were identified as exceptionally propylene-selective catalysts. Based on the prediction of the descriptor, they synthesized the PtMn catalyst and achieved propylene selectivity up to 90%. 249 In general, for a specific class of catalysts, one can effectively steer the activity trend by precisely defining these economic descriptors. This allows for the identification of the optimal catalyst for a given reaction based on the derived volcano diagram or linear relationship. Subsequently, one can synthesize the ideal catalyst experimentally for validation to achieve the goal of using theory to guide experiment.

5. Spin-related properties as the descriptor

In the past few decades, research in the field of electrocatalysis has predominantly focused on investigating the readily accessible intrinsic properties of catalysts, such as atomic species and electronegativity, as well as electronic properties like energy band structure and charge transfer. However, investigations regarding the exploration of spin-related magnetic features in electrocatalysis are scarce. These features encompass atomic magnetic moments and high/low spin states, which have received limited attention in electrocatalytic studies. For metal atoms in a certain material, high spin states are generally associated with larger magnetic moments, whereas low spin states correspond to smaller magnetic moments. The presence of different spin states can give rise to variations in adsorption behavior and bonding strength between catalysts and key intermediates, ultimately affecting the catalytic activity. The most classic moiety in SAC, FeN₄, was reported to exhibit various electron configurations, including low $(d_{xy}^2, d_{yz}^2, d_{xz}^1, d_{z^2}^1)$, intermediate $(d_{xy}^2, d_{yz}^1, d_{xz}^1, d_{z^2}^1)$, and high $(d_{xy}^{1}, d_{yz}^{1}, d_{xz}^{1}, d_{zz}^{1}, d_{z^{2}, d_{x^{2}-y^{2}}})$ spin states (Fig. 14a). 250,251 These different spin states can result in variations in selectivity and electron transfer during catalytic reactions due to the different electron occupation when interacting with molecules (Fig. 14a). In addition, there are differences in the adsorption of adsorbates between spin-polarized and non-spin-polarized systems for certain magnetic atoms (Cr, Mn, Fe, Co, Ni). Nørskov et al. have demonstrated that the commonly used exchange-correlation generalizations based on DFT show stronger adsorption energies on nonspin-polarized surfaces compared to spin-polarized ground-state surfaces for Fe, Co, and Ni surfaces.²⁵² In 2021, theoretical predictions have shown that the CO2RR catalytic activity of a novel TM-doped ferroelectric electrocatalyst, TM@α-In₂Se₃, can be influenced by the ferroelectric polarization. The calculations revealed two effects of ferroelectric polarization: adjusting the confining potential by tuning the d-band center, and modifying the reaction paths and final products on Nb@In₂Se₃ and Re@In₂Se₃. These changes in properties arise from the synergistic effects of the

d-orbitals (d-orbital centers) of the adsorbed metal atoms, polarization-dependent electron transfer, and CO2 adsorption energy under ferroelectric switching.²⁵³ In recent years, the impact of spin-related factors on electrochemical reactions has gained increasing attention in the field of electrocatalysis.

5.1. Spin-related properties as the descriptor on OER/ORR

The OER has been extensively studied in the context of magnetic materials. This is primarily due to the fact that O₂ is a paramagnetic molecule with a three-linear state in the ground state, whereas H₂O is a single-linear antimagnetic molecule, resulting in slow kinetics.²⁵⁶ Some spin-polarized ferromagnetic materials, such as CoFe₂O₄, ²⁵⁷ have been proved to be effective catalysts for promoting OER. Introducing non-metal doping into the catalyst can induce charge/spin polarization, thereby enhancing the activity of the reaction. Zhang et al. conducted research on carbon nanoflakes (NCFs) and doped two classical N-configurations, pyridine-N and graphite-N, into them, resulting in significantly improved ORR activity comparable to that of Pt in alkaline medium. Both experiments and theoretical calculations demonstrated that the dipole formed by edge-type pyridine-N/graphite-N and the spacing of the edge carbon atoms played a synergistic role in facilitating the reaction.²⁵⁸ Furthermore, sulfur doped Fe₁-NC SACs have also demonstrated impressive ORR performance. ⁵⁷Fe Mössbauer spectroscopy and electron paramagnetic resonance spectroscopy have provided evidence indicating that the introduction of S atoms induces a shift in the spin state of the active site. Specifically, the optimal active site for ORR was identified as the low-spin single Fe³⁺-atom within the C-FeN₄-S moiety. Building upon this finding, the researchers proposed the OER mechanism as depicted in Fig. 14b. Additionally, DFT calculations revealed that the presence of low-spin doped Fe weakened the adsorption of the key intermediate *OH, thereby enhancing the ORR activity (Fig. 14c and d).257

In 2021, Yang et al. rationally designed and synthesized an atomically dispersed bimetallic Fe, Mn/N-C catalyst for ORR. They aimed to modulate the catalytic activity of the Fe-N structure by altering the spin state of the Fe atoms. Through measurements of zero-field cooling temperature-dependent magnetization, they found that the Fe^{III} ions in the intermediate spin state of the FeN₄/C system, with a single electron configuration $(t_{2g}^{4}e_{g}^{1})$, were preferentially involved in OER. This allowed for the occupation of the antibonding π -orbital of oxygen, resulting in high catalytic activity of the designed Fe, Mn/N-C catalyst. 259 Li et al. demonstrated that strain engineering can modify the spin states of the active site, thus impacting the catalytic activity of catalysts. By applying a 9% strain to CoOOH, they were able to effectively adjust the electronic arrangement of Co atoms from a low-spin configuration $(t_{2g}^6 e_g^0)$ to a high-spin configuration $(t_{2g}^4 e_g^2)$. This adjustment significantly reduced the energy (from 1.35 to 0.03 eV) required for releasing O2 from adsorbed intermediates during the OER. 260

5.2. Spin-related properties as the descriptor on NRR

The N₂ molecule is commonly known as a diamagnetic molecule, which implies that it has zero net magnetic moment.

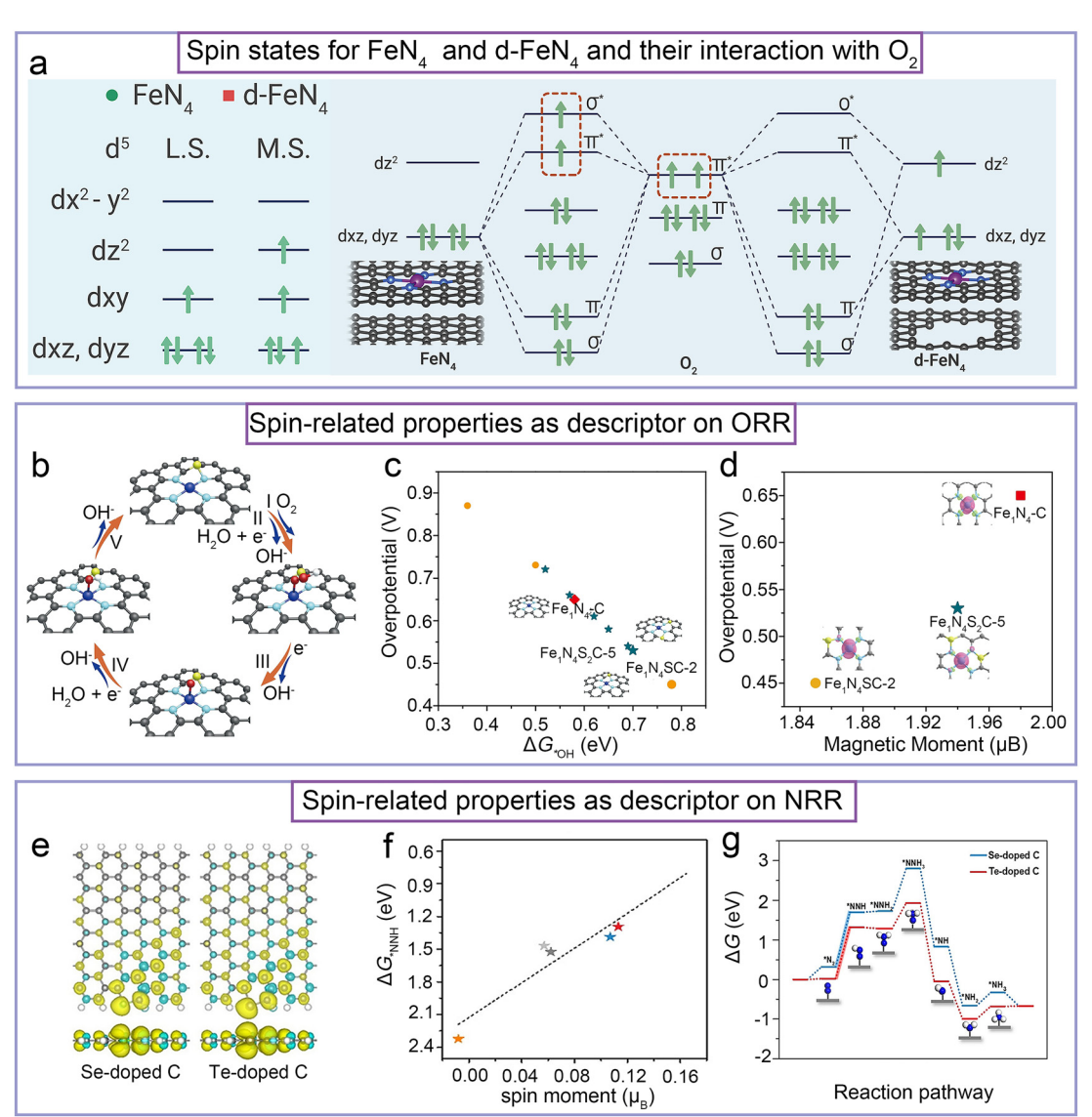


Fig. 14 (a) Magnetic susceptibility of d-FeN₄ or FeN₄ and their orbital interactions with O₂. Reproduced with permission. Copyright 2022, ScienceDirect. 251 (b) The proposed ORR mechanism for the Fe₁-N₄SC catalyst. (c) and (d) The overpotential as a function of (c) ΔG_{*OH} and (d) magnetic moment for the considered catalysts. Reproduced with permission. Copyright 2021, Wiley-VCH.²⁵⁴ (e) The structures of Se- and Te-doped C catalysts. (f) The correlation between ΔG_{*NNH} and the spin moment of the active C atom. (g) Free-energy diagrams of NRR on Se- and Te-doped C catalysts. Reproduced with permission. Copyright 2020, Wiley-VCH. 255

Consequently, the spin polarization has limited impact on N₂ adsorption. However, recent studies have revealed that different spin states can influence the activation of N≡N to different extents. For instance, in the case of Rh NPs, the combination of high spin polarization and charge exchange between the Rh NPs and substrates has been found to synergistically enhance N2 adsorption and activation.261 The donation and back-donation mechanism has long been recognized as an effective explanation for N₂ activation. In 2021, Wang et al. investigated the spin regulation of the neighboring FeN4 moiety by MoN4. Their findings demonstrated that the presence of neighboring MoN₄ can induce a shift in the spin state of the Fe center from a highspin configuration $(d_{xy}^2, d_{yz}^1, d_{xz}^1, d_{z^2}^1, d_{z^2y^2}^1)$ to a medium-spin configuration $(d_{xy}^2, d_{yz}^2, d_{xz}^1, d_{zz}^{-1})$. Based on the N₂ activation

mechanism mentioned earlier, the redistribution of d electrons ensures their efficient overlapping with the N 2p orbitals, thereby facilitating the activation of the $N \equiv N$ triple bond. Experimental measurement of the NH₃ yield rate and FE further supported these predications, confirming the improved NRR activity resulting from the spin regulation.²⁶² Recently, considerable attention has been given to the NRR involving Mn³⁺-Mn³⁺ pairs and Mn⁴⁺-O-Mn⁴⁺ pairs, along with the underlying mechanisms. The distinct electron distributions within these pairs can significantly influence their adsorption behavior with NRR intermediates, ultimately influencing the overall NRR performance. Experimental studies have demonstrated that the MnO₂ catalyst, featuring Mn³⁺-Mn³⁺ pairs, exhibited a noteworthy NH₃ yield of 147.2 µg h⁻¹ with a FE of 15% at

-0.75 V, which is attributed to the exceptional spin properties of Mn³⁺-Mn³⁺ pairs.²⁶³

Numerous studies have emphasized the significance of the first protonation step (resulting in the formation of *NNH) as the decisive PDS in the NRR. In 2020, Qiao et al. conducted an extensive computational investigation on carbon materials doped with oxygen-group elements (O, S, Se, Te) as potential catalysts for NRR (Fig. 14e). They highlighted the significant influence of spin polarization on the adsorption of the *NNH intermediate and identified a linear relationship between the adsorption energy of *NNH (ΔG_{*NHH}) and the magnetic moment (Fig. 14f). Through comprehensive mechanistic studies, they demonstrated that the heteroatom doping-induced charge accumulation enhanced the adsorption of N2 on carbon atoms. Moreover, the heteroatom doping-induced spin polarization promoted the formation of *NNH through the first protonation step, reducing the energy barrier associated with the decisive velocity step and enabling more efficient NRR. The final results indicated that the Se-doped carbon catalyst exhibited favorable electronic and spin properties, enhancing the adsorption and activation of N2, thus displaying high intrinsic NRR activity (Fig. 14g).²⁵⁵ In 2021, Zhang et al. conducted further research on Co-doped LaNiO3 (denoted as Co-LNO) with a focus on investigating the relationship between the effective spin magnetic moment of the catalyst and its catalytic performance in NRR. The study demonstrated that LaNi_{0.995} Co_{0.005}O with a 3d high-spin configuration exhibited remarkable NRR performance. Specifically, it achieved a high NH₃ yield of 14.57 mg h⁻¹ mg⁻¹, an outstanding FE of 26.44%, and a remarkable energy efficiency of 21.35% (at 0.1 V vs. RHE). Further investigation into the mechanism revealed that Co-LNO provided additional catalytically active sites comprising Co and accompanying oxygen vacancies. These sites played a crucial role in modulating the electronic structure of LNO, promoting N₂ adsorption, and facilitating the first protonation step during the NRR process.264

Cao et al. summarized a vast amount of experimental data on NH3 synthesis and demonstrated two crucial factors that impact the catalytic activity of the NRR, providing a new pathway for the development of advanced catalysts for NH3 synthesis. The first factor identified is the electrostatic interaction between the adsorbed promoter and the N-N dissociative transition state. The second factor is the magnetic catalyst promoter effect, which involves the manipulation of the spin properties of the catalyst, resulting in a decrease in the activation energy for NRR.265 Building upon this research, Guo et al. proposed a strategy to modulate the NRR activity of magnetic catalysts by regulating their spin magnetic moments. Through DFT calculations, they observed significant changes in the magnetic moments of Fe atoms based on the coordination environment of neighboring N atoms. Notably, the magnetic moment of Fe atoms exhibited a linear correlation with both the applied potential U versus SHE and the adsorption energy of N atoms. By controlling the magnetic moments of Fe atoms, it becomes possible to adjust the adsorption strength of intermediates, fine-tuning the catalytic activity, and ultimately lowering the U_L of NRR.²⁶⁶ In a recent

study, Huang et al. employed B-doped carbon dots to modulate the electron spin density of the magnetic Co₃O₄ catalyst, resulting in an exceptional FE for production of $\mathrm{NH_4}^+$ (94.6 \pm 0.9%). The change of spin configuration from $t_{2g}^{6}e_{g}^{0}$ of Co^{3+} to $t_{2g}^{5}e_{g}^{2}$ of Co^{2+} was identified as a key factor in enhancing the electrocatalytic NO₃RR. Experimental results and theoretical calculations further supported that the modulation of spin-density affected the PDS, reducing the energy barrier that needed to be overcome, and ultimately optimizing the catalytic activity.267

The spin arrangement and magnetic moment of the magnetic atom within the active site of a catalyst have been demonstrated to exert a significant influence on the binding strength with crucial intermediates, and consequently impact its catalytic activity in specific reactions. Altering the type or quantity of ligand atoms surrounding the magnetic atom at the active site can modulate its electron arrangement, leading to changes in the occupancy of various orbitals. In studies related to spin-catalysis, emphasis is placed on acquiring the orbital distribution and electron occupation of the central atoms, which can be correlated with the adsorption of key intermediates to predict the catalytic activity.

5.3. How the spin-related descriptors guide the experiments

Recent studies have demonstrated that the catalytic activity of magnetic materials can be manipulated by adjusting the magnetic field, highlighting the significance of the material's spin properties. The magnetic moment of the catalyst with Bader charge transfer can be determined through DFT calculations; the orbital arrangement and electron occupation of the central atom in the catalyst can be obtained according to the crystal field theory. Typically, the high and low spin states of the central atom in catalysts are pivotal in affecting the adsorption strength of reaction intermediates, which, in turn, impact the overall catalytic activity. Comparing the spin states of the active central atoms allows for the assessment of the adsorption strength of various catalysts with reaction intermediates, enabling the prediction of the catalytic performance. From an experimental perspective, crafting target catalysts based on predicted catalytic activity not only conserves resources but also streamlines the development of catalysts tailored for specific applications.

6. Multiple features as descriptors

Traditionally, the catalytic activity of a given catalyst can be influenced by a variety of factors, making it a significant challenge to accurately describe or predict its activity. Additionally, it is difficult to determine the precise impact of different characteristics on catalytic activity solely relying on experimental results or DFT calculations. The development of the machine learning (ML) strategy has significantly enhanced the efficiency and accuracy in identifying the factors affecting catalytic activity. Several research papers and reviews have underscored that ML methods enable the rapid identification of various features that influence the catalytic performance of catalysts, thereby facilitating the acquisition of precise descriptors. 42,268-270

In general, the process of using ML methods (Fig. 15a)²⁷¹ to identify the parameters affecting the catalytic activity and the extent of each parameter entails the following steps: (i) data preparation: this involves acquiring the essential multidimensional features from the database, including readily accessible intrinsic properties of catalysts, spin properties, d-band centers, and other relevant factors. Additionally, the inclusion of experimental or DFT results is essential as part of the training data. (ii) Model selection: the optimal ML model is selected by comparing the output results and mean absolute error (MAE) of different models to ensure the most suitable model for the specific application. Generally, a smaller MAE indicates a more accurate ML model. (iii) Descriptor determination: this involves utilizing the selected ML model to assess the impact of various input parameters on catalytic activity, thereby identifying the most significant descriptors. It is important to include as many input parameters as possible to ensure a more precise search for descriptors, as the catalytic performance of a catalyst is generally determined by multiple factors. (iv) Catalyst prediction: this step is performed using the recognized factors and the identified descriptors from the ML model to enable the screening of known catalysts or the design of new catalysts with improved performance.

Taking HER as an example, Fung et al. utilized *H as a key intermediate to assess the catalytic effectiveness of single-atom N-doped graphene catalysts. By employing the compressed sensing method, SISSO (Sure Independence Screening and Sparsifying Operator), they determined a multidimensional descriptor $\Delta G_{\rm H} = -1.032 \times \frac{\varepsilon_{\rm d}}{q} + 13.424 \times \frac{1}{r_{\rm cov}} + 1.726 \times (\varepsilon_{\rm d} \times {\rm EN}) - 0.045 \times \frac{1}{r_{\rm cov}}$ $(d_{\rm occ}^2)$ – 9.241. In this descriptor, the intrinsic properties such as electronegativity (EN) and covalent radius (r_{cov}), d-state center $(\varepsilon_{\rm d})$, Bader charge (q), and the number of occupied d-states $(d_{\rm occ})$ for spin-related properties are all included to collectively evaluate the catalytic activity.²⁷⁵ For the g-CN structure, it has been documented that certain anchored metal atoms (such as Sc, Ti, V. Ga. Sn. and Au) on large holes can serve as excellent catalysts for HER, 276 while the strong *H adsorption energy by other metals still poses challenges for the release of *H. A recently reported new class of hybrid double atom catalysts (HDACs), featuring both metal and non-metal atoms embedded in the holes of the g-CN structure, effectively mitigate this issue by altering the geometric and electronic properties between the active site atoms. Through the application of ML, it has been demonstrated that the hydride formation enthalpy (H_{xf}) , the

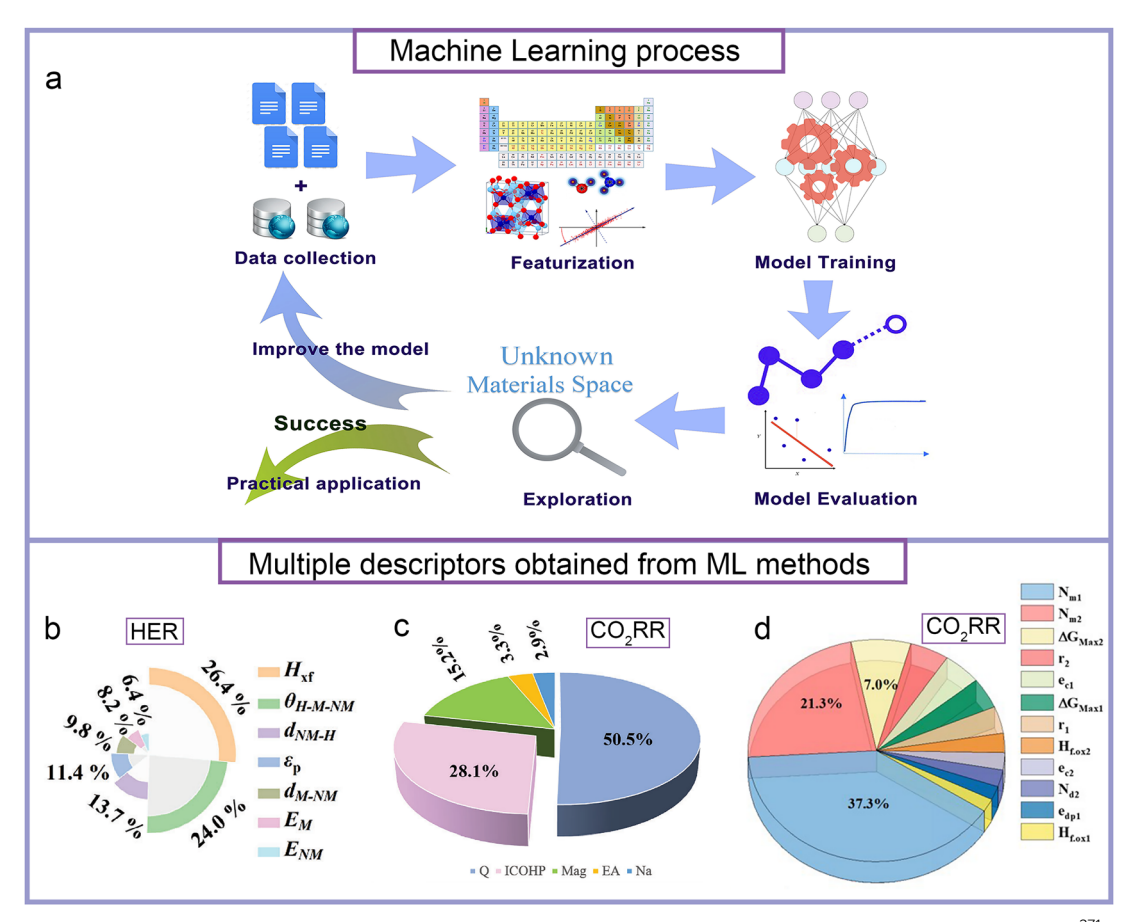


Fig. 15 (a) Workflow of machine learning methods. Reproduced with permission. Copyright 2022, American Chemical Society.²⁷¹ (b) The feature importance calculated by random forest regression methods for $\Delta G_{^*H}$, Copyright 2023, Wiley-VCH. 272 (c) The feature importance analysis in the random forest model for CO_2RR on graphdiyne and holey graphyne-based SACs. Reproduced with permission. Copyright 2023, Wiley-VCH. 273 (d) The feature importance of the most important 12 features got by ML methods. Reproduced with permission. Copyright 2021, American Chemical Society.²⁷⁴

bond angle between H atoms and catalyst surface atoms (θ_{M-H-NM}) , the distance between H atoms and active center atoms $(d_{M/NM-H})$, and the p-band center of non-metal atoms (ε_p) all play crucial roles in determining the catalytic activity of these HDACs for HER (Fig. 15b). In addition, a catalytic activity map of HDACs has been established, providing a predictive framework to accurately forecast the activity of HDACs in unexplored chemical spaces.²⁷² In a recent development, Abraham et al. integrated ML strategies with DFT calculations to screen 2D MXene-based catalysts with exceptional HER catalytic activity. They established nine distinct ML models and employed random forest regression (RFR) and gradient boosting regression (GBR) to reduce the number of features through recursive feature elimination. Ultimately, they identified the valence electron number (V_T) and electron affinity (EA_T) of the termination group, along with the dband center relative to the mean variance (d_{bcs}²), as predictive descriptors to correlate $\Delta G_{^*\mathrm{H}}$. 269

In the context of multi-electron reaction processes, such as CO₂RR, identifying the primary factors influencing the catalytic activity of specific catalysts is particularly challenging. Ren et al. designed graphdiyne and holey graphyne-based single atom catalysts and identified *CO2 and *OH as crucial intermediates in CO2RR. By leveraging a ML model, they successfully pinpointed the intrinsic properties, including the polarization charge (Q) of the central metal, the interaction between the central metal and the carrier (ICOHP), and relevant magnetic properties such as the magnetic moment of the central metal atom, as the key descriptors (Fig. 15c). Furthermore, they quantified the relative influence of these descriptors on catalytic performance. Interestingly, this ML model can also be applied to quickly predict other candidate materials for CO₂RR.²⁷³ Another study focuses on dual-metal-site catalysts (DMSCs) for CO₂RR, where dual-TM atoms are supported on a phthalocyanine (Pc) ring. This study demonstrated that the gradient boosting regression (GBR) model proved to be the most effective method for predicting the $U_{\rm L}$ of CO₂RR for 249 Pc DMSCs. Moreover, the model successfully identified Ag-MoPc and Ag-CoPc as superior catalysts for CO₂RR. In the quest to uncover the origin of catalytic activity in these catalysts, *COOH was identified as a key intermediate in the reaction. This study also unveiled that the electronegativity of the active atoms of the catalyst, along with the charge transfer (Q) from the TM atom to the Pc ring, all play pivotal roles in determining the catalytic activity of the catalyst (Fig. 15d).²⁷⁴ Furthermore, due to significant constrains on the kinetics of the CO₂RR process and the successful industrial-level conversion of CO₂ into CO, catalytic CORR has become a focal point of research. In a DFT calculation study on CORR using single TM atom anchored nitrogen-doped γ-graphene (N-GY) as the catalyst, it was found that the position of metal atoms in the periodic table of elements influences the final product. Specifically, metal atoms in the front and middle positions of the periodic table favor the production of CH₄, while TMs are conducive to methanol production. In addition, five key characteristics—Pauli electronegativity (N_e) , first ionization energy $(I_{\rm m})$, atomic radius $(R_{\rm m})$, d orbital, and atomic number $(Z_{\rm m})$ of the TM atom—are utilized as input data to correlate $\Delta E_{\rm CHO}^*$

through ML methods, with Z_m identified as the predominant descriptor.277

7. Summary and outlook

The rational design and development of electrocatalysts with exceptional electrocatalytic activity, high FE, specific product selectivity, low cost, eco-friendliness, and long-term stability have become significant goals in this field. To aid in this endeavor, the establishment and development of descriptors have played crucial roles in facilitating the exploration of the catalytic mechanisms of electrocatalysts and promoting the design of electrocatalysts. In this review, we discuss the mechanisms of widely studied electrocatalytic reactions and summarize the relationships of intrinsic property descriptors, d-band center descriptors, and spin-dependent descriptors with key intermediates of catalytic reactions. Descriptors have rapidly evolved in recent years and have been widely used to interpret differences in catalytic properties and guide the design of electrocatalysts. However, the search for suitable descriptors remains a major challenge. Developing descriptors that are sensible, readily accessible, and capable of capturing the multidimensional nature of catalytic activity still requires extensive efforts, especially in the following aspects:

7.1. Combining multiple factors as descriptors

In general, replacing a ligand (coordination atom) around a metal atom with a more electronegative atom can induce changes in the electron occupation of the d-electron layer of the metal atoms, and alter the binding strength between the adsorbed molecules and the metal atoms. It is important to note that this adsorption behavior is not solely determined by the electronegativity of the coordinating atom, but also influenced by the specific arrangement of d-electrons in the active center. Nørskov et al. discussed the applicability of the d-band center concept in studying the adsorption of N atoms on 3d TMs ranging from V to Cu. For the Cu metal, the value of ε_d is too low, resulting in a completely filled bonding and nearly filled antibonding states between the adsorbed N atom and the d states. As a result, all d states and antibonding states are well below $E_{\rm F}$. Consequently, the dependence on the d-band center disappears. On the other hand, for early TMs like V with higher values of ε_d , the energy of the d states is relatively high. This leads to a gradual decrease in the occupancy of the antibonding adsorbate/d states as ε_d increases. Consequently, the dependence on ε_d gradually diminishes.²⁵² Therefore, when studying the electronic structure of active sites with fully occupied or few occupied d-bands, it is essential to take into account other factors such as spin states, bond lengths, ligands, etc., in addition to the d-band center. Furthermore, there has been a growing interest in assessing the catalytic behavior of catalysts by considering multiple factors simultaneously. Researchers have attempted to establish linear relationships between multiple factors and the catalytic performance of catalysts. However, little discussions have been involved on delving into the readily accessible intrinsic physical or chemical

mechanisms underlying these factors. Therefore, the search for more integrated descriptors that combine the properties of different dimensions to jointly describe catalytic activity remains a great challenge in this field.

7.2. Developing advanced methods to seek for precise descriptors

The introduction of artificial intelligence (AI) has made a significant impact across various sectors including the economy, healthcare, and transport. Additionally, AI is also increasingly dominating the fields of economic forecasting, biomedicine, chemical synthesis, and physical mechanisms. Specifically, in the realm of computational catalysis, both ML and data mining have proven to be useful tools, offering numerous benefits including significantly reducing computational time and providing a deeper understanding of the activity and selectivity. ML algorithms, such as GBR, support vector regression, RFR, and kneighbor regression, and neural networks have been extensively utilized in the field of computational catalysis. These algorithms play a crucial role in the design of screening conditions for the selection of electrocatalysts, enabling researchers to obtain desired catalysts more efficiently. Moreover, ML models trained using the existing DFT calculations can predict the binding energies for new catalyst structures, allowing for more efficient assessment of the strength of the bonding between intermediates and the catalyst surface. In the establishment of descriptors for studying catalytic activity, numerous existing works have considered a wide range of factors that can be directly obtained from databases, such as period, group, electronegativity, atomic number, figure of merit, ionization energy, etc. Following the collection of these features, ML techniques can be applied to analyze the impact of these different factors on catalytic activity. Through this analysis, researchers can identify the optimal descriptors that significantly influence the catalytic performance.

Despite the significant advances in ML, the training of reliable ML models requires large amounts of high-quality data as input. However, the cost of collecting such data, whether through computational simulations or experimental work, can be prohibitively expensive. As a result, there is an urgent need to develop more efficient methods that can reduce resource waste and maximize data utility. Wang's group has developed an innovative approach that combines automatic DFT calculations with an improved reinforcement learning algorithm, especially the Monte Carlo Tree Search with Policy Gradient (MCTS-PG) algorithm. This integration has enabled the rapid identification of materials with desired properties starting from minimal initial data, thereby reducing the need for extensive DFT calculations. By utilizing this approach, they successfully screened seven reliable catalysts (CuAl₃, SbCaCu, ZrInCu₂, Si₂CaCu₂, AlV₆Ga, CAlTi₂, and ZrInCu₂) for CO₂ activation and methanation through 200 MCTS-PG steps. 278 In summary, ML plays a pivotal role in (i) efficiently screening and selecting eligible catalysts based on their readily accessible intrinsic properties; (ii) predicting crucial properties that connect activities such as adsorption energy; and (iii) determining key descriptors that influence the catalytic performance. These capabilities greatly

facilitate the design and optimization of catalysts, contributing to the development of more effective catalysts for diverse chemical processes.

7.3. Improving the scope of application of descriptors

Existing works on descriptors often focus on specific systems or reactions, and there is a need to explore the universal descriptors that can be applied to a wide range of catalysts and electrochemical reactions. Specifically, a comprehensive descriptor should incorporate multiple physicochemical factors to accurately describe the catalytic activity for a given material. This could involve considering the interactions between the catalyst and key intermediates of the electrocatalytic reactions, such as HER, OER, ORR, NRR, and CO₂RR. For example, fitting adsorption energies of key intermediates such as *H, *OH, *N and *CO from the d-band center theory has been successful for some catalysts. However, it is important to recognize that not all the active sites conform to the d-band center theory, and corrections may be necessary. This can involve taking into account the surrounding coordination environment and incorporating additional factors like bond lengths, planar spacing, etc. These approaches aim to create descriptors that are applicable to a broad range of intermediates. In conclusion, developing comprehensive descriptors is still an ongoing and urgent pursuit in the field of electrocatalysis. The complexity and diversity of catalysts and electrochemical reactions pose challenges in finding universally applicable descriptors. Further exploration and research are needed to advance the development of comprehensive descriptors that can be widely applied across diverse catalysts and electrochemical applications.

Conflicts of interest

The authors declare that they have no known competing financial interests or personal relationships that could have appeared to influence the work reported in this paper.

Acknowledgements

The authors acknowledge the funding supports from the National Natural Science Foundation of China (Grant No. 52202264), the Natural Science Foundation of Shandong Province (2022HWYQ-005), Youth Taishan Scholar Program of Shandong Province (tsqn202306025), and the Program of Qilu Young Scholars of Shandong University.

References

- 1 J. A. Turner, Science, 1999, 285, 687-689.
- 2 S. Chu and A. Majumdar, Nature, 2012, 488, 294-303.
- 3 D. Larcher and J. M. Tarascon, Nat. Chem., 2015, 7, 19-29.
- 4 W. Sheng, Z. Zhuang, B. Xu and Y. Yan, Sci. Adv., 2016, 2, e1501602.
- 5 Q. Zhou, C. Xu, J. Hou, W. Ma, T. Jian, S. Yan and H. Liu, Nano-Micro Lett., 2023, 15, 95.

Chem Soc Rev

- 6 B. Y. Tang, R. P. Bisbey, K. M. Lodaya, W. L. Toh and Y. Surendranath, Nat. Catal., 2023, 6, 339-350.
- 7 Y. Yang, Y. Qian, Z. Luo, H. Li, L. Chen, X. Cao, S. Wei, B. Zhou, Z. Zhang, S. Chen, W. Yan, J. Dong, L. Song, W. Zhang, R. Feng, J. Zhou, K. Du, X. Li, X. M. Zhang and X. Fan, Nat. Commun., 2022, 13, 7225.
- 8 S. Sultan, M. Ha, D. Y. Kim, J. N. Tiwari, C. W. Myung, A. Meena, T. J. Shin, K. H. Chae and K. S. Kim, Nat. Commun., 2019, 10, 5195.
- 9 W. H. Lee, Y. J. Ko, J. H. Kim, C. H. Choi, K. H. Chae, H. Kim, Y. J. Hwang, B. K. Min, P. Strasser and H. S. Oh, Nat. Commun., 2021, 12, 4271.
- 10 D. Galyamin, J. Torrero, I. Rodriguez, M. J. Kolb, P. Ferrer, L. Pascual, M. A. Salam, D. Gianolio, V. Celorrio, M. Mokhtar, D. Garcia Sanchez, A. S. Gago, K. A. Friedrich, M. A. Pena, J. A. Alonso, F. Calle-Vallejo, M. Retuerto and S. Rojas, Nat. Commun., 2023, 14, 2010.
- 11 H. Li, S. Kelly, D. Guevarra, Z. Wang, Y. Wang, J. A. Haber, M. Anand, G. T. K. K. Gunasooriya, C. S. Abraham, S. Vijay, J. M. Gregoire and J. K. Nørskov, *Nat. Catal.*, 2021, 4, 463–468.
- 12 J. Li, H.-M. Yin, X.-B. Li, E. Okunishi, Y.-L. Shen, J. He, Z.-K. Tang, W.-X. Wang, E. Yücelen, C. Li, Y. Gong, L. Gu, S. Miao, L.-M. Liu, J. Luo and Y. Ding, Nat. Energy, 2017, 2, 17111.
- 13 M. Luo, Z. Zhao, Y. Zhang, Y. Sun, Y. Xing, F. Lv, Y. Yang, X. Zhang, S. Hwang, Y. Qin, J. Y. Ma, F. Lin, D. Su, G. Lu and S. Guo, Nature, 2019, 574, 81-85.
- 14 Q. Zhang and J. Guan, Energy Environ. Mater., 2020, 4, 307-335.
- 15 P. P. Lopes, D. Y. Chung, X. Rui, H. Zheng, H. He, P. Farinazzo, B. D. Martins, D. Strmenik, V. R. Stamenkovic, P. Zapol, J. F. Mitchell, R. F. Klie and N. M. Markovic, J. Am. Chem. Soc., 2021, 143, 2741-2750.
- 16 J. Guan, X. Bai and T. Tang, Nano Res., 2021, 15, 818-837. 17 V. Smil, Nature, 1999, 400, 415.
- 18 J. W. Erisman, M. A. Sutton, J. Galloway, Z. Klimont and W. Winiwarter, Nat. Geosci., 2008, 1, 636-639.
- 19 J. G. Chen, R. M. Crooks, L. C. Seefeldt, K. L. Bren, R. M. Bullock, M. Y. Darensbourg, P. L. Holland, B. Hoffman, M. J. Janik, A. K. Jones, M. G. Kanatzidis, P. King, K. M. Lancaster, S. V. Lymar, P. Pfromm, W. F. Schneider and R. R. Schrock, Science, 2018, 360, 873.
- 20 K. Chu, Y. Luo, P. Shen, X. Li, Q. Li and Y. Guo, Adv. Energy Mater., 2022, 12, 2103022.
- 21 X. W. Lv, X. L. Liu, Y. J. Suo, Y. P. Liu and Z. Y. Yuan, ACS Nano, 2021, 15, 12109-12118.
- 22 X. Wu, M. Nazemi, S. Gupta, A. Chismar, K. Hong, H. Jacobs, W. Zhang, K. Rigby, T. Hedtke, Q. Wang, E. Stavitski, M. S. Wong, C. Muhich and J. H. Kim, ACS Catal., 2023, 13, 6804-6812.
- 23 B. Han, J. Liu, C. Lee, C. Lv and Q. Yan, Small Methods, 2023, 7, 2300277.
- 24 M. Ferri, L. Delafontaine, S. Guo, T. Asset, P. Cristiani, S. Campisi, A. Gervasini and P. Atanassov, ACS Energy Lett., 2022, 7, 2304-2310.
- 25 S. Yu, S. Louisia and P. Yang, *JACS Au*, 2022, 2, 562–572.

- 26 J. Yu, J. Wang, Y. Ma, J. Zhou, Y. Wang, P. Lu, J. Yin, R. Ye, Z. Zhu and Z. Fan, Adv. Funct. Mater., 2021, 31, 2102151.
- 27 S. Ringe, Nat. Commun., 2023, 14, 2598.
- 28 H. S. Taylor, Proc. R. Soc. London, Ser. A, 1925, 108, 745.
- 29 A. J. Medford, A. Vojvodic, J. S. Hummelshøj, J. Voss, F. Abild-Pedersen, F. Studt, T. Bligaard, A. Nilsson and J. K. Nørskov, J. Catal., 2015, 328, 36-42.
- 30 C. J. H. Jacobsen, S. Dahl, B. S. Clausen, S. Bahn, A. Logadottir and J. K. Nørskov, J. Am. Chem. Soc., 2001, 123, 8404-8405.
- 31 K. S. Exner, ChemCatChem, 2019, 11, 3234-3241.
- 32 K. S. Exner, Angew. Chem., Int. Ed., 2020, 59, 10236-10240.
- 33 W. Ding, Z. Wei, S. Chen, X. Qi, T. Yang, J. Hu, D. Wang, L. J. Wan, S. F. Alvi and L. Li, Angew. Chem., Int. Ed., 2013, 52, 11755-11759.
- 34 K. Guo, X. Han, S. Wei, J. Bao, Y. Lin, Y. Li and D. Xu, Nano Lett., 2023, 23, 1085-1092.
- 35 Q. Yu, W. Yu, Y. Wang, J. He, Y. Chen, H. Yuan, R. Liu, J. Wang, S. Liu, J. Yu, H. Liu and W. Zhou, Small, 2023, 19, 2208045.
- 36 X. Rong, H. J. Wang, X. L. Lu, R. Si and T. B. Lu, Angew. Chem., Int. Ed., 2020, 59, 1961-1965.
- 37 W. Lin, Y.-R. Lu, W. Peng, M. Luo, T.-S. Chan and Y. Tan, J. Mater. Chem. A, 2022, 10, 9878-9885.
- 38 L. Zhang, C. Y. Lin, D. Zhang, L. Gong, Y. Zhu, Z. Zhao, Q. Xu, H. Li and Z. Xia, Adv. Mater., 2019, 31, e1805252.
- 39 W. Ouyang, Q. Zhi, L. Gong, H. Sun, M. Liu, J. Zhang, X. Han, Z. Xia and L. Zhang, J. Mater. Chem. A, 2021, 9, 24590-24599.
- 40 Y. Zang, Q. Wu, S. Wang, B. Huang, Y. Dai and Y. Ma, J. Phys. Chem. Lett., 2022, 13, 527-535.
- 41 X. Wang, X. J. Gao, L. Qin, C. Wang, L. Song, Y. N. Zhou, G. Zhu, W. Cao, S. Lin, L. Zhou, K. Wang, H. Zhang, Z. Jin, P. Wang, X. Gao and H. Wei, Nat. Commun., 2019, 10, 704.
- 42 J. Liu, W. Luo, L. Wang, J. Zhang, X. Z. Fu and J. L. Luo, Adv. Funct. Mater., 2022, 32, 2110748.
- 43 J. Liu, H. Liu, H. Chen, X. Du, B. Zhang, Z. Hong, S. Sun and W. Wang, Adv. Sci., 2020, 7, 1901614.
- 44 H. J. Peng, M. T. Tang, J. Halldin Stenlid, X. Liu and F. Abild-Pedersen, Nat. Commun., 2022, 13, 1399.
- 45 S. Hammes-Schiffer and G. Galli, Nat. Energy, 2021, 6, 700–705.
- 46 C. Baeumer, J. Li, Q. Lu, A. Y. Liang, L. Jin, H. P. Martins, T. Duchon, M. Gloss, S. M. Gericke, M. A. Wohlgemuth, M. Giesen, E. E. Penn, R. Dittmann, F. Gunkel, R. Waser, M. Bajdich, S. Nemsak, J. T. Mefford and W. C. Chueh, Nat. Mater., 2021, 20, 674-682.
- 47 S. Feng Zai, Y. Han Wu, Y. Tong Zhou, Z. Tian Hui Li and C. Bin Guo, J. Colloid Interface Sci., 2023, 643, 350-359.
- 48 X. Sun, H. Zhang, S. Wang, Z. Ren, B. Huang, Y. Dai and W. Wei, J. Phys. Chem. C, 2022, 126, 16606-16614.
- 49 Z. Ren, S. Wang, H. Zhang, B. Huang, Y. Dai and W. Wei, Phys. Chem. Chem. Phys., 2021, 23, 25239-25245.
- 50 F. Abild-Pedersen, J. Greeley, F. Studt, J. Rossmeisl, T. R. Munter, P. G. Moses, E. Skulason, T. Bligaard and J. K. Nørskov, Phys. Rev. Lett., 2007, 99, 016105.
- 51 F. Calle-Vallejo, D. Loffreda, M. T. Koper and P. Sautet, Nat. Chem., 2015, 7, 403-410.

- 52 Z.-F. Huang, J. Song, S. Dou, X. Li, J. Wang and X. Wang, Matter, 2019, 1, 1494-1518.
- 53 J. H. Montoya, C. Tsai, A. Vojvodic and J. K. Nørskov, ChemSusChem, 2015, 8, 2180-2186.
- 54 H. Wang, T. Zhai, Y. Wu, T. Zhou, B. Zhou, C. Shang and Z. Guo, Adv. Sci., 2023, 10, 2301706.
- 55 J. Wang, S. Xu, C. Zhang, A. Yin, M. Sun, H. Yang, C. Hu and H. Liu, InfoMat, 2023, 5, e12376.
- 56 S. Wang, W. Wei, X. Lv, B. Huang and Y. Dai, J. Mater. Chem. A, 2020, 8, 1378-1385.
- 57 R. Chattot, P. Bordet, I. Martens, J. Drnec, L. Dubau and F. Maillard, ACS Catal., 2020, 10, 9046-9056.
- 58 E. C. dos Santos, R. B. Araujo, M. Valter, G. Salazar-Alvarez, M. Johnsson, M. Bajdich, F. Abild-Pedersen and L. G. M. Pettersson, Electrochim. Acta, 2021, 398, 139283.
- 59 R. B. Araujo, I. Bayrak Pehlivan and T. Edvinsson, Nano Energy, 2023, 105, 108027.
- 60 X. Yu, R. B. Araujo, Z. Qiu, E. Campos dos Santos, A. Anil, A. Cornell, L. G. M. Pettersson and M. Johnsson, Adv. Energy Mater., 2022, 12, 2103750.
- 61 M. Tamtaji, Q. Peng, T. Liu, X. Zhao, Z. Xu, P. R. Galligan, M. D. Hossain, Z. Liu, H. Wong, H. Liu, K. Amine, Y. Zhu, W. A. Goddard Iii, W. Wu and Z. Luo, Nano Energy, 2023, **108**, 108218.
- 62 N. Helsel and P. Choudhury, Mol. Catal., 2023, 545, 113213.
- 63 M. Andersen and K. Reuter, Acc. Chem. Res., 2021, 54, 2741-2749.
- 64 S. Jiao, X. Fu and H. Huang, Adv. Funct. Mater., 2021, 32, 2107651.
- 65 J. Song, C. Wei, Z. F. Huang, C. Liu, L. Zeng, X. Wang and Z. J. Xu, Chem. Soc. Rev., 2020, 49, 2196-2214.
- 66 G. Bharath, C. Liu, F. Banat, A. Kumar, A. Hai, A. Kumar Nadda, V. Kumar Gupta, M. Abu Haija and J. Balamurugan, Chem. Eng. J., 2023, 465, 143040.
- 67 L. Yang, J. Fan, B. Xiao and W. Zhu, Chem. Eng. J., 2023, 468, 143823.
- 68 Q. Xue, X. Qi, K. Li, Y. Zeng, F. Xu, K. Zhang, T. Yang, X. Qi and J. Jiang, Catalysts, 2023, 13, 722.
- 69 Y. Xiao and C. Shen, Small, 2021, 17, e2100776.
- 70 J. Greeley, Annu. Rev. Chem. Biomol. Eng., 2016, 7, 605-635.
- 71 Z.-J. Zhao, S. Liu, S. Zha, D. Cheng, F. Studt, G. Henkelman and J. Gong, Nat. Rev. Mater., 2019, 4, 792-804.
- 72 B. M. Tackett, W. Sheng and J. G. Chen, Joule, 2017, 1, 253-263.
- 73 J. Zhu, L. Hu, P. Zhao, L. Y. S. Lee and K. Y. Wong, Chem. Rev., 2020, 120, 851-918.
- 74 Q. Gao, W. Zhang, Z. Shi, L. Yang and Y. Tang, Adv. Mater., 2019, 31, e1802880.
- 75 Q. Tang and D.-e Jiang, ACS Catal., 2016, 6, 4953-4961.
- 76 Y. Yu, J. Zhou and Z. Sun, Adv. Funct. Mater., 2020, 30, 2000570.
- 77 Y. Zheng, Y. Jiao, Y. Zhu, L. H. Li, Y. Han, Y. Chen, A. Du, M. Jaroniec and S. Z. Qiao, *Nat. Commun.*, 2014, 5, 3783.
- 78 Q. Zhang, Z. Jiang, B. M. Tackett, S. R. Denny, B. Tian, X. Chen, B. Wang and J. G. Chen, ACS Catal., 2019, 9, 2415-2422.

- 79 P. Lindgren, G. Kastlunger and A. A. Peterson, ACS Catal., 2019, 10, 121-128.
- 80 X. Bai, Q. Wang, G. Xu, Y. Ning, K. Huang, F. He, Z. J. Wu and J. Zhang, Chemistry, 2017, 23, 16862-16870.
- 81 X. Li, P. Cui, W. Zhong, J. Li, X. Wang, Z. Wang and J. Jiang, Chem. Commun., 2016, 52, 13233-13236.
- 82 J. Wan, C. Wang, Q. Tang, X. Gu and M. He, RSC Adv., 2019, 9, 37467-37473.
- 83 M. Gorlin, J. H. Stenlid, S. Koroidov, H. Y. Wang, M. Borner, M. Shipilin, A. Kalinko, V. Murzin, O. V. Safonova, M. Nachtegaal, A. Uheida, J. Dutta, M. Bauer, A. Nilsson and O. Diaz-Morales, Nat. Commun., 2020, 11, 6181.
- 84 S. Xu, M. Wang, G. Saranya, N. Chen, L. Zhang, Y. He, L. Wu, Y. Gong, Z. Yao, G. Wang, Z. Wang, S. Zhao, H. Tang, M. Chen and H. Gou, Appl. Catal., B, 2020, 268, 118385.
- 85 H. Xu, D. Cheng, D. Cao and X. C. Zeng, Nat. Catal., 2018, 1, 339-348.
- 86 J. Rossmeisl, Z. W. Qu, H. Zhu, G. J. Kroes and J. K. Nørskov, J. Electroanal. Chem., 2007, 607, 83-89.
- 87 A. Kulkarni, S. Siahrostami, A. Patel and J. K. Nørskov, Chem. Rev., 2018, 118, 2302-2312.
- 88 D. Kan, D. Wang, X. Zhang, R. Lian, J. Xu, G. Chen and Y. Wei, J. Mater. Chem. A, 2020, 8, 3097-3108.
- 89 I. C. Man, H. Y. Su, F. Calle-Vallejo, H. A. Hansen, J. I. Martínez, N. G. Inoglu, J. Kitchin, T. F. Jaramillo, J. K. Nørskov and J. Rossmeisl, ChemCatChem, 2011, 3, 1159-1165.
- 90 J. K. Nørskov, J. Rossmeisl, A. Logadottir and L. Lindqvist, J. Phys. Chem. B, 2004, 108, 17886-17892.
- 91 A. Vojvodic and J. K. Nørskov, Natl. Sci. Rev., 2015, 2, 140-143.
- 92 Z. Lu, G. Xu, C. He, T. Wang, L. Yang, Z. Yang and D. Ma, Carbon, 2015, 84, 500-508.
- 93 M. D. Bhatt, G. Lee and J. S. Lee, Electrochim. Acta, 2017, 228, 619-627.
- 94 M. Reda, H. A. Hansen and T. Vegge, ACS Catal., 2018, 8, 10521-10529.
- 95 R. Koitz, J. K. Norskov and F. Studt, Phys. Chem. Chem. Phys., 2015, 17, 12722-12727.
- 96 S. Kattel and G. Wang, J. Phys. Chem. Lett., 2014, 5, 452-456.
- 97 E. Jung, H. Shin, B. H. Lee, V. Efremov, S. Lee, H. S. Lee, J. Kim, W. Hooch Antink, S. Park, K. S. Lee, S. P. Cho, J. S. Yoo, Y. E. Sung and T. Hyeon, Nat. Mater., 2020, 19, 436-442.
- 98 A. M. Dudzinski, E. Diesen, H. H. Heenen, V. J. Bukas and K. Reuter, ACS Catal., 2023, 13, 12074-12081.
- 99 S. B. Patil and D. Y. Wang, Small, 2020, 16, e2002885.
- 100 Y. Wan, J. Xu and R. Lv, Mater. Today, 2019, 27, 69-90.
- 101 J. Zhao and Z. Chen, J. Am. Chem. Soc., 2017, 139, 12480-12487.
- 102 Z. Xue, X. Zhang, J. Qin and R. Liu, Nano Energy, 2021, 80, 105527.
- 103 X. Lv, W. Wei, B. Huang, Y. Dai and T. Frauenheim, Nano Lett., 2021, 21, 1871-1878.
- 104 B. He, P. Lv, D. Wu, X. Li, R. Zhu, K. Chu, D. Ma and Y. Jia, J. Mater. Chem. A, 2022, 10, 18690-18700.

- 105 Y. Zang, Q. Wu, S. Wang, B. Huang, Y. Dai and Y. Ma, *Phys. Rev. Appl.*, 2023, **19**, 024003.
- 106 P. Lv, D. Wu, B. He, X. Li, R. Zhu, G. Tang, Z. Lu, D. Ma and Y. Jia, *J. Mater. Chem. A*, 2022, **10**, 9707–9716.
- 107 Y. Xiao, C. Shen and W. B. Zhang, *Mater. Today Chem.*, 2022, 25, 100958.
- 108 Q. Wu, B. Huang, Y. Dai, T. Heine and Y. Ma, *npj 2D Mater. Appl.*, 2022, **6**, 52.
- 109 S. Back and Y. Jung, ACS Energy Lett., 2017, 2, 969-975.
- 110 S. Payra, S. Shenoy, C. Chakraborty, K. Tarafder and S. Roy, *ACS Appl. Mater. Interfaces*, 2020, **12**, 19402–19414.
- 111 X. Lv, J. Liu, T. Shao, M. Ye and S. Liu, *Catal. Today*, 2023, 420, 114188.
- 112 M. Li, N. Song, W. Luo, J. Chen, W. Jiang and J. Yang, *Adv. Sci.*, 2023, **10**, e2204579.
- 113 M. Jouny, W. Luc and F. Jiao, Nat. Catal., 2018, 1, 748-755.
- 114 X. Liao, R. Lu, L. Xia, Q. Liu, H. Wang, K. Zhao, Z. Wang and Y. Zhao, *Energy Environ. Mater.*, 2021, 5, 157–185.
- 115 W. Luc, X. Fu, J. Shi, J.-J. Lv, M. Jouny, B. H. Ko, Y. Xu, Q. Tu, X. Hu, J. Wu, Q. Yue, Y. Liu, F. Jiao and Y. Kang, *Nat. Catal.*, 2019, 2, 423–430.
- 116 L. Li, X. Li, Y. Sun and Y. Xie, *Chem. Soc. Rev.*, 2022, **51**, 1234–1252.
- 117 T. Kim, A. Kargar, Y. Luo, R. Mohammed, E. Martinez-Loran, A. Ganapathi, P. Shah and D. P. Fenning, *ACS Appl. Energy Mater.*, 2018, 1, 1965–1972.
- 118 K. P. Kuhl, E. R. Cave, D. N. Abram and T. F. Jaramillo, *Energy Environ. Sci.*, 2012, **5**, 7050.
- 119 C. Genovese, C. Ampelli, S. Perathoner and G. Centi, *Green Chem.*, 2017, **19**, 2406–2415.
- 120 S. Sen, D. Liu and G. T. R. Palmore, ACS Catal., 2014, 4, 3091–3095.
- 121 K. Jiang, R. B. Sandberg, A. J. Akey, X. Liu, D. C. Bell, J. K. Nørskov, K. Chan and H. Wang, *Nat. Catal.*, 2018, 1, 111–119.
- 122 J. Feng, L. Wu, S. Liu, L. Xu, X. Song, L. Zhang, Q. Zhu, X. Kang, X. Sun and B. Han, J. Am. Chem. Soc., 2023, 145, 9857–9866.
- 123 S. Vijay, W. Ju, S. Brückner, S.-C. Tsang, P. Strasser and K. Chan, *Nat. Catal.*, 2021, **4**, 1024–1031.
- 124 J.-H. Liu, L.-M. Yang and E. Ganz, *ACS Sustainable Chem. Eng.*, 2018, **6**, 15494–15502.
- 125 S. Liu, Z. Li, C. Wang, W. Tao, M. Huang, M. Zuo, Y. Yang, K. Yang, L. Zhang, S. Chen, P. Xu and Q. Chen, *Nat. Commun.*, 2020, 11, 938.
- 126 W. Ma, S. Xie, B. Zhang, X. He, X. Liu, B. Mei, F. Sun, Z. Jiang, L. Lin, Q. Zhang, B. Ren, G. Fu, X. Hu and Y. Wang, *Chem*, 2023, 9, 2161–2177.
- 127 J. Qu, X. Cao, L. Gao, J. Li, L. Li, Y. Xie, Y. Zhao, J. Zhang, M. Wu and H. Liu, *Nano-Micro Lett.*, 2023, 15, 178.
- 128 X. Wang, Y. Chen, F. Li, R. K. Miao, J. E. Huang, Z. Zhao, X. Y. Li, R. Dorakhan, S. Chu, J. Wu, S. Zheng, W. Ni, D. Kim, S. Park, Y. Liang, A. Ozden, P. Ou, Y. Hou, D. Sinton and E. H. Sargent, *Nat. Commun.*, 2024, 15, 616.
- 129 M. Luo and M. T. M. Koper, Nat. Catal., 2022, 5, 615-623.
- 130 J. K. Nørskov, J. Rossmeisl, A. Logadottir, L. Lindqvist, T. Bligaard and H. Jónsson, *J. Phys. Chem. B*, 2004, **108**, 17886–17892.

- 131 V. Tripković, E. Skúlason, S. Siahrostami, J. K. Nørskov and J. Rossmeisl, *Electrochim. Acta*, 2010, **55**, 7975–7981.
- 132 D. Zhang, Z. Wang, F. Liu, P. Yi, L. Peng, Y. Chen, L. Wei and H. Li, *J. Am. Chem. Soc.*, 2024, **146**, 3210–3219.
- 133 B. Hammer and J. K. Nørskov, Nature, 1995, 376, 238-240.
- 134 J. K. Nørskov, F. Abild-Pedersen, F. Studt and T. Bligaard, Proc. Natl. Acad. Sci. U. S. A., 2011, 108, 937–943.
- 135 A. Vojvodic, J. K. Nørskov and F. Abild-Pedersen, *Top. Catal.*, 2013, 57, 25–32.
- 136 H. Xin, A. Vojvodic, J. Voss, J. K. Nørskov and F. Abild-Pedersen, *Phys. Rev. B: Condens. Matter Mater. Phys.*, 2014, **89**, 115114.
- 137 Z. Chen, Y. Song, J. Cai, X. Zheng, D. Han, Y. Wu, Y. Zang, S. Niu, Y. Liu, J. Zhu, X. Liu and G. Wang, *Angew. Chem.*, *Int. Ed.*, 2018, 57, 5076–5080.
- 138 Y. Wang, J. Fu, H. Hu and D. Ho, ACS Appl. Mater. Interfaces, 2023, 15, 40846-40854.
- 139 P. G. Moses, B. Hinnemann, J. Bonde, K. P. Jørgensen, J. H. Nielsen, S. Horch, I. B. Chorkendorff and J. K. Nørskov, J. Am. Chem. Soc., 2005, 127, 5308–5309.
- 140 N. Du, C. Wang, X. Wang, Y. Lin, J. Jiang and Y. Xiong, Adv. Mater., 2016, 28, 2077–2084.
- 141 G. Zhan, Y. Yao, F. Quan, H. Gu, X. Liu and L. Zhang, J. Energy Chem., 2022, 72, 203-209.
- 142 C. Miao, Y. Zang, H. Wang, X. Zhuang, N. Han, Y. Yin, Y. Ma, M. Chen, Y. Dai, S. Yip, J. C. Ho and Z. X. Yang, *Adv. Mater. Interfaces*, 2022, **9**, 2200739.
- 143 C. Wei, Y. Sun, G. G. Scherer, A. C. Fisher, M. Sherburne, J. W. Ager and Z. J. Xu, *J. Am. Chem. Soc.*, 2020, 142, 7765–7775.
- 144 J. Wang, S. Xin, Y. Xiao, Z. Zhang, Z. Li, W. Zhang, C. Li, R. Bao, J. Peng, J. Yi and S. Chou, *Angew. Chem., Int. Ed.*, 2022, 61, e202202518.
- 145 J. K. Pedersen, T. A. A. Batchelor, A. Bagger and J. Rossmeisl, ACS Catal., 2020, 10, 2169–2176.
- 146 T. A. A. Batchelor, J. K. Pedersen, S. H. Winther, I. E. Castelli, K. W. Jacobsen and J. Rossmeisl, *Joule*, 2019, 3, 834–845.
- 147 M. C. Folgueras, Y. Jiang, J. Jin and P. Yang, *Nature*, 2023, 621, 282–288.
- 148 L. Wang, J. Ding, S. Chen, K. Jin, Q. Zhang, J. Cui, B. Wang, B. Chen, T. Li, Y. Ren, S. Zheng, K. Ming, W. Lu, J. Hou, G. Sha, J. Liang, L. Wang, Y. Xue and E. Ma, *Nat. Mater.*, 2023, 22, 950–957.
- 149 G. Cao, J. Liang, Z. Guo, K. Yang, G. Wang, H. Wang, X. Wan, Z. Li, Y. Bai, Y. Zhang, J. Liu, Y. Feng, Z. Zheng, C. Lu, G. He, Z. Xiong, Z. Liu, S. Chen, Y. Guo, M. Zeng, J. Lin and L. Fu, *Nature*, 2023, 619, 73–77.
- 150 Z. Li, K. G. Pradeep, Y. Deng, D. Raabe and C. C. Tasan, *Nature*, 2016, **534**, 227–230.
- 151 S. Wei, S. J. Kim, J. Kang, Y. Zhang, Y. Zhang, T. Furuhara, E. S. Park and C. C. Tasan, *Nat. Mater.*, 2020, 19, 1175–1181.
- 152 J. Kwon, S. Sun, S. Choi, K. Lee, S. Jo, K. Park, Y. K. Kim, H. B. Park, H. Y. Park, J. H. Jang, H. Han, U. Paik and T. Song, Adv. Mater., 2023, 35, e2300091.
- 153 Y. Dou, Y. Xie, X. Hao, T. Xia, Q. Li, J. Wang, L. Huo and H. Zhao, *Appl. Catal.*, *B*, 2021, **297**, 120403.

154 Q. Gong, Y. Wang, Q. Hu, J. Zhou, R. Feng, P. N. Duchesne, P. Zhang, F. Chen, N. Han, Y. Li, C. Jin, Y. Li and S. T. Lee, Nat. Commun., 2016, 7, 13216.

Review Article

- 155 Z. Zheng, L. Yu, M. Gao, X. Chen, W. Zhou, C. Ma, L. Wu, J. Zhu, X. Meng, J. Hu, Y. Tu, S. Wu, J. Mao, Z. Tian and D. Deng, Nat. Commun., 2020, 11, 3315.
- 156 Y. Zhang, Y. Zhang, B. Tian, H. Li, Z. Zeng and D. Ho, Mater. Today Energy, 2022, 29, 101133.
- 157 S. Geng, F. Tian, M. Li, X. Guo, Y. Yu, W. Yang and Y. Hou, J. Mater. Chem. A, 2021, 9, 8561-8567.
- 158 Q. Li, X. Zou, X. Ai, H. Chen, L. Sun and X. Zou, Adv. Energy Mater., 2019, 9, 1803369.
- 159 Y. Wang, X. Li, M. Zhang, Y. Zhou, D. Rao, C. Zhong, J. Zhang, X. Han, W. Hu, Y. Zhang, K. Zaghib, Y. Wang and Y. Deng, Adv. Mater., 2020, 32, e2000231.
- 160 S. Shen, Z. Wang, Z. Lin, K. Song, Q. Zhang, F. Meng, L. Gu and W. Zhong, Adv. Mater., 2022, 34, e2110631.
- 161 Z. Yang, J. Zhu, X. Xu, L. Wang, G. Zhou, Z. Yang and Y. Zhang, RSC Adv., 2023, 13, 4056-4064.
- 162 I. S. Kwon, I. H. Kwak, G. M. Zewdie, S. J. Lee, J. Y. Kim, S. J. Yoo, J. G. Kim, J. Park and H. S. Kang, Adv. Mater., 2022, 34, e2205524.
- 163 C. Lu, I. C. Lee, R. I. Masel, A. Wieckowski and C. Rice, J. Phys. Chem. A, 2002, 106, 3084-3091.
- 164 V. Stamenkovic, B. S. Mun, K. J. J. Mayrhofer, P. N. Ross, N. M. Markovic, J. Rossmeisl, J. Greeley and J. K. Nørskov, Angew. Chem., Int. Ed., 2006, 45, 2897-2901.
- 165 E. Toyoda, R. Jinnouchi, T. Hatanaka, Y. Morimoto, K. Mitsuhara, A. Visikovskiy and Y. Kido, J. Phys. Chem. C, 2011, 115, 21236-21240.
- 166 F. Ando, T. Tanabe, T. Gunji, S. Kaneko, T. Takeda, T. Ohsaka and F. Matsumoto, ACS Appl. Nano Mater., 2018, 1, 2844-2850.
- 167 F. Ando, T. Gunji, T. Tanabe, I. Fukano, H. D. Abruña, J. Wu, T. Ohsaka and F. Matsumoto, ACS Catal., 2021, 11, 9317-9332.
- 168 Y. P. Zhang, Z. X. Su, H. H. Wei, Z. Q. Wang and X. Q. Gong, J. Phys. Chem. Lett., 2023, 14, 1990-1998.
- 169 X. Zhu, X. Tan, K. H. Wu, S. C. Haw, C. W. Pao, B. J. Su, J. Jiang, S. C. Smith, J. M. Chen, R. Amal and X. Lu, Angew. Chem., Int. Ed., 2021, 60, 21911-21917.
- 170 A. Grimaud, W. T. Hong, Y. Shao-Horn and J. M. Tarascon, Nat. Mater., 2016, 15, 121-126.
- 171 S. Wang, Z. Ren, S. Yu, B. Huang, Y. Dai and W. Wei, J. Mater. Chem. A, 2023, 11, 14952-14958.
- 172 X. Wang, H. Zhong, S. Xi, W. S. V. Lee and J. Xue, Adv. Mater., 2022, 34, e2107956.
- 173 B. Weng, Z. Song, R. Zhu, Q. Yan, Q. Sun, C. G. Grice, Y. Yan and W. J. Yin, Nat. Commun., 2020, 11, 3513.
- 174 J. Li, Nano-Micro Lett., 2022, 14, 112.
- 175 N. Zhang and Y. Chai, Energy Environ. Sci., 2021, 14, 4647-4671.
- 176 H. Lee, O. Gwon, K. Choi, L. Zhang, J. Zhou, J. Park, J.-W. Yoo, J.-Q. Wang, J. H. Lee and G. Kim, ACS Catal., 2020, 10, 4664-4670.
- 177 Y. Huang, M. Li, F. Pan, Z. Zhu, H. Sun, Y. Tang and G. Fu, Carbon Energy, 2022, 5, e279.

- 178 Y. Sun, Z. Zhao, S. Wu, W. Li, B. Wu, G. Liu, G. Chen, B. Xu, B. Kang, Y. Li and C. Li, ChemSusChem, 2020, 13, 2671-2676.
- 179 Y. Pan, X. Xu, Y. Zhong, L. Ge, Y. Chen, J. M. Veder, D. Guan, R. O'Hayre, M. Li, G. Wang, H. Wang, W. Zhou and Z. Shao, Nat. Commun., 2020, 11, 2002.
- 180 Y. Sun, H. Liao, J. Wang, B. Chen, S. Sun, S. J. H. Ong, S. Xi, C. Diao, Y. Du, J.-O. Wang, M. B. H. Breese, S. Li, H. Zhang and Z. J. Xu, Nat. Catal., 2020, 3, 554-563.
- 181 F. Cheng, J. Shen, B. Peng, Y. Pan, Z. Tao and J. Chen, Nat. Chem., 2011, 3, 79-84.
- 182 J. Baek, M. D. Hossain, P. Mukherjee, J. Lee, K. T. Winther, J. Leem, Y. Jiang, W. C. Chueh, M. Bajdich and X. Zheng, Nat. Commun., 2023, 14, 5936.
- 183 J. Yang, T. Fujigaya and N. Nakashima, Sci. Rep., 2017, 7, 45384.
- 184 D. Luo, B. Yang, Z. Mei, Q. Kang, G. Chen, X. Liu and N. Zhang, ACS Appl. Mater. Interfaces, 2022, 14, 52857-52867.
- 185 X. Cheng, E. Fabbri, M. Nachtegaal, I. E. Castelli, M. El Kazzi, R. Haumont, N. Marzari and T. J. Schmidt, Chem. Mater., 2015, 27, 7662-7672.
- 186 A. Grimaud, O. Diaz-Morales, B. Han, W. T. Hong, Y. L. Lee, L. Giordano, K. A. Stoerzinger, M. T. M. Koper and Y. Shao-Horn, Nat. Chem., 2017, 9, 457-465.
- 187 J. T. Mefford, X. Rong, A. M. Abakumov, W. G. Hardin, S. Dai, A. M. Kolpak, K. P. Johnston and K. J. Stevenson, Nat. Commun., 2016, 7, 11053.
- 188 Y. Duan, S. Sun, Y. Sun, S. Xi, X. Chi, Q. Zhang, X. Ren, J. Wang, S. J. H. Ong, Y. Du, L. Gu, A. Grimaud and Z. J. Xu, Adv. Mater., 2019, 31, e1807898.
- 189 L. Zhang, H. Jang, H. Liu, M. G. Kim, D. Yang, S. Liu, X. Liu and J. Cho, Angew. Chem., Int. Ed., 2021, 60, 18821-18829.
- 190 C. Yang, H. Xie, B. Li, C. Shi, C. He, N. Zhao and E. Liu, J. Alloys Compd., 2023, 941, 168918.
- 191 L. Y. Zhang, C. X. Guo, H. Cao, S. Wang, Y. Ouyang, B. Xu, P. Guo and C. M. Li, Chem. Eng. J., 2022, 431, 133237.
- 192 X. Cui, Y. Tao, X. Xu and G. Yang, J. Power Sources, 2023, 557, 232519.
- 193 X. Wang, Y. An, L. Liu, L. Fang, Y. Liu, J. Zhang, H. Qi, T. Heine, T. Li, A. Kuc, M. Yu and X. Feng, Angew. Chem., Int. Ed., 2022, 61, e202209746.
- 194 L. Li, G. Zhang, J. Xu, H. He, B. Wang, Z. Yang and S. Yang, Adv. Funct. Mater., 2023, 33, 2213304.
- 195 C. Berger, Z. Song, T. Li, X. Li, A. Y. Ogbazghi, R. Feng, Z. Dai, A. N. Marchenkov, E. H. Conrad, P. N. First and W. A. de Heer, J. Phys. Chem. B, 2004, 108, 19912–19916.
- 196 Y. J. Sa, S. O. Park, G. Y. Jung, T. J. Shin, H. Y. Jeong, S. K. Kwak and S. H. Joo, ACS Catal., 2018, 9, 83-97.
- 197 Z. Shi, W. Yang, Y. Gu, T. Liao and Z. Sun, Adv. Sci., 2020, 7, 2001069.
- 198 T. Möller, W. Ju, A. Bagger, X. Wang, F. Luo, T. Ngo Thanh, A. S. Varela, J. Rossmeisl and P. Strasser, Energy Environ. Sci., 2019, 12, 640-647.
- 199 C. Lin, X. Liu, J. Qu, X. Feng, Z. W. Seh, T. Wang and Q. Zhang, Mater. Adv., 2021, 2, 5704–5711.
- 200 T. Deng, C. Cen, H. Shen, S. Wang, J. Guo, S. Cai and M. Deng, J. Phys. Chem. Lett., 2020, 11, 6320-6329.

201 A. E. Genc and I. C. Tranca, Phys. Chem. Chem. Phys., 2023, 25, 18465–18480.

Chem Soc Rev

- 202 R. Wang, C. He, W. Chen, L. Fu, C. Zhao, J. Huo and C. Sun, *Nanoscale*, 2021, 13, 19247–19254.
- 203 B. Yu, H. Li, J. White, S. Donne, J. Yi, S. Xi, Y. Fu, G. Henkelman, H. Yu, Z. Chen and T. Ma, *Adv. Funct. Mater.*, 2020, 30, 1905665.
- 204 X. Li, Q. Zhou, S. Wang, Y. Li, Y. Liu, Q. Gao and Q. Wu, *J. Phys. Chem. C*, 2021, **125**, 11963–11974.
- 205 Q. Zhang, X. Wang, F. Zhang, C. Fang, D. Liu and Q. Zhou, *ACS Appl. Mater. Interfaces*, 2023, **15**, 11812–11826.
- 206 M. Mukherjee, S. Dutta, M. Ghosh, P. Basuchowdhuri and A. Datta, *Phys. Chem. Chem. Phys.*, 2022, 24, 17050–17058.
- 207 X. Wang and L.-M. Yang, Appl. Surf. Sci., 2022, 576, 151839.
- 208 C. Quan, S. Xiao, Y. Yi, D. Sun, S. Ji, S. Zhou, J. Yang, X. Niu and X. A. Li, *Int. J. Hydrogen Energy*, 2022, **47**, 22035–22044.
- 209 J. Yu, X. Yong and S. Lu, Energy Environ. Mater., 2023, e12587.
- 210 F. Lai, N. Chen, X. Ye, G. He, W. Zong, K. B. Holt, B. Pan, I. P. Parkin, T. Liu and R. Chen, *Adv. Funct. Mater.*, 2020, 30, 1907376.
- 211 Y. Luo, Q. Li, Y. Tian, Y. Liu and K. Chu, *J. Mater. Chem. A*, 2022, **10**, 1742–1749.
- 212 P.-Y. Liu, K. Shi, W.-Z. Chen, R. Gao, Z.-L. Liu, H. Hao and Y.-Q. Wang, *Appl. Catal.*, *B*, 2021, **287**, 119956.
- 213 H. Guo, H. Zhang, J. Zhao, P. Yuan, Y. Li, Y. Zhang, L. Li, S. Wang and R. Song, *J. Phys. Chem. C*, 2022, **126**, 3043–3053.
- 214 A. Biswas, S. Kapse, B. Ghosh, R. Thapa and R. S. Dey, *Proc. Natl. Acad. Sci. U. S. A.*, 2022, **119**, e2204638119.
- 215 X. Lu, D. Y. C. Leung, H. Wang, M. K. H. Leung and J. Xuan, *ChemElectroChem*, 2014, **1**, 836–849.
- 216 S.-G. Wang, X.-Y. Liao, D.-B. Cao, C.-F. Huo, Y.-W. Li, J. Wang and H. Jiao, *J. Phys. Chem. C*, 2007, **111**, 16934–16940.
- 217 S. Rasul, D. H. Anjum, A. Jedidi, Y. Minenkov, L. Cavallo and K. Takanabe, *Angew. Chem., Int. Ed.*, 2015, 54, 2146–2150.
- 218 E. L. Clark, C. Hahn, T. F. Jaramillo and A. T. Bell, *J. Am. Chem. Soc.*, 2017, **139**, 15848–15857.
- 219 W. Ren, X. Tan, J. Qu, S. Li, J. Li, X. Liu, S. P. Ringer, J. M. Cairney, K. Wang, S. C. Smith and C. Zhao, *Nat. Commun.*, 2021, 12, 1449.
- 220 W. Zhang, L. Wang, H. Liu, Y. Hao, H. Li, M. U. Khan and J. Zeng, *Nano Lett.*, 2017, **17**, 788–793.
- 221 M. Feng, X. Wu, H. Cheng, Z. Fan, X. Li, F. Cui, S. Fan, Y. Dai, G. Lei and G. He, *J. Mater. Chem. A*, 2021, 9, 23817–23827.
- 222 H. Huang, H. Jia, Z. Liu, P. Gao, J. Zhao, Z. Luo, J. Yang and J. Zeng, *Angew. Chem., Int. Ed.*, 2017, **56**, 3594–3598.
- 223 C. Zhang, W. Zhang, F. Karadas, J. Low, R. Long, C. Liang, J. Wang, Z. Li and Y. Xiong, *Nanoscale*, 2022, 14, 7702–7710.
- 224 S. Liu, H. Tao, Q. Liu, Z. Xu, Q. Liu and J.-L. Luo, *ACS Catal.*, 2018, **8**, 1469–1475.
- 225 S. Sun, X. Zhou, B. Cong, W. Hong and G. Chen, *ACS Catal.*, 2020, **10**, 9086–9097.
- 226 H. Tandon, M. Labarca and T. Chakraborty, *ChemistrySelect*, 2021, **6**, 5622–5627.

- 227 M. Filatov, S. Lee, H. Nakata and C. H. Choi, *J. Phys. Chem. A*, 2020, **124**, 7795–7804.
- 228 F. Calle-Vallejo, Adv. Sci., 2023, 10, e2207644.
- 229 Y. Zhu, D. Zhang, L. Gong, L. Zhang and Z. Xia, Front. Mater., 2019, 6, 16.
- 230 Z. Zhao, M. Li, L. Zhang, L. Dai and Z. Xia, Adv. Mater., 2015, 27, 6834–6840.
- 231 H. Xu, D. Cheng, D. Cao and X. C. Zeng, *Nat. Catal.*, 2024, 7, 207–218.
- 232 N. Ran, W. Qiu, E. Song, Y. Wang, X. Zhao, Z. Liu and J. Liu, *Chem. Mater.*, 2020, 32, 1224–1234.
- 233 H. Guo, L. Li, X. Wang, G. Yao, H. Yu, Z. Tian, B. Li and L. Chen, *ACS Appl. Mater. Interfaces*, 2019, **11**, 36506–36514.
- 234 M. Yao, Z. Shi, P. Zhang, W.-J. Ong, J. Jiang, W.-Y. Ching and N. Li, *ACS Appl. Nano Mater.*, 2020, 3, 9870–9879.
- 235 H.-J. Yin, J.-H. Zhou and Y.-W. Zhang, *Inorg. Chem. Front.*, 2019, 6, 2582–2618.
- 236 Z. W. Seh, J. Kibsgaard, C. F. Dickens, I. Chorkendorff, J. K. Nørskov and T. F. Jaramillo, *Science*, 2017, 355, 146.
- 237 G. Zheng, Y. Li, X. Qian, G. Yao, Z. Tian, X. Zhang and L. Chen, *ACS Appl. Mater. Interfaces*, 2021, **13**, 16336–16344.
- 238 X. Wang, Q. Zhang and J. Zhou, *J. Colloid Interface Sci.*, 2022, **610**, 546–556.
- 239 S. Wang, H. Gao, L. Li, K. S. Hui, D. A. Dinh, S. Wu, S. Kumar, F. Chen, Z. Shao and K. N. Hui, *Nano Energy*, 2022, **100**, 108545.
- 240 S. Wang, L. Li, K. S. Hui, D. A. Dinh, Z. Lu, Q. Zhang and K. N. Hui, *Nano Energy*, 2023, **113**, 108543.
- 241 Z. N. Zhang, Q. L. Hong, X. H. Wang, H. Huang, S. N. Li and Y. Chen, *Small*, 2023, **19**, e2300530.
- 242 Y. Wang, D. Wu, P. Lv, B. He, X. Li, D. Ma and Y. Jia, *Nanoscale*, 2022, **14**, 10862–10872.
- 243 L. Gong, D. Zhang, C. Y. Lin, Y. Zhu, Y. Shen, J. Zhang, X. Han, L. Zhang and Z. Xia, *Adv. Energy Mater.*, 2019, 9, 1902625.
- 244 J. Wang, M. Zheng, X. Zhao and W. Fan, ACS Catal., 2022, 12, 5441–5454.
- 245 L. Gong, X. Wang, T. Zheng, J. Liu, J. Wang, Y.-C. Yang, J. Zhang, X. Han, L. Zhang and Z. Xia, *J. Mater. Chem. A*, 2021, 9, 3555–3566.
- 246 C. Zhu, Z. Zhang, L. Zhong, C.-S. Hsu, X. Xu, Y. Li, S. Zhao, S. Chen, J. Yu, S. Chen, M. Wu, P. Gao, S. Li, H. M. Chen, K. Liu and L. Zhang, *Chem*, 2021, 7, 406–420.
- 247 M. D. Pohl, S. Watzele, F. Calle-Vallejo and A. S. Bandarenka, *ACS Omega*, 2017, **2**, 8141–8147.
- 248 W. Gao, Y. Chen, B. Li, S. P. Liu, X. Liu and Q. Jiang, *Nat. Commun.*, 2020, **11**, 1196.
- 249 X. Chang, Z. J. Zhao, Z. Lu, S. Chen, R. Luo, S. Zha, L. Li, G. Sun, C. Pei and J. Gong, *Nat. Nanotechnol.*, 2023, 18, 611-616.
- 250 Q. Dang, S. Tang, T. Liu, X. Li, X. Wang, W. Zhong, Y. Luo and J. Jiang, *J. Phys. Chem. Lett.*, 2021, **12**, 8355–8362.
- 251 Z. Li, R. Ma, Q. Ju, Q. Liu, L. Liu, Y. Zhu, M. Yang and J. Wang, *Innovation*, 2022, 3, 100268.
- 252 A. Cao and J. K. Nørskov, ACS Catal., 2023, 13, 3456-3462.
- 253 L. Ju, X. Tan, X. Mao, Y. Gu, S. Smith, A. Du, Z. Chen,C. Chen and L. Kou, *Nat. Commun.*, 2021, 12, 5128.

254 Z. Chen, H. Niu, J. Ding, H. Liu, P. H. Chen, Y. H. Lu, Y. R. Lu, W. Zuo, L. Han, Y. Guo, S. F. Hung and Y. Zhai, Angew. Chem., Int. Ed., 2021, 60, 25404-25410.

Review Article

- 255 Y. Yang, L. Zhang, Z. Hu, Y. Zheng, C. Tang, P. Chen, R. Wang, K. Qiu, J. Mao, T. Ling and S. Z. Qiao, Angew. Chem., Int. Ed., 2020, 59, 4525-4531.
- 256 T. Wu, X. Ren, Y. Sun, S. Sun, G. Xian, G. G. Scherer, A. C. Fisher, D. Mandler, J. W. Ager, A. Grimaud, J. Wang, C. Shen, H. Yang, J. Gracia, H.-J. Gao and Z. J. Xu, Nat. Commun., 2021, 12, 3634.
- 257 X. Ren, T. Wu, Y. Sun, Y. Li, G. Xian, X. Liu, C. Shen, J. Gracia, H. J. Gao, H. Yang and Z. J. Xu, Nat. Commun., 2021, 12, 2608.
- 258 L. Zhang, T. Gu, K. Lu, L. Zhou, D. S. Li and R. Wang, Adv. Funct. Mater., 2021, 31, 2103187.
- 259 G. Yang, J. Zhu, P. Yuan, Y. Hu, G. Qu, B. A. Lu, X. Xue, H. Yin, W. Cheng, J. Cheng, W. Xu, J. Li, J. Hu, S. Mu and J. N. Zhang, Nat. Commun., 2021, 12, 1734.
- 260 F. Li, H. Ai, D. Liu, K. H. Lo and H. Pan, J. Mater. Chem. A, 2021, 9, 17749-17759.
- 261 Y. Zhang, Q. Zhang, D.-X. Liu, Z. Wen, J.-X. Yao, M.-M. Shi, Y.-F. Zhu, J.-M. Yan and Q. Jiang, Appl. Catal., B, 2021, 298, 120592.
- 262 Y. Wang, W. Cheng, P. Yuan, G. Yang, S. Mu, J. Liang, H. Xia, K. Guo, M. Liu, S. Zhao, G. Qu, B. A. Lu, Y. Hu, J. Hu and J. N. Zhang, Adv. Sci., 2021, 8, e2102915.
- 263 Y. Wen, J. Liu, F. Zhang, Z. Li, P. Wang, Z. Fang, M. He, J. Chen, W. Song, R. Si and L. Wang, Nano Res., 2022, 16, 4664-4670.
- 264 Y. Zhang, J.-Z. Wang, K. Li, M.-M. Shi, Z. Wen, M.-G. Jiao and D. Bao, J. Mater. Chem. A, 2022, 10, 2819-2825.

- 265 A. Cao, V. J. Bukas, V. Shadravan, Z. Wang, H. Li, J. Kibsgaard, I. Chorkendorff and J. K. Norskov, Nat. Commun., 2022, 13, 2382.
- 266 X. Guo and S. Huang, Electrochim. Acta, 2018, 284, 392-399.
- 267 J. Huang, J. Yu, X. Lu, Y. Wei, H. Song, A. Cao, J. Cai, S.-Q. Zang and S. Lu, Inorg. Chem. Front., 2023, 10, 3955-3962.
- 268 K. Takahashi, J. Ohyama, S. Nishimura, J. Fujima, L. Takahashi, T. Uno and T. Taniike, Chem. Commun., 2023, 59, 2222-2238.
- 269 B. M. Abraham, P. Sinha, P. Halder and J. K. Singh, J. Mater. Chem. A, 2023, 11, 8091-8100.
- 270 C. Y. Lim, I. R. Made, Z. H. Khoo, C. K. Ng, Y. Bai, J. Wang, G. Yang, A. D. Handoko and Y. F. Lim, Mater. Horiz., 2023, 10, 5022-5031.
- 271 H. Mai, T. C. Le, D. Chen, D. A. Winkler and R. A. Caruso, Chem. Rev., 2022, 122, 13478-13515.
- 272 L. Zhang, X. Guo, S. Zhang, T. Frauenheim and S. Huang, Adv. Energy Mater., 2023, 14, 2302754.
- 273 M. Ren, X. Guo, S. Zhang and S. Huang, Adv. Funct. Mater., 2023, 33, 2213543.
- 274 X. Wan, Z. Zhang, H. Niu, Y. Yin, C. Kuai, J. Wang, C. Shao and Y. Guo, J. Phys. Chem. Lett., 2021, 12, 6111-6118.
- 275 V. Fung, G. Hu, Z. Wu and D.-E. Jiang, J. Phys. Chem. C, 2020, 124, 19571-19578.
- 276 L. Zhang, X. Guo, S. Zhang and S. Huang, Appl. Mater. Today, 2021, 25, 101177.
- 277 D. Jiao, D. Zhang, D. Wang, J. Fan, X. Ma, J. Zhao, W. Zheng and X. Cui, Nano Res., 2023, 16, 11511-11520.
- 278 Z. Song, Q. Zhou, S. Lu, S. Dieb, C. Ling and J. Wang, J. Phys. Chem. Lett., 2023, 14, 3594-3601.